amU
Aix Marseille Université

NNT : 2024AIXM0001

THÈSE DE DOCTORAT

Soutenue à AMU — Aix-Marseille Université
le 7 novembre 2024 par

Kirill Afonin

Étude du transport de la poudre de bore injectée dans le plasma du tokamak WEST et de son effet sur la performance de la décharge

Discipline
Physique et Sciences de la Matière

Spécialité
Energie, Rayonnement et Plasma

École doctorale
ED 352 Physique et sciences de la matière

Laboratoire/Partenaires de recherche
Commissariat à l'énergie atomique et aux énergies alternatives,
Princeton Plasma Physics Laboratory

Composition du jury

Karl KRIEGER MPG/IPP Garching, Chercheur	Rapporteur
Tom WAUTERS ITER organization, Chercheur	Rapporteur
Davide CURRELI University of Illinois, Professeur Ordinaire	Examinateur
Cécile ARNAS PIIM, CNRS/AMU, Directeur de Recherche	Examinatrice
Frédéric BROCHARD Institut Jean Lamour, Professeur Ordinaire	Président du jury
Yannick MARANDET PIIM, CNRS/AMU, Directeur de Recherche	Directeur de thèse
Alberto GALLO CEA Cadarache, Chercheur	Co-encadrant
Philippe MOREAU CEA Cadarache, Directeur de Recherche	Membre invité

cea irfm PPPL EUROfusion

Affidavit

I, undersigned, Kirill Afonin, hereby declare that the work presented in this manuscript is my own work, carried out under the scientific supervision of Alberto Gallo, in accordance with the principles of honesty, integrity and responsibility inherent to the research mission. The research work and the writing of this manuscript have been carried out in compliance with both the french national charter for Research Integrity and AMU charter on the fight against plagiarism.

This work has not been submitted previously either in this country or in another country in the same or in a similar version to any other examination body.

Saint-Paul-lez-Durance, August 27th, 2024



This work is licensed under Creative Commons Attribution-NonCommercial-NoDerivatives 4.0 International Public License

List of publications and conference contributions

List of publications authored during the doctoral studies:

1. K. Afonin, A. Gallo, Y. Marandet, Ph. Moreau, G. Bodner, H. Bufferand,G. Ciraolo, C. Desgranges, P. Devynck, A. Diallo, J. Gaspar, C. Guillemaut, R. Guirlet, J.-P. Gunn, N. Fedorczak, T. Loarer, R. Lunsford, P. Manas, F. Nespoli, N. Rivals, P. Tamain, E.A. Unterberg and the WEST Team. Interpretive modelling of boron transport in the boundary plasma of WEST experiments with the impurity powder dropper. *2023* Nuclear Fusion **63 126057**. DOI: 10.1088/1741-4326/ad0597

2. K. Afonin, A. Gallo, R. Lunsford, S. Bose, Y. Marandet, P. Moreau, G. Bodner, H. Bufferand, G. Ciraolo, C. Desgranges, P. Devynck, A. Diallo, J. Gaspar, C. Guillemaut, R. Guirlet, J.P. Gunn, N. Fedorczak, Y. Corre, F. Nespoli, N. Rivals, T. Loarer, P. Tamain, E.A. Unterberg and the WEST team. Boron powder injection experiments in WEST with a fully actively cooled, ITER grade, tungsten divertor. *2024* Nuclear Materials and Energy, accepted manuscript

Participation in conferences and summer schools during the doctoral studies:

1. K. Afonin *et al.* Interpretative modelling of boron transport in the WEST boundary plasma in experiments with impurity powder dropper. October 17–21, 2022; Spokane, Washington, USA

2. 60th Culham Plasma Physics Summer School, July 17-27 2023

3. K. Afonin *et al.* Boron powder injection in WEST during long pulses with a fully actively cooled, ITER grade tungsten divertor. October 30–November 3 2023; Denver, Colorado, USA

4. K. Afonin *et al.* Real-time boron powder injection experiments in WEST with ITER grade full-tungsten divertor. May 12–17 2024; Marseille, France

5. K. Afonin *et al.* Analysis of boron powder injection experiments on WEST with interpretive modelling suite. October 7–11 2024; Atlanta, Georgia, USA

Abstract and keywords in English

With ITER transitioning to tungsten (W) plasma-facing components (PFCs), study of wall conditioning techniques becomes an important subject for achieving high-yield fusion plasmas. Wall conditioning in tokamaks is necessary to remove unwanted impurities from the vessel, which otherwise would lead to increased radiative losses and fuel dilution, lowering the fusion energy yield. A novel conditioning technique that is currently being studied is boronization via boron (B) powder injection with an Impurity Powder Dropper (IPD). Boronization with an IPD device is performed by dropping B powder during a plasma pulse, where B powder is evaporated, B atoms are ionized and subsequently deposited on the PFCs. This method acts as an alternative to an established conditioning technique called Glow Discharge Boronization (GDB), where B is injected in form of diborane gas (B_2D_6) into a glow discharge between positively-charged electrodes and negatively-charged tokamak walls. B from B_2D_6 is ionized and deposited onto the walls, where it traps the light impurities, e.g. oxygen (O) which is introduced into the vessel during the vent of the machine or through unavoidable micro-leaks. Benefits of GDB are well-known, and boronization via IPD injections is being studied as an alternative with a similar effect but with a number of upsides: the injection can be performed on-demand without interrupting tokamak operation and does not require the usage of toxic B_2D_6. However, it requires plasma to operate. This thesis attempts to extend the existing research of B study in pulses with IPD injections in two directions: the experimental part, where experiments with an IPD device installed on W Environment Steady-State Tokamak (WEST) are performed in an attempt to maximize the amount of B injected and the effects during and after the injections are studied, and the computational part, where WEST pulses with IPD are simulated using computational models to interpret the experimental results and gain insight into the injected B transport.

Keywords: fusion plasma, tokamak, WEST, wall conditioning, boron, IPD

Résumé et mots clés en français

Avec le passage d'ITER à des composants en tungstène (W) face au plasma (CFP), l'étude des techniques de conditionnement des parois devient un sujet important pour obtenir des plasmas de fusion à haut rendement. Le conditionnement des parois dans les tokamaks est nécessaire pour éliminer les impuretés indésirables de la chambre, qui sinon entraîneraient une augmentation des pertes radiatives et une dilution du combustible, ce qui réduirait le rendement énergétique de la fusion. Une nouvelle technique de conditionnement actuellement à l'étude est la boronisation par injection de poudre de bore (B) à l'aide d'un dispositif d'injection de poudre d'impureté (*Impurity Powder Dropper*, IPD). La boronisation à l'aide d'un dispositif IPD est réalisée en faisant tomber de la poudre de B pendant une décharge de plasma, dans laquelle la poudre de B est évaporée et les atomes de B sont ionisés avant de se déposer sur les CFP. Cette méthode est une alternative à une technique de conditionnement établie appelée boronisation par décharge luminescente (*Glow Discharge Boronization*, GDB), où le B est injecté sous forme de gaz diborane (B_2D_6) dans une décharge luminescente entre des électrodes chargées positivement et les parois du tokamak chargées négativement. Le B de B_2D_6 est ionisé et déposé sur les murs, où il piège les impuretés légères, par exemple l'oxygène (O) qui est introduit lorsque la machine est mise à l'air ou par des micro-fuites inévitables. Les avantages de la GDB sont bien connus, et la boronisation via des injections IPD est étudiée comme une alternative avec un effet similaire mais avec un certain nombre d'avantages : l'injection peut être effectuée à la demande sans interrompre le fonctionnement du tokamak et ne nécessite pas l'utilisation de B_2D_6 toxique. Elle nécessite cependant de pouvoir démarrer des plasmas. Cette thèse tente d'étendre la recherche existante sur l'étude du B dans les impulsions avec des injections IPD dans deux directions : la partie expérimentale, où des expériences avec un appareil IPD installé sur le tokamak en environnement de tungstène à l'état stable (*W Environment Steady-State Tokamak*, WEST) sont réalisées pour tenter de maximiser la quantité de B injecté et les effets pendant et après les injections sont étudiés, et la partie numérique, où les décharges WEST avec IPD sont simulées à l'aide de modèles numériques pour interpréter les résultats expérimentaux et obtenir un aperçu du transport du B injecté.

Mots clés : plasma de fusion, tokamak, WEST, conditionnement des murs, bore, IPD

Résumé étendu en français

1. Introduction

L'une des caractéristiques des plasmas de tokamaks, cruciale pour leur étude, est la présence d'*impuretés*, c'est-à-dire d'espèces autres que les espèces qui doivent fusionner, qui sont soit introduites de façon incontrôlée dans le plasma à partir des murs de la chambre par les fuites d'air ou de liquide de refroidissement, les interactions plasma-surface et/ou la formation d'oxydes pendant que la machine est exposée à l'air, soit injectés intentionnellement, par exemple pour la protection des CFP (composants face au plasma) via le refroidissement radiatif. Dans la région confinée, les impuretés réduisent la capacité du plasma à fusionner de plusieurs manières. Tout d'abord, les ions d'impureté introduisent une perte de puissance par le biais du rayonnement de raies lorsqu'ils ne sont pas complètement ionisés.

Ce problème est exacerbé par la charge atomique de l'impureté : avec l'augmentation de la charge atomique, le nombre d'états d'ionisation augmente également, ce qui entraîne une plus grande perte de rayonnement. Deuxièmement, la présence d'ions d'impureté dilue le plasma de deutérium et de tritium. Les ions d'impuretés sont accompagnés d'un grand nombre d'électrons et, pour une pression de plasma donnée, la concentration partielle des ions du combustible est réduite, ainsi que la puissance fusion. Ces deux problèmes sont préjudiciables à la maximisation du rendement énergétique de la fusion. Les impuretés peuvent également entraîner des *disruptions* du plasma : un refroidissement important du plasma peut affecter le profil du courant et donc modifier le champ poloïdal, entraînant la perte rapide du confinement de particules et de chaleur. Ces perturbations peuvent endommager le matériau de la première paroi, ce qui peut à son tour créer davantage de sources d'impuretés à la paroi.

Le tokamak ITER est développé pour étudier les plasmas pertinents pour une centrale de fusion, dans le but d'atteindre un *gain net d'énergie de fusion* $Q = 10$, où Q est le rapport entre la puissance de fusion produite et la puissance de chauffage [6]. L'une des conceptions initiales d'ITER prévoyait une première paroi entièrement en béryllium (Be) avec des CFP de divertor constitués d'un composite de fibres de carbone (C) et d'éléments en tungstène (W) [7]. La nécessité d'utiliser un matériau différent pour le divertor s'explique par la capacité de résister à des flux thermique plus faible des composants de la première paroi en Be, jusqu'à ~5 MW m^{-2} pour les panneaux « à flux thermique renforcé » et ~2 MW m^{-2} pour les panneaux « à flux thermique normal », alors que le divertor d'ITER a été développé pour supporter jusqu'à ~10 MW m^{-2} [8].

Si le Be présente les avantages décrits ci-dessus, il présente également des inconvénients sous la forme de la formation de poussières et d'une faible résistance aux charges thermiques dues à des perturbations non atténuées ou partiellement atténuées [9]. La formation de poussière de Be augmente effectivement la surface d'interaction des isotopes H avec le matériau de la paroi, ce qui entraîne une rétention accrue de T et impacte l'inventaire de T autorisé pour l'exploitation d'ITER. Les charges thermiques transitoires peuvent entraîner une réduction drastique de la durée de vie des CFP. Enfin, le Be est un métal toxique dont la manipulation est coûteuse. Pour ces raisons, la conception d'ITER a été modifiée en faveur d'une première paroi entièrement en W [10].

Le remplacement du Be par du W dans la conception de la première paroi a des effets positifs potentiels sur la rétention de T, la production de poussière et la résistance aux charges thermiques, mais il accroît également le risque lié à une augmentation potentielle du rayonnement du plasma du cœur, qui pourrait rendre le confinement du plasma non durable, avec un impact direct sur l'objectif de $Q = 10$. C'est pourquoi il est important d'étudier les interactions plasma-paroi dans les tokamaks activements refroidis existants afin de tester et d'améliorer la conception d'ITER.

Le tokamak W Environment Steady-state Tokamak (WEST) est un tokamak équipé de CFP entièrement en W qui permet de tester la conception du divertor W d'ITER [11] [12]. Les caractéristiques importantes qui font de WEST une excellente machine de test pour le divertor d'ITER sont la présence d'un divertor bas de technologie identique à celle d'ITER, activement refroidi [13] [14] et permettant des décharges longues. Le divertor de WEST a été conçu pour tester des charges thermiques de divertor pertinentes pour ITER de $\sim$ 10-20 MW m^{-2}, ainsi qu'une fluence de particules de $\sim 10^{27}$ D m^{-2} et une durée de décharge plasma de $\sim$ 1 000 s. Au cours de la campagne expérimentale de 2024, WEST a atteint une durée de décharge record de plus de 6 minutes, avec une puissance de chauffage de $\sim$ 3 MW et une densité intégrée dans le plan équatorial $\langle n_e l \rangle_{\text{central}}$ de $\sim 3 \times 10^{19}$m^{-2}.

Bien que l'utilisation du W présente certains avantages importants pour l'amélioration de l'extraction de puissance – une rétention de T plus faible que celle du C qui se lie chimiquement aux isotopes H et du Be qui forme des poussières et des couches codéposées, une température de fusion plus élevée que celle du Be et une absence de toxicité, contrairement au Be – la contamination du plasma par le W est particulièrement problématique en raison du numéro atomique élevé du W $Z_W = 74$. En raison de son Z élevé, le W n'est encore que partiellement ionisé lorsqu'il pénètre dans le plasma confiné, ce qui provoque des pertes radiatives jusqu'au cœur du plasma, diminuant ainsi le confinement de l'énergie.

Pour atténuer la pulvérisation de W, dominée par les impuretés, on procède à un *conditionnement*, qui consiste à traiter la première paroi afin de réduire la quantité de résidus déposés et/ou de les piéger dans le matériau de la paroi, inhibant ainsi leur pulvérisation et la pulvérisation ultérieure de W. Une approche alternative aux techniques de conditionnement actuelles est en cours de développement sous la forme d'une injection de bore (B) en poudre avec un « *Impurity Powder Dropper* » (IPD dans la suite).

L'idée principale du conditionnement de paroi en temps réel est l'injection d'une impureté métallique sous la forme d'une poudre pendant une impulsion de plasma. Lorsque la poudre d'impureté interagit avec le plasma, elle fond, s'évapore et s'ionise, et les ions d'impureté injectés sont transportés vers les parois du tokamak.

Une fois que l'ion injecté atteint les CFP, on s'attend à ce qu'il se recombine et se dépose sur la première paroi de la même manière que le B dans la boronisation par décharge luminescente (*Glow Discharge Boronization*, GDB dans la suite). Cependant, lors d'une GDB, le B est ionisé par une décharge non magnétisée , alors que dans une boronisation en temps réel avec un IPD, le B est ionisé par le plasma du tokamak, ce qui affecterait la distribution du dépôt de B en raison de la géométrie du champ magnétique. Par exemple, on s'attend à ce que le divertor reçoive un afflux de B plus important que les autres PFC. La motivation de l'injection de poudre de B est similaire à celle qui sous-tend la GDB : l'élimination des impuretés légères (c'est-à-dire leur capture dans les couches de dépôt) et la réduction du recyclage du D et des impuretés légères.

La boronisation par injection de poudre de B présente des caractéristiques intéressantes par rapport à la GDB. Tout d'abord, elle peut être réalisée à la demande, sans avoir à éteindre le champ toroidal, ce qui est important pour le fonctionnement des tokamaks supraconducteurs, car la GDB ne peut pas être réalisée en présence du champ magnétique. Deuxièmement, elle fait appel au métal B, qui est pratiquement inerte par rapport au B_2D_6 toxique.

Cette thèse vise à développer la recherche sur le conditionnement des parois des tokamaks W via l'IPD dans deux directions. Premièrement, nous tenterons d'étendre le domaine opérationnel de l'IPD dans WEST en maximisant le taux d'injection de B et la masse cumulée dans WEST pour essayer d'approcher des quantités de B injectées similaires à la GDB afin de comparer l'efficacité de ces deux méthodes dans le conditionnement du PFC. Deuxièmement, nous analyserons le transport des poudres de B dans les plasmas WEST afin d'améliorer les modèles de calcul existants et de mieux comprendre la distribution du B sur les PFC et la manière dont elle dépend des paramètres du plasma.

2. Partie expérimentale de la thèse

Les objectifs des expériences dédiées à l'IPD étaient, premièrement, d'élargir l'espace de fonctionnement de l'IPD sur WEST par rapport aux expériences réalisées lors de la campagne de mise en service de l'IPD. Deuxièmement, un nouveau divertor W de type ITER entièrement activement refroidi a été installé en 2021, et l'étude du conditionnement d'un tel divertor était l'un des objectifs de l'expérience. Troisièmement, nous avons essayé d'atteindre un taux d'injection de B et une masse totale de B injectée élevés, dans le but d'accumuler une masse de B comparable à la quantité totale de B injectée dans une décharge de conditionnement GDB typique, qui est d'environ 10 g, afin de comparer l'effet du conditionnement IPD à l'effet de la GDB. Enfin, l'étude de l'effet de l'injection de B sur le transport des impuretés de W et de celles de faible

charge (C, O,...) dans le domaine de fonctionnement élargi de l'IPD était également un objectif de l'expérience.

Deux séries d'expériences avec injection par l'IPD ont été réalisées au cours de cette étude. Dans la première série, à taux d'injection plus élevé, environ 1 g de B a été injecté au cours de quatre décharges, le taux d'injection maximal étant d'environ 58 mg/s. Les injections ont été réalisées dans la configuration en appui sur le divertor bas seulement (LSN, pour Lower single nul), avec une puissance de chauffage LH de 4,4 MW et un courant plasma de 500 kA, les injections commençant 10 secondes après le début du plateau de courant. La masse cumulée et le taux d'injection B maximal étaient environ trois fois plus élevés que lors de l'expérience précédente sur WEST.

Dans la deuxième série de taux d'injection plus faibles, qui s'est déroulée environ un an après la série de taux d'injections plus élevés, trois décharges de référence et 14 décharges avec injection de poudre ont été réalisées. Les conditions du plasma étaient beaucoup moins favorables que pour la série de taux d'injection plus élevés, probablement en raison de l'accumulation d'impuretés au cours de la campagne expérimentale. Pour cette raison, des taux d'injection beaucoup plus faibles, de l'ordre de 3 à 5 mg/s, ont été maintenus. Pour compenser la fenêtre de fonctionnement plus réduite en ce qui concerne le taux d'injection, les injections ont été réalisées dans deux autres scénarios de décharge : dans des décharges ohmiques sans chauffage additionnel et dans le scénario de *décharge longue* (« long pulse »), c'est-à-dire avec 3 MW de chauffage LH, un courant plasma de 400 kA et une durée d'impulsion supérieure à 60 s. En outre, une injection de poudre de nitrure de bore (BN) a également été réalisée pour comparer son effet sur le plasma à l'effet du B, car le BN semble avoir un effet plus important sur le confinement de l'énergie du cœur [43].

Comme pour les expériences de mise en service en 2021, nous avons observé les effets en temps réel de l'injection de B sur le conditionnement des parois par spectroscopie visible au niveau de différents CFP (divertors bas et haut, limiteur côté fort champ et antenne hybride du côté faible champ). Les changements dans la luminosité de la raie B-II indiquent l'augmentation de la quantité de B dans le divertor inférieur. Les changements de luminosité de la ligne D-I et des lignes d'impuretés légères indiquent des taux de recyclage plus faibles de l'ion principal et des espèces d'impuretés légères. L'évolution de la luminosité de la raie W-I indique une pulvérisation accrue de W par le B injecté. La température des électrons de la cible n'a pratiquement pas été affectée par l'injection de poudre de B, à l'exception d'une chute soudaine vers la fin de l'injection à t=22,5 s dans la décharge 58051, ce qui suggère un détachement partiel de la jambe interne dans ce cas. Alors que la GDB est réalisée pour lier l'O via l'effet de dit de « gettering », les données spectroscopiques suggèrent que pendant l'injection de poudre B, les impuretés légères peuvent être piégées dans les couches B déposées, ce qui peut être important si l'on considère que le carbone (C) sur WEST peut encore contribuer de manière significative à la pulvérisation de W [18]. Comme pour les expériences de mise en service, une amélioration du confinement a également été observée, se traduisant par une augmentation de T_e au centre du plasma, de W_{MHD} ainsi que du flux de neutrons.

Outre les effets observés de l'injection de B qui étaient également présents dans la

série préliminaire (augmentation de W_{MHD}, effets sur l'émission de raies provenant d'impuretés de faible Z et de W, etc.), le retournement (« roll-over ») du comportement de la puissance rayonnée totale s'est produit au seuil d'injection de B d'environ 20 mg/s. Étant donné que les effets de conditionnement étaient présents pour les taux d'injection inférieurs à ce seuil, ce changement de comportement est probablement dû à l'effet de l'injection de B sur le transport du W du SOL vers le plasma du cœur.

Les effets de conditionnement de l'injection de poudre de B ont été comparés aux effets de la GDB. Des niveaux de conditionnement similaires ont été obtenus après le conditionnement GDB avec une masse cumulée de 10 g et après des injections IPD avec une masse cumulée d'environ 530 mg, avec un taux de réduction similaire des effets de conditionnement pendant les impulsions de 4 MW. Le conditionnement par injection d'IPD semble être une alternative viable à la GDB, qui peut être appliquée pendant une période plus courte (~ minutes de fonctionnement de l'IPD contre ~ heures de fonctionnement de la GDB) et à la demande.

3. Partie simulation numérique de la thèse

Dans la partie numérique de notre étude, nous avons abordé le problème de la modélisation de l'expérience IPD d'une manière similaire à la méthode de Shoji et al. [51], avec la suite de codes SOLEDGE3X-EIRENE [70] modélisant le plasma de bord, y compris le transport du bore, et le code DIS (Dust Injection Simulator) [71] modélisant la dynamique et l'évaporation des poudres.

Le modèle numérique de plasma de bord de SOLEDGE3X-EIRENE se compose de deux parties couplées : SOLEDGE3X [70], un code de transport multi-espèces qui peut simuler le plasma de D avec plusieurs impuretés, et EIRENE [72], qui sert à modéliser les neutres.

SOLEDGE3X modélise le plasma de bord comme un fluide magnétisé en faisant évoluer les équations fluides pour $n_{e,i}$, $v_{\parallel}^{e,i}$, et $T_{e,i}$ avec une fermeture collisionnelle dérivée de Zhdanov [73]. Les équations de transport dans SOLEDGE3X sont décrites dans [70], l'équation du bilan de masse étant d'un intérêt particulier pour notre étude :

$$\partial_t n_\alpha + \vec{\nabla} \cdot (n_\alpha \vec{v_\alpha}) = S_\alpha^n$$

où n_α est la densité de l'ion α et S_α^n est la source d'ions due à l'ionisation ou à la recombinaison. La vitesse $\vec{v_\alpha}$ est décomposée en composantes parallèle et perpendiculaire $\vec{v_\alpha} = v_{\parallel,\alpha}\vec{b} + \vec{v_{\perp,\alpha}}$, où $\vec{b} = \vec{B}/B$ est la direction du champ magnétique. La vitesse perpendiculaire $\vec{v_{\perp,\alpha}}$ est calculée à partir des équations de transport du champ transverse qui peuvent impliquer des dérives transverses au champs B et une diffusivité anormale, due par exemple à la turbulence. Dans les simulations des plasmas de bord des expériences avec IPD, les dérives n'ont pas été prises en compte et un modèle de transport radial unidimensionnel plus simple a été utilisé :

$$v_{\perp,\alpha}(\rho) = -\frac{D_\alpha(\rho)\partial_\rho n_\alpha}{n_\alpha}$$

où $D_\alpha(\rho)$ est le coefficient de transport des particules, et v_{pinch} est la vitesse de pincement. Ni $D_\alpha(\rho)$ ni v_{pinch} ne sont calculés à partir des premiers principes. $D_\alpha(\rho)$ pourrait être fixé à une valeur uniforme ou être contrôlé par le code afin de s'adapter à un profil de densité d'ions radial prescrit $n_\alpha(\rho)$, où ρ est la coordonnée de surface de flux magnétique normalisé (égale à 0 sur l'axe magnétique et à 1 à la séparatrice).

L'un des avantages de l'utilisation de SOLEDGE3X comme modèle de plasma est que les espèces d'ions d'impureté sont entièrement couplées aux espèces d'ions principaux, ce qui signifie que les espèces fluides d'impureté exercent une force sur l'ion principal et vice versa. Dans le modèle de plasma fluide EMC3, par exemple, le transport des espèces d'impuretés est approximé par le modèle de trace d'impuretés [74], où la distribution des impuretés est calculée en utilisant les forces thermiques et de friction de l'ion principal, et l'ionisation et l'excitation des impuretés fournissent un puits d'énergie pour l'ion principal.

Une autre caractéristique de SOLEDGE3X qui en fait un choix intéressant est l'extension de la grille de calcul jusqu'aux CFP, ce qui permet de modéliser les interactions plasma-paroi de manière plus approfondie. Les cellules de la grille qui sont interceptées par la paroi sont masquées par ce que l'on appelle le « masque de pénalisation » qui fixe les conditions limites de la paroi dans ces cellules.

Bien qu'il soit possible d'utiliser les équations fluides pour les particules neutres également, cela nécessite l'hypothèse d'une collisionnalité élevée, c'est-à-dire le fait que le libre parcours moyen d'une particule neutre est plus petit que les longueurs de gradient du plasma, et ce depuis la source d'émission neutre (recombinaison d'un ion, recyclage) jusqu'à son d'ionisation. Cette hypothèse n'est généralement pas valable pour la plupart des particules neutres dans les plasmas de bord des tokamaks, le mouvement des particules neutres étant mieux décrit comme un mouvement balistique [75]. Pour cette raison, SOLEDGE3X est couplé à un code de transport de particules neutres cinétique, EIRENE [72]. EIRENE est basé sur le processus Monte-Carlo de génération d'ions test près de la surface de la paroi, où elles impactent le matériau de surface et génèrent des atomes et des molécules. EIRENE suit ensuite ces particules et décrit leurs interactions avec le plasma et les CFP. Ainsi, SOLEDGE3X fournit à EIRENE les paramètres du plasma pour générer des ions test et modéliser les interactions neutre-plasma, et EIRENE fournit à SOLEDGE3X les sources de particules chargées.

Le simulateur d'injection de poussières (Dust Injection Simulator, DIS) [71] est un code de suivi des poussières développé pour modéliser la dynamique des particules de poussière dans le plasma de fusion. Il utilise les paramètres du plasma donnés au modèle pour calculer la trajectoire d'une particule de poussière injectée et son taux d'évaporation le long de la trajectoire jusqu'à ce qu'elle soit complètement évaporée. Il prend en compte les forces de friction due aux ions, principaux et impuretés, et des neutres, les bilans de courant et d'énergie de la particule, ainsi que la fusion du matériau injecté, qui s'applique au bore. DIS a récemment été utilisé pour modéliser

les expériences d'injection de poudre par Nespoli et al [76] pour étudier la distribution des ions de bore dans les simulations d'expériences IPD sur le stellarator LHD.

Le processus de modélisation se compose de trois étapes principales. Tout d'abord, le plasma de la phase de précédant l'injection a été modélisé dans SOLEDGE3X-EIRENE (𝕊𝔼) avec deux espèces, D comme espèce ionique principale et O comme proxy pour toutes les impuretés légères présentes dans WEST avant l'injection de B, qui sont principalement B, O, C, et N [18]. Ensuite, les paramètres du plasma d'une simulation D+O donnée ($(n,T)_{e,i,n}$, nombre de Mach $\vec{M}$) sont exportés de 𝕊𝔼 vers DIS, où une particule B sphérique est lancée verticalement vers le bas depuis le haut de la machine. Ensuite, la distribution volumique de la source atomique neutre B est normalisé en fonction du taux d'injection de poudre B souhaité, et la source atomique B est ajoutée à la simulation 𝕊𝔼, ce qui donne des cas D+O+B représentatifs la phase d'injection d'une décharge avec injection de poudre B.

Les études numériques ont permis d'établir une correspondance quantitative entre certaines quantités du modèle numérique et les données expérimentales dans les phases précédant l'injection et d'injection ($(n,T)_e^{\text{targets}}$, n_e^{OMP}), et pour d'autres quantités, une correspondance qualitative a été obtenue (rapport $\Gamma_{\parallel}^{O^+}$ entre la phase d'injection et la phase de pré-injection, $S_{drop}/S_{pre-drop}$ au niveau du divertor haut). Un balayage des paramètres du plasma a été effectué pour étudier la sensibilité de la distribution de Γ^B à la variation de $(n,T)_e$, P_{in}, C_O^{core} et R_{IPD}. Les analyses ont montré que Γ^B varie très peu en fonction de ces paramètres, à l'exception de R_{IPD}. Bien que la position absolue de l'IPD sur la machine ne puisse être modifiée dans la pratique, le fort effet de R_{IPD} sur Γ^B dans les simulations montre que le transport de B dépend de la position relative de l'IPD et du plasma, en particulier de la position par rapport au point de stagnation.

Dans le scan de μ_B, R_B a été fixé à une valeur non nulle pour faire correspondre les mesures de spectroscopie visible des expériences avec les mesures synthétiques. La variation de μ_B a nécessité la réduction de $R_{D,O}$ pour faire correspondre $(n,T)_e^{\text{targets}}$ sur les plaques du divertor (« targets »). Ceci est cohérent avec les effets de l'injection d'impuretés dans les expériences, où l'injection d'une impureté qui n'adhère pas à une surface (par exemple N) causerait de forts changements de $(n,T)_e^{\text{targets}}$ et déclencherait finalement le détachement, alors que l'injection de poudre de B n'affecterait pas $(n,T)_e^{\text{targets}}$ de manière significative même à $\mu_B^{max} \approx 60$ mg/s.

4. Conclusions

Pour conclure la thèse, dans les deux séries d'expériences sur WEST, les effets positifs de l'injection de poudre de B sur le confinement, qui ont été observés pour la première fois dans les expériences préliminaires avec IPD, ont été confirmés et les principales causes de cette amélioration ont été établies : le gettering et la réduction du recyclage des principaux ions et des impuretés légères, ainsi que la réduction du transport des impuretés due à la dilution du plasma de bord, ont entraîné une augmentation de W_{mhd}, T_e^{central} et du taux de neutrons.

L'effet de réduction du recyclage est suggéré par les effets cumulatifs de l'injection de poudre de B dans les phases de pré-injection de chaque impulsion. Les raies B-II, O-II et W-I ont été sensiblement affectées par les injections des décharges précédentes, même lorsque μ_B ne dépassait pas le seuil de retournement de P_{rad}. L'effet était d'une ampleur similaire au conditionnement GDB, même pour des masses injectées nettement plus faibles.

Le piégeage des impuretés et la réduction de leur transport sont plus difficiles à discerner. D'une part, les effets de l'injection de poudre de bore sont clairement différents des effets de l'injection délibérée d'azote, car N n'adhère pas à la surface : $(n, T)_e$ varie plus fortement, et le plasma de divertor détache dans les expériences d'injection N, tandis que dans les expériences d'injection de poudre B/BN, les effets sur $(n, T)_e$ sont beaucoup plus légers, et n_e diminue même pour des μ_B suffisamment élevés. Cette différence peut être attribuée à l'effet de gettering qui se produit pendant l'injection de poudre, réduisant fortement le recyclage du deutérium et des impuretés à faible Z, compensant ainsi les électrons introduits par la poudre injectée. D'autre part, le gettering seul ne peut pas décrire de manière adéquate les effets de l'injection de poudre : dans la série à faible taux d'injection où le B et le BN ont été injectés dans des décharges avec les mêmes paramètres (P_{in}, n_e, configuration magnétique, etc.), la poudre de BN semble avoir un effet sur la raie visible O-II au niveau du divertor bas similaire à celui causé par l'injection de poudre de B, même si, en termes de masse, moins de la moitié de la poudre de BN est constituée de B qui peut air comme getter pour l'oxygène. En même temps, N rayonne plus que B par émission de raies, et étant donné que l'injection de N a également affecté le flux d'O mesuré spectroscopiquement par la technique du S/XB, on peut supposer que la rayonnement de raies plus intense, et par conséquent le refroidissement plus important de la SOL (pour « Scrape-Off Layer ») et les effets connexes sur le transport des impuretés, pourraient compenser la quantité réduite de B lors l'injection de poudre de BN.

Alors que l'effet de l'injection de poudre de B sur les impuretés légères semble être double, l'effet sur le transport du W semble être principalement déterminé par des changements du transport dans la SOL. La radiance de la raie W-I au niveau des plaques de divertor externes est linéairement corrélé avec μ_B dans les séries de taux d'injection plus élevés pour toute la gamme de μ_B, ce qui suggère une pulvérisation accrue du W par le B. La radiance de la raie W-I au niveau de la cible intérieure se comporte différemment, avec un retournement à $\mu_B \approx 30$ mg/s, qui semble être causé par le détachement partiel de la jambe intérieure du plasma. Néanmoins, le basculement de n_W^{core} et P_{rad} s'est produit à un seuil plus bas $\mu_B \approx 20$ mg/s, et n'a donc pas pu être causé par le détachement partiel de la jambe interne. L'augmentation du taux de pulvérisation du W avec une diminution de n_W^{core} suggère que la raison principale du retournement est l'effet du B injecté sur le transport du W, peut-être en supprimant le transport turbulent dans la direction transverse à B [64].

Lors du scan de μ_B et $R_{D,O}$ dans le modèle $\mathbb{SE}$, nous avons dû abaisser $R_{D,O}$ jusqu'à 0,58 pour $\mu_B = 15$ mg/s, ce qui est significativement plus petit que l'albédo de la pompe dans nos simulations $\mathbb{SE}$. En d'autres termes, dans les simulations, la paroi était un puits surfacique plus important que la pompe à vide. Un effet aussi important

sur $R_{D,O}$ pourrait être une surestimation causée par l'absence de transport turbulent dans les simulations avant la phase d'injection, qui aurait pu être supprimée par l'ajout de B.

5. Recherche future

Nous terminons par une proposition de recherche future dans ce domaine. Dans la partie expérimentale, il est souhaitable d'élargir le domaine opérationnel de l'IPD. Bien que, dans la série des taux d'injection plus élevés, μ_{max} et M_{max} aient tous deux été triplés par rapport aux expériences précédentes, M_{max} ne constituait encore que $\sim 10\%$ de la masse totale de B injectée dans une GDB. Étant donné que la majeure partie de cette masse a été injectée en trois impulsions, il est très réaliste et souhaitable d'atteindre $M \geq 10$ g en une seule session expérimentale afin, premièrement, de mieux comparer les techniques de conditionnement IPD et GDB et, deuxièmement, de vérifier si les effets de conditionnement saturent au-delà d'un certain seuil de M. Nous n'avons pas réussi à atteindre $M \geq 10$ g en raison d'un mauvais étalonnage de l'IPD, ce qui nous a obligés à depenser plusieurs impulsions pour injecter $\mu_B \approx 0$ mg/s.

Une autre façon d'étendre le domaine opérationnel consiste à augmenter P_{LHCD} pour obtenir un f_{rad} plus faible, qui agit clairement comme un facteur limitant pour les injections de IPD, comme on l'a observé par exemple dans les décharges chauffées par l'ICRH. Les décharges avec $P_{LH} \geq 5$ MW ont été récemment obtenues sur WEST, et il serait intéressant d'essayer d'injecter du B à des taux beaucoup plus élevés dans de telles décharges. Des injections IPD à 5 MW ont même été tentées à la fin de la campagne au premier semestre 2024, mais la machine n'était pas dans un état favorable, et toutes les impulsions ont été interrompues avant que l'injection de poudre de B n'ait pu être effectuée.

Un autre aspect de la partie expérimentale de la recherche qui mérite d'être discuté consiste à influencer Γ_B pour que le bore se répande de manière plus homogène, ou pour qu'il cible des CFP spécifiques. Comme le montre le balayage de RI PD dans la modélisation $\mathbb{SE}$, la position relative de l'IPD par rapport au centre du plasma/SOL peut être un élément clé pour affecter la distribution de Γ_B en modifiant le mouillage des CPP par le plasma. Une autre configuration qui n'a été prise en compte ni dans les expériences ni dans la modélisation est la configuration magnétique en limiteur. D'une part, un plasma limité sur un PFC W devrait mieux conditionner ce PFC lors de l'injection de poudre B. D'autre part, la configuration limiteur dans WEST est généralement réalisée sur des tuiles en BN qui ne nécessitent pas de boronisation, et la limitation du plasma sur une surface W peut entraîner une augmentation de f_{rad} telle que l'injection de poudre B deviendrait impossible.

Il serait également intéressant d'essayer de discerner entre l'effet de piégeage et les effets sur le transport des impuretés dans la SOL, par exemple en injectant en même temps du B et du BN à différents ratios afin de comparer les effets pour différentes valeurs de μ_N/μ_B. Pour cela, un étalonnage plus robuste serait nécessaire et des taux d'injection plus élevés sont souhaitables pour disposer d'un espace opérationnel plus

grand ($\mu_B + \mu_N, \mu_N/\mu_B$) à analyser.

Des études sur des échantillons de W exposés à l'injection de poudre de B à l'aide, par exemple, de la spectroscopie de désorption thermique seraient utiles pour mieux comprendre les effets des dépôts de B introduits par l'IPD sur la rétention de D et d'impuretés. L'analyse comparative de ces échantillons avec des échantillons analogues de GDB permettrait de mieux comprendre les similitudes et les différences entre les deux approches du conditionnement des parois.

En ce qui concerne la partie de la recherche relative à la modélisation numérique, de nombreux domaines peuvent être améliorés. On pourrait essayer de modéliser toute la gamme des μ présents dans les expériences. Les simulations avec $\mu > 15$ mg/s n'ont pas pu converger dans un temps suffisant en raison d'un petit pas de temps causé par de grandes dérivées temporelles des champs. Une façon d'aborder ce problème est de faire un compromis sur la résolution spatiale des modèles : le pas de temps est également limité par la taille des cellules du maillage, de sorte que le choix de ne pas résoudre certains détails peut aider à atteindre la convergence de l'équilibre des particules. Une autre solution consiste à ajouter progressivement B par étapes chaque fois que l'équilibre du contenu en particules est atteint.

Un autre domaine d'amélioration de la modélisation est la prise en compte de la non-axisymétrie des CFP et de la source de bore. Pour l'instant, EIRENE ne fonctionne pas dans les simulations 3D de SOLEDGE, ce qui signifie que les calculs 3D devraient être effectués avec des fluides neutres, à moins que l'interface STYX d'EIRENE ne soit mise à jour. Il serait intéressant d'analyser les différences entre les modèles neutres cinétiques et les modèles neutres fluides par rapport aux modèles SOLEDGE des expériences IPD - pour savoir si les neutres fluides sont un modèle adéquat pour comparer aux données expérimentales et dans quelles conditions cela est vrai.

Les simulations $\mathbb{SE}$ présentées dans notre étude n'incluent pas les dérives « transerves à B », c'est-à-dire $\vec{E} \times \vec{B}$, $\vec{B} \times \nabla B$, etc., ni le transport turbulent. L'inclusion de chacun de ces éléments pourrait affecter la distribution poloïdale de $\Gamma^i_{\parallel}$, modifiant la distribution finale de Γ^B sur les CFP.

Acknowledgements

I wish to thank the many people who supported me during my work. In particular, my supervisor Alberto Gallo was encouraging and helpful throughout the doctoral studies, helping me to explore the physics behind the problem posed by this thesis and preparing me for my defence. Yannick Marandet provided guidance and feedback on the STYX interface extension in the beginning of the studies. I would also like to thank Philippe Moreau for all the help and encouragement, as well as the entire WEST Team, and in partular Francis-Pierre Pellissier and Matthieu de Combarieu for the support in setting up and conducting the experiments. I thank my family, my father and my mother for all the teaching that they gave me to reach this point.

Table of Contents

Affidavit ii

List of publications and conference contributions iii

Abstract and keywords in English iv

Résumé et mots clés en français v

Résumé étendu en français vi

Acknowledgements xvi

Table of Contents 1

1 Introduction 3
- 1.1 Nuclear fusion . . . 3
- 1.2 Magnetic confinement and tokamaks . . . 4
- 1.3 Plasma-wall interaction in a tokamak . . . 7
- 1.4 ITER project goals and challenges . . . 8
- 1.5 WEST description . . . 9
- 1.6 Wall conditioning in W tokamaks . . . 11
- 1.7 Real-time wall conditioning with B powder injection . . . 12
- 1.8 Impurity powder dropper description . . . 14
- 1.9 Computational modeling of IPD experiments . . . 16
- 1.10 Goals of the study . . . 18

2 Experiment description and results 19
- 2.1 Methodology of B powder injection experiments . . . 19
  - 2.1.1 WEST experimental setup . . . 19
  - 2.1.2 IPD experimental setup . . . 23
- 2.2 Objectives for the dedicated experiment . . . 23
- 2.3 B and BN powder injection experiment description . . . 24
  - 2.3.1 Transient effects of B powder injection at high drop rates . . . 25
  - 2.3.2 Cumulative effects of B powder injection . . . 36
- 2.4 BN powder injection experiment results . . . 39
- 2.5 Summary of the experimental part of the thesis . . . 42

3 Modeling workflow description and results of the computational analysis **43**
3.1 Modeling workflow description 43
3.1.1 Boundary plasma modeling with SOLEDGE3X-EIRENE 43
3.1.2 Dust Injection Simulator 44
3.1.3 Modeling of IPD experiments in WEST 45
3.2 Workflow test and parameter scan with constant $D(\rho)$ 47
3.3 Scan of P_{in} and C_O^{core} with a feedback on $D(\rho)$ 52
3.4 Scan of B drop rate and recycling coefficients 59
3.5 Scan of input parameters in the revised model 63
3.5.1 Scan of P_{in} and n_e^{OMP} 63
3.5.2 Scan of the radial position of IPD 64
3.6 Summary of the modeling part of the thesis 68

4 Discussion of the results **69**

5 Future research **73**

References **74**

1 Introduction

1.1 Nuclear fusion

Nuclear fusion of hydrogen isotopes (hydrogen H, deuterium D, tritium T) and helium He is being studied in the hopes of developing a new source of energy. The principle of nuclear fusion is grounded in the fact that the *nuclear binding energy* (minimum energy required to disassemble the nucleus of an atom into the protons and neutrons) generally increases with the mass of the element, up to a limit of iron-56. Because of that, the fusion of two light nuclei releases the excess of the binding energy in the kinetic energy of the fusion products and/or photon emission. The exhaust energy can then be used to boil water and spin turbines, producing electricity similar to nuclear fission power plant operation through nuclear transmutation.

A major difference between nuclear fusion and fission is the stability of the fuel. In nuclear fission unstable isotopes of uranium U are used, which split spontaneously, and it is simple to increase U reaction rate by increasing the neutron flux to the fuel. In nuclear fusion, however, the reaction requires the fuel atom nuclei to get close to each other to fuse, which does not happen spontaneously and requires external forces to overcome the repelling of nuclei. The fuel, depending on the reaction of choice, is either a stable isotope (H, D, He^3, He^4) or unstable T, whose decay is detrimental to the operation of the hypothetical fusion power plant. The energy released in T decay is 18.6 keV, while in one of the most promising fusion reactions D-T total energy production is 17.6 MeV:

$$ {}_1\mathrm{D}^2 + {}_1\mathrm{T}^3 \rightarrow {}_2\mathrm{He}^4\ (3.5\ \mathrm{MeV}) + {}_0\mathrm{n}^1\ (14.1\ \mathrm{MeV}) $$

To achieve this reaction the nuclei must be put in close proximity against the repelling electrostatic force. This can be done by either packing the fuel at a very high density and heating it, which is typical for *inertial confinement fusion* where fuel pellets are compressed and heated with lasers for a short period of time (10^{-11} to 10^{-9} s), or by heating a fuel-containing thermonuclear *plasma* (highly ionized gas) at a lower density and higher temperature with a much longer pulse time (10^{-3} to 10^{3} s), as it is done in *magnetic confinement fusion*.

For the reaction to be self-sustaining, i.e. for the heating from He^4-particles produced by the D-T reaction to be sufficient to maintain the thermonuclear conditions, the fuel density n needs to be as high as possible to maximize the rate of reactions; their temperature T must be as high as possible for the same reason; the energy confinement time τ_E must also be maximized to prevent the plasma from cooling down too fast. All these parameters can be brought together into a *triple product* $nT\tau_E$, which

in the case of D-T reactions must satisfy the criterion for the self-sustainability or *ignition*, also called Lawson criterion:

$$nT\tau_E > 3 \times 10^{21} \mathrm{m}^{-3}\ \mathrm{keV\ s} \qquad [1]$$

1.2 Magnetic confinement and tokamaks

The optimum temperature for the D-T reaction is around 10 keV, or 10^8 K. Such high temperatures prevent the confinement of the plasma with material walls. A better approach is to leverage the almost full ionization of the plasma by placing it in a strong magnetic field.

In a uniform magnetic field $\vec{B}$, the motion of a charged particle in the plane perpendicular to $\vec{B}$ in the absence of other forces is limited to gyration with a Larmor radius $\rho_g = \frac{mv_\perp}{|q|B}$. In other words, the motion of a charged particle in such arrangement is limited to the inertial motion parallel to $\vec{B}$ and to rotation around a fixed field line, and it can be thought of as being confined within ρ_g of the field line that serves as an axis of rotation. The motion along the magnetic lines is not, however, restricted in any way. In order to confine charged particles in a finite volume, the magnetic field can be closed into a toroidal loop. This configuration would make $\vec{B}$ non-uniform, but if the external magnetic field is strong and uniform enough, or:

$$\frac{\delta B}{\delta r} \ll \frac{B}{\rho_g},$$

then the charged particles will move mostly along the magnetic field lines with their parallel velocity $v_\parallel \gg v_\perp^{\mathrm{drift}}$, where $v_\perp^{\mathrm{drift}}$ is the velocity of a particle drift across the magnetic field lines caused by the non-uniformity of $\vec{B}$ and the presence of other fields. For example, the presence of an electric field $\vec{E}$ perpendicular to the magnetic field will cause the particle to drift in the direction $\vec{E} \times \vec{B}$ with the velocity $v_d = E/B$.

A device designed to produce such a toroidal magnetic field to confine plasma in the vacuum is called *tokamak*: a toroidal vessel with magnetic coils in Russian. A schematic representation of a tokamak is presented in figure 1.1. In the direction around the axis of symmetry of the tokamak φ, or *toroidal* direction, the magnetic field $\vec{B_\varphi}$ is created with toroidal field magnets wrapped around the chamber. The *poloidal* magnetic field $\vec{B_\theta}$ that lies in the plane perpendicular to the toroidal direction and is curved around the *magnetic axis* of the tokamak is created with the plasma current $\vec{I_p}$, which is induced with a central solenoid. $\vec{I_p}$ serves as an ohmic source of heat for the plasma, and $\vec{B_\theta}$ serves to stabilize the confinement of the particles by mixing drifting particles in poloidal direction. The sum of $\vec{B_\varphi}$ and $\vec{B_\theta}$ produces total magnetic field $\vec{B}$, magnetic lines of which form nested toroids, with a *Last Closed Flux Surface* (LCFS) as the boundary between the flux surfaces that are confined in the vessel and the flux surfaces that intersect the vessel walls. The distance between the center of the tokamak and the magnetic axis is called the *major radius* R_0 of the

tokamak, and the distance between the magnetic axis and the vessel walls or LCFS is called the *minor radius a*. Ratio $q = \frac{aB_\varphi}{R_0 B_\theta}$ is called *safety factor*, and it describes how many rotations in toroidal direction are necessary for a magnetic field line to return to the same poloidal position starting from a given point. In other words, q refers to the "windiness" of the toroidal magnetic field, that is, it is equal to the pitch of the magnetic field $\frac{d\varphi}{d\theta}$. Generally, high values of q lead to greater plasma stability, as flux tubes with rational values of $q = m/n$ with $n \sim 1$ form resonant surfaces, enhancing plasma instabilities [1].

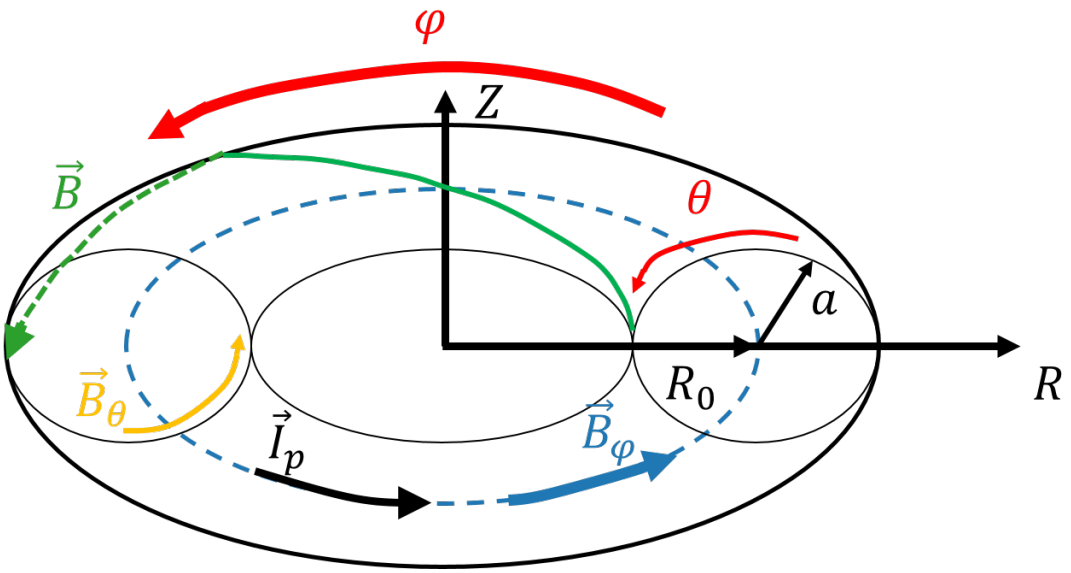

Figure 1.1. Schematic representation of a tokamak

Magnetic configuration in a tokamak refers to the shape of the magnetic field in the poloidal section. In a *limited* configuration the flux surfaces form nested ellipses and LCFS is defined by a material *limiter* that gets eroded by the *Scrape-Off Layer* (SOL) plasma outside LCFS, allowing the material to enter directly in the *confined region*, i.e. the region where the magnetic field lines are closed within the vessel (figure 1.2a, yellow region). In *diverted* configuration, the magnetic field is modified by introducing secondary magnetic axes outside of the vessel, dividing the magnetic field between the confined region and the SOL (figure 1.2b, blue region), where field lines cross the walls. Most of the particle and heat flux in that configuration flows from the confined plasma to the part of the wall that is intersected by the *separatrix*, a boundary between the areas of the tokamak with closed and opened magnetic field lines. The magnetic field lines outside of the separatrix are not truly open, of course, but instead they are closed outside of the vessel walls. In diverted plasmas most of the particles that drift across the separatrix from the confined plasma to the SOL due to the variation of $\vec{B}$ and presence of other forces get flushed along the magnetic field lines on the *divertor* targets, which is the part of the wall that is intersected by the separatrix and the SOL field lines. Since the magnetic field lines near the divertor do not enter the

plasma volume within the separatrix, the plasma near the divertor is decoupled from the confined plasma, thus reducing its contamination with the divertor material. In both cases, the peripheral portion of the confined plasma, the edge, together with the SOL will be referred to as *boundary plasma* in the following.

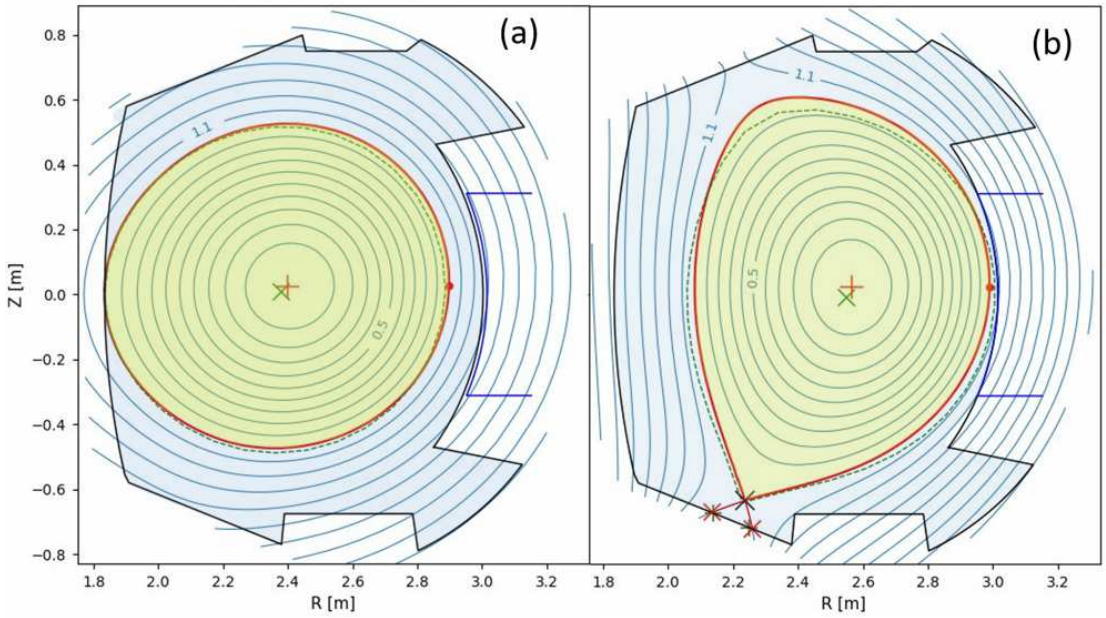

Figure 1.2. Limited (a) and diverted (b) magnetic configuration in WEST tokamak, with LCFS in red, confined plasma in yellow, scrape-off layer in blue. Detailed description of PFCs is given in figure 2.1

A typical lifecycle of a charged particle in the confined plasma consists of a slow cross-field transport toward the separatrix, followed by a rapid transport along the open field lines to the first wall, where plasma-wall interactions occur. In the most common assumption for ion transport description, the transport of a charged species i across the field lines can be considered a one-dimensional diffusivity problem:

$$\Gamma_{\perp}^{i} = -D_{\perp}^{i} \frac{dn_i}{dr}.$$

A schematic representation of the transport is shown on figure 1.3. For simplicity of representation of the transport the SOL was straightened such that the confined plasma is located in the area beneath separatrix, and the SOL is located between two wetted wall elements. Once the charged particle crosses the separatrix, it travels to the plasma-facing component (PFC) with $v_{\parallel} \gg v_{\perp}$. The distance L_c between the SOL entry point and the PFC is the *connection length* of the tokamak, which depends on the geometry of the wall and the magnetic field. The width of the SOL is given by the density exponential decay length λ_n and it is in the centimetric range, given by the equation 1.10 in [2]:

$$\lambda_{\mathrm{SOL}} = \sqrt{\frac{D_\perp L}{c_s}}$$

and for typical SOL values: $D_\perp = 1\ \mathrm{m}^2\ \mathrm{s}^{-1}$, $L = 50$ m, $c_s = 5 \times 10^4\ \mathrm{m\ s}^{-1}$. This leads to the concentration of the power exhaust on thin rings on the divertor around the strike points (intersections of the separatrix and the PFC).

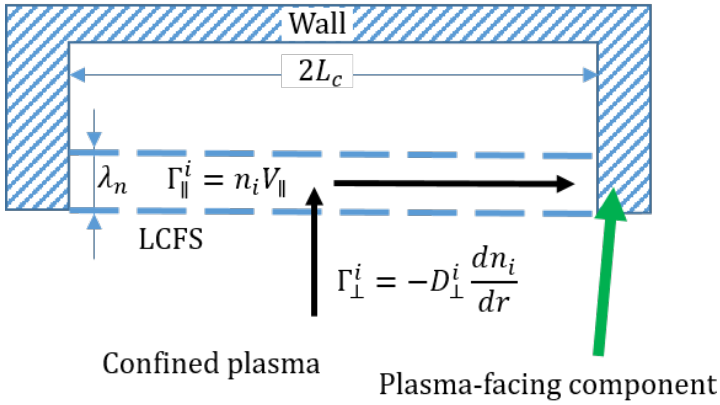

Figure 1.3. Schematic representation of particle transport in tokamaks with a straightened out SOL, similar to figure 1.13 in [2]

1.3 Plasma-wall interaction in a tokamak

One of the features of tokamak plasmas crucial for their study is the presence of *impurities*: non-fuel ions, which are either introduced inadvertently from the vessel walls into the plasma through the air or coolant leaks, plasma-surface interactions and/or oxide formation during the venting of the machine, or injected intentionally for e.g. protection of the PFCs via radiative cooling. In the confined region impurities worsen the capacity of the plasma for fusion is several ways. Firstly, the impurity ions introduce a power loss through line radiation when they are not fully stripped. This problem is exacerbated with the atomic charge of the impurity: with the increase of the atomic charge the number of ionization states also increases, leading to greater radiation loss. Secondly, the presence of impurity ions dilutes the fuel. The impurity ions come with a number of electrons, and for a given plasma pressure the partial concentration of fuel ions is reduced, and the fusion rate is decreased. Both issues are detrimental to the maximization of $nT\tau_E$. Impurities can also lead to plasma *disruptions*: strong cooling of the plasma can affect the current profile and thus change the poloidal field, triggering MHD instabilities and leading to the rapid loss of the particle and heat confinement. Disruptions can cause first wall material damage, which in turn can create more impurity sources at the wall.

One of the sources of impurities in reactor-grade tokamaks is He produced during the fusion reactions, usually referred to as *He ash*. While He ash removal is of great importance for fusion reactor development, it can be disregarded for smaller-scale experimental tokamaks.

The other source of impurities are the PFCs, which release them into the plasma during various interactions. Impurities like nitrogen (N), oxygen (O), water vapor can enter the vacuum chamber in the case of imperfect vacuum conditions or during the vent of the chamber which can be necessary to perform maintenance of the machine. *Sputtering* is a process in which high-energy ions, either fuel or impurities, strike the PFCs and release wall material into the plasma. The ions from that material can continue that process, in which case the material is said to be *self-sputtered*. Another source of impurities is the recombination of incident ions in the boundary plasma, followed by back-scattering and ionization, in the process called *recycling*.

While the presence of impurities in the confined plasma is detrimental to the maximization of $nT\tau_E$, the presence of impurities in the SOL in diverted configuration can also be helpful. Considering that the parallel transport of charged particles is a lot faster than the perpendicular transport, most of the heat and particle flux on the PFCs comes from the particles that drifted across the separatrix to the SOL, where they get swiftly transported to the wetted areas of the PFCs, mainly divertor targets. If the SOL plasma contains impurities, it can radiatively cool down the plasma, causing it to disperse the energy isotropically in the form of electromagnetic radiation, instead of directly transferring that energy to the PFCs via conduction and convection.

1.4 ITER project goals and challenges

As shown in the previous section, choice of the first wall material is a crucial part of the tokamak design due to the importance of the plasma-wall interactions. Earlier tokamaks, e.g. T-3 used stainless steel [3], which was poorly resistant to structural damage due to heating and melting, and had an unfavourable combination of relatively high sputter yield and impurity radiation losses. Carbon (C) in form of graphite was then favored over these materials, due to its high sublimation temperature and the absence of surface instability caused by melting [4]. While C PFCs permitted high-performance plasmas, i.e. plasma pulses with higher triple product, to be obtained, D release during discharge and unaccepably high T retention were an obstacle on the path to a reactor-grade tokamak [5].

To reduce T retention, ITER design included PFCs made with beryllium (Be). It has a lower rate of H isotope retention. While Be has a lower melting point when compared to the sublimation temperature of C, it is partly offset by its larger thermal conductivity. In addition, Be codeposits with T are more local than that of C, which formes hydrocarbons with T that get transported in remote locations.

The ITER tokamak is being developed to study reactor-grade plasmas, with the goal of achieving *net fusion energy gain* $Q = 10$, where Q is the ratio between the produced fusion power and heating power [6]. One of the initial designs for ITER featured full-Be

first wall with divertor PFCs made either of a C fiber composite and tungsten (W) elements [7]. The need for the different divertor materials arises from the lower heat flux capacity of Be first wall components, up to ~5 MW m^{-2} for the "enhanced heat flux" panels and ~2 MW m^{-2} for the "normal heat flux" panels, while the ITER divertor was developed to withstand up to ~10 MW m^{-2} in steady state[8].

While Be has its advantages described above, it also has its disadvantages in the form of dust formation and low resilience to thermal loads due to unmitigated or partially mitigated disruptions [9]. Be dust formation effectively increases the surface area for the interaction of H isotopes with wall material, leading to an increased T retention and effectively lowering the allowed T inventory capacity for ITER operation, as well as generating toxic Be dust, which presented a potential hazard in case of a leak. Thermal transient loads can cause drastic reduction of PFC component lifetime. Lastly, Be is a toxic metal that requires expensive handling. For these reasons ITER baseline design was changed in favor of a full-W first wall [10].

Replacement of Be with W in the first wall design has potential positive impacts related to T retention, dust production and resilience to disruption thermal loads, but it also increases the risk related to a potentially increased core plasma radiation, which could make $Q = 10$ goal harder to achieve. For these reasons the study of plasma-wall interactions in existing full-W tokamaks is important to test and improve ITER design.

1.5 WEST description

The W Environment Steady-state Tokamak (WEST) is a tokamak with full-W PFCs which, among other studies, is also used as a testing ground for ITER W divertor design [11] [12]. The main characteristics of WEST are given in table 1.1. Important characteristics that make WEST an excellent test subject for ITER divertor is the presence of an ITER grade, full W, actively cooled lower divertor [13] [14] and long pulse capability. WEST divertor was designed to test ITER-relevant divertor heat loads of ~10-20 MW m^{-2}, as well as particle fluence of ~ 10^{27} D m^{-2} and plasma pulse duration of ~ 1000 s. During the experimental campaign of 2024 WEST achieved a record pulse duration of over 6 minutes, with ~3 MW of heating power and line-integrated density in the equatorial plane $\langle n_e l \rangle_{\text{central}}$ of $\sim 3 \times 10^{19} m^{-2}$ (figure 1.4). The limiting factor for the pulse was the gradual temperature increase of non-actively cooled vessel components which led to the outgassing of the remote regions of the vessel, causing n_e increase and I_p decrease at $t = 350$ s.

A significant part of research on WEST is centered around the study of W erosion and transport, the mitigation of the heat loads and W sputtering. For example, W PFCs were studied *in situ* after the first three years of the operation [15], and it was shown that the damage to W PFCs comes from singular high-load events (disruptions, electric arc formation etc) rather than from the continuous heating. N injection helped to decrease W sputtering by reducing the SOL plasma temperature, leading to improved confinement properties and higher central temperature [16]. One of the domains of plasma-wall interaction studies relevant for this thesis is *wall conditioning*, which is

Major radius, m	2.5
Minor radius, m	0.50
Toroidal magnetic field, T	3.7
Plasma current, MA	< 1.0
Nominal pulse duration, s	1000
LH heating, MW	≤ 5

Table 1.1. WEST machine parameters

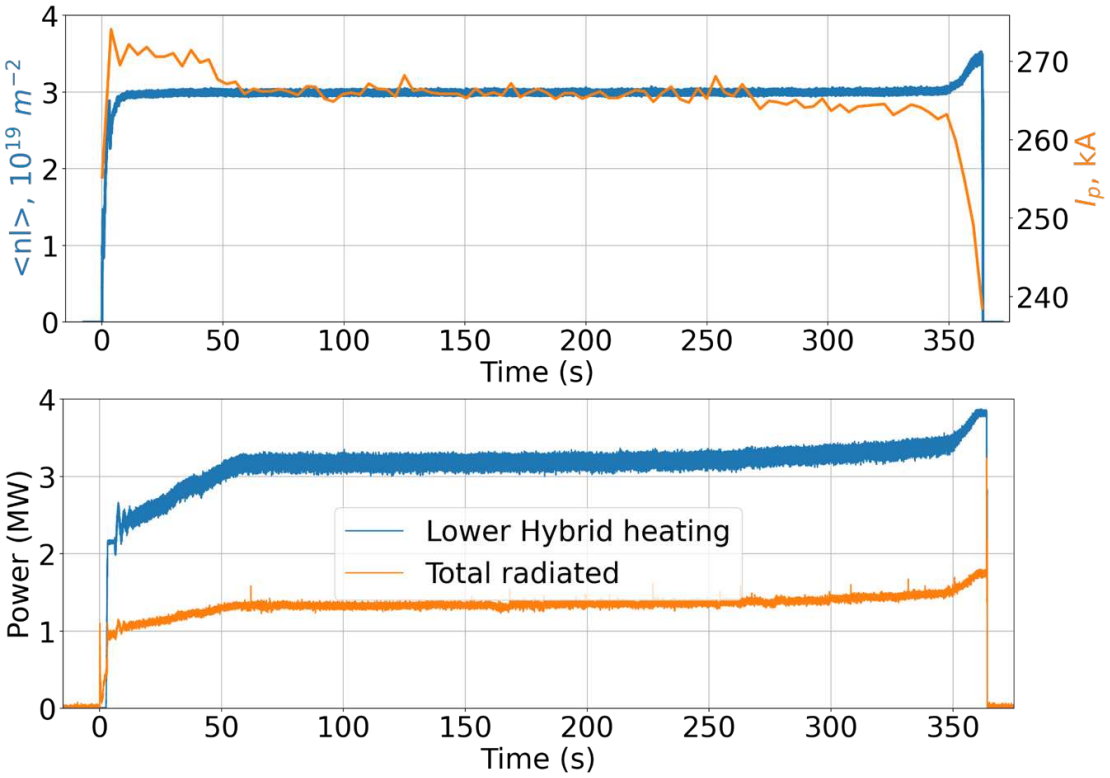

Figure 1.4. Time traces of heating and total radiation powers, central line-integrated density and plasma current in the record-long WEST pulse, $t_{\text{duration}} = 365$ s

also actively studied on WEST.

1.6 Wall conditioning in W tokamaks

While the use of W has some benefits that are important for improving power exhaust — lower T retention when compared to C which binds chemically with H isotopes and Be which forms dust, higher melting temperature than that of Be and also no toxicity, unlike Be — plasma contamination with W is exceptionally problematic due to high atomic number of W $Z_W = 74$, considering that the critical tolerated impurity concentration is roughly proportional to $1/Z^2$ [17]. Because of its high Z, W is still only partially ionized even in the center of the plasma, causing radiative losses up to the plasma core, thus leading to the reduction of energy confinement.

One of the causes of W contamination is the sputtering of W walls by low-Z impurities, which in case of WEST are mostly C (typical peak flux $\Gamma^C_{peak} \sim 5 \times 10^19$ ions/m^2/s) and O ($\Gamma^O_{peak} \sim 7 \times 10^18$ ions/m^2/s) [18]. O is introduced during the venting of the vessel and through the air leaks in the form of oxide formation with the O in the air, water vapor deposits and gas adsorption. C source is present in the vessel in form of the graphite substrate of W PFCs.

To mitigate W sputtering, a *conditioning* is performed, which is a process that involves treating the first wall to reduce the quantity of deposited residue and/or to trap it in the wall material, thereby inhibiting their sputtering and the subsequent sputtering of W. Several wall conditioning methods are utilized in W tokamaks, some of which are also used in machines with other wall materials. *Baking*, which involves subjecting the PFCs to high-temperature treatment, facilitates the removal of adsorbed gases and water, and is used in both W tokamaks and other machines [19]. Another approach, *glow discharge cleaning*, uses D_2 or He glow discharges, causing bombardment of the first wall with ions, removing impurity deposits[20]. Additionally, *glow discharge boronization* (GDB) is employed in tokamaks with high-Z walls like W and nickel, where a glow discharge is generated with a diborane (B_2D_6) atmosphere [21] [22] [23].

During GDB in WEST, the vessel is filled with He at a pressure of 0.5-0.7 Pa. A glow discharge is performed by creating a potential difference of ~500 V between positively charged electrodes mounted in the vessel and negatively charged tokamak wall, and B_2D_6 diluted with He is puffed. The glow discharge causes B_2D_6 to disassociate and B atoms to ionize. B ions are then transported to the negatively charged vessel walls, where they form a deposit. This boron layer with the thickness of ~30-50 nm serves a dual purpose: it encapsulates residual O beneath the boron deposits and reduces D and O recycling in subsequent plasma pulses, enabling improvements in density control and reducing the sputtering of the walls by low-Z impurities.

1.7 Real-time wall conditioning with B powder injection

While GDB is utilized in present W tokamaks [24] [25] and is also envisioned in ITER in view of full-W PFCs [9], it has some operational limitations relevant for reactor-grade devices. Considering that the B deposits are getting worn out as the plasma time is accumulated, GDB might not be suitable for long-pulse operations, since it can only be performed in the absence of plasma and the process takes multiple hours. Lastly, GDB requires the use of highly toxic B_2D_6. For these reasons, an alternative approach to boronization is being developed in the form of *B powder injection with an impurity powder dropper* (IPD) [26].

The main idea behind the real-time wall conditioning is an injection of an impurity that getters oxygen and hydrogen in a form of a powder during a plasma pulse. As the impurity powder reaches the boundary plasma it will melt, evaporate and ionize, and the injected impurity ions will be subject to the same transport dynamics that were described in the sections above. On one hand, the transport of the injected impurity in poloidal direction depends on q: with bigger q the rotational transform $\iota = q^{-1}$ is smaller. ι refers to a number of poloidal rotations of a magnetic field line, and thus of a trajectory of a charged particle, per one toroidal rotation. On the other hand the *connection length* L, i.e. the typical length a charged particle has to travel in the SOL before reaching a PFC, in diverted configuration is proportional to q [2]:

$$L \approx \pi R q.$$

Thus in the first-order approximation it can be assumed that injected impurities will travel $\sim \pi$ in poloidal direction before reaching the PFCs, and that B will be distributed uniformly in poloidal direction because of that. The actual distribution of the injected impurity depends on the force balance near the PFCs [27], subsequent re-erosion and redeposition [28] [29].

Once the injected ion reaches the PFC it is expected that it will recombine and be deposited on the first wall similarly to B in GDB, with the difference that in GDB B is ionized by a glow discharge, while in a real-time boronization with an IPD B is ionized by the tokamak plasma, which would affect the distribution of the B deposition due to the magnetic field geometry. For example, it is expected that the divertor would receive a greater influx of B compared to other PFCs. The motivation for the B powder injection is similar to the motivation behind GDB: the *gettering* (i.e. capture in the deposit layers) of light impurities and the reduction of D and light impurities' recycling.

Lithium (Li) and B were used as the impurities in IPD injections, with Li tested on EAST [30] [31] [32], DIII-D [33], and NSTX [34], and with B injected in: DIII-D [35] [36], EAST [37] [38] [39] [40], AUG [41] [42] [43], KSTAR [44], LHD [45] [46] [47], W7X [48], and WEST [49] [50].

In Li injection experiments the following effects were observed:

- In EAST Li injection studies [30] an H-mode was achieved by injecting Li aerosol

into the plasma. Injected Li suppressed ELMs while increasing edge turbulence with an edge coherent MHD mode, increasing particle exhaust, thus preventing impurity accumulation.

- In the following Li injection experiments in EAST active control over divertor recycling of D was achieved [31], as well as the ion fluxes of W, molybdenum and C [32].
- In DIII-D experiments Li injection facilitated the transition to the enhanced phase of the pulse, causing a decrease of the core concentration of other impurities and radiated power,improved energy confinement, reduced the divertor heat fluxes and improved wall conditions [33] [35].
- In NSTX two Li injection methods were tested: powder injection and Li evaporation from divertor plates [34]. Li injection appeared to be more effective than the evaporation method since it required only a fraction of Li to be injected to achieve similar improvements in the energy confinement and the edge stability.

In numerous B-containing powder injection experiments the following effects were observed:

- Reduction of wall fueling and reduced recycling ([35], [40], [41], [42], [44], [46], [47], [49], [50]);
- Formation of B-containing layers ([35], [41]);
- Increased divertor detachment ([36]);
- Reduction and/or suppression of edge-localized modes ([36], [37], [40], [44]);
- Excitement of an edge harmonic mode that provided enhanced particle exhaust ([38]);
- Reduction of impurity core concentration ([39]);
- Improved confinement ([42], [43], [48], [49], [50]).

Performing boronization with B powder injection has some attractive properties when compared to GDB. First, it can be performed on-demand, without having to power the magnetic coils off and on, which is relevant for long-pulse tokamak operation since GDB cannot be performed in a middle of a plasma pulse and requires the toroidal field to be turned off, unless it utilizes plasmas generated with electron-cyclotron or ion-cyclotron heating. Second, it involves B in powder form, which is practically inert when compared to toxic B_2D_6.

In B powder injection experiments cited above, multiple positive effects of B powder injections were reported. For example, they were observed on WEST during IPD commisioning campaign [49]. In these preliminary experiments 310 mg of B were

injected in total over 9 pulses with a maximum achieved drop rate between 9 and 17 mg/s. Firstly, the conditioning effect of B powder injections was observed in the form of the reduction of line radiance of O-II, N-II and C-II lines as the cumulative mass of the injected powder grew, indicating the lowered recycling and gettering of the light impurities by the injected B. Density-normalized total radiated power $P_{\text{rad}}^{\text{total}}/\langle n_e l\rangle_{\text{central}}$ also experienced a similar reduction with the increase of cumulated B mass, with the conditioning effect being reset after a disruption, suggesting that the B deposits get damaged by the disruptions, freeing the captured impurities. Secondly, during the B powder injection line radiances of D and O were transiently decreasing while W-I line radiance increased, suggesting that while injection of B transiently reduces the sputtering and recycling of the main ion and other light impurities, it itself causes W sputtering. In addition, B powder drop rate positively correlated with the stored energy W_{MHD} estimated from the plasma pressure determined by the magnetic equilibrium reconstruction, the neutron rate, which serves as a metric of the fusion reaction rate, and electron temperature T_e. All these metrics imply an improved confinement of the plasma, which is relevant for the triple product maximization.

1.8 Impurity powder dropper description

The impurity powder dropper (IPD) is a device developed by A. Nagy and collaborators at the Princeton Plasma Physics Laboratory [26] for controlled injection of impurity powders. The main part of the device is a powder *feeder*, depicted in figure 1.5(a). The feeder consists of a horizontal trough, connected to piezoelectric actuators that can be put to vibrating motion by applying an alternating voltage. When the feeder is activated, the trough starts shaking together with a powder-filled funnel that acts as a secondary reservoir. The funnel is vibrated to prevent powder flow instabilities, and it is filled by the primary reservoir, which is mechanically decoupled from the rest of the feeder. To perform a powder injection, an alternating sinusoidal voltage is applied with a frequency close to the harmonic oscillation frequency of the feeder, which is determined in advance via a calibration.

Four feeders are assembled in a vacuum chamber to form the top part of an IPD. The vibrating part of each feeder is equipped with a copper weight, introducing a change in the resonance frequency of the feeder to mechanically decouple it from the rest of the device. The troughs point into a vertical tube, mounted to a torus interface valve (TIV). TIV contamination by powder is undesired because the TIV may not be able to shut itself vacuum-sealed in the presence of powder if the IPD needs to be dismounted or pressurized. To prevent the powder from falling on the TIV during calibration and testing a TIV protector is installed connected to the vertical tube, as shown in figures 1.5(b), 1.6, 1.7. TIV protector is a blade that separates the valve and the feeders, preventing powder spilling on the TIV. The powder can be dropped into a catch-can for calibration measurements and to perform IPD tests without actual powder injection in the vessel. The vertical tube is equipped with an LED-based *flowmeter*, which consists of an LED light and a photoelectric sensor on the opposite sides of the vertical tube,

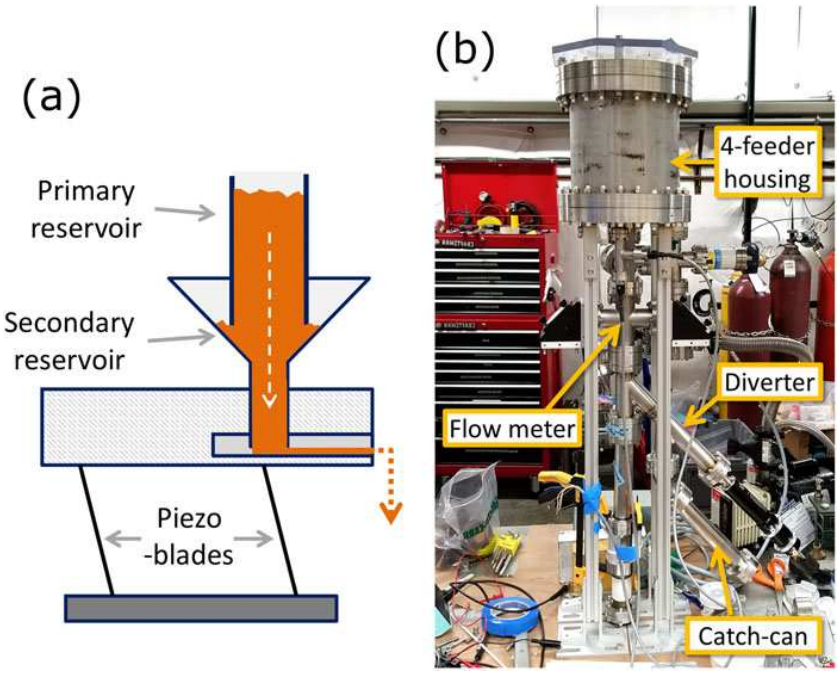

Figure 1.5. (a) Vertical cross-section of an IPD feeder, with a flow of powder from the primary reservoir into the secondary and the trough. (b) Assembled IPD on a test bench, with four feeders in the top chamber. From [26]

optically connected with two mirrors (figure 1.6). Voltage measurements from the sensor in the absence of powder varied around 12 V depending on the alignment of the mirrors.

In B powder injection experiments the feeders are filled with B powder (particle diameter $d_p^{\mathrm{B}} \leq 150\ \mu$m) or with boron nitride (BN) powder (particle diameter $d_p^{\mathrm{BN}} \leq 40\ \mu$m). During an experiment, the powder is dropped into the tokamak plasma, where it gets evaporated, ionized, transported along the magnetic field lines, and is eventually deposited on PFCs.

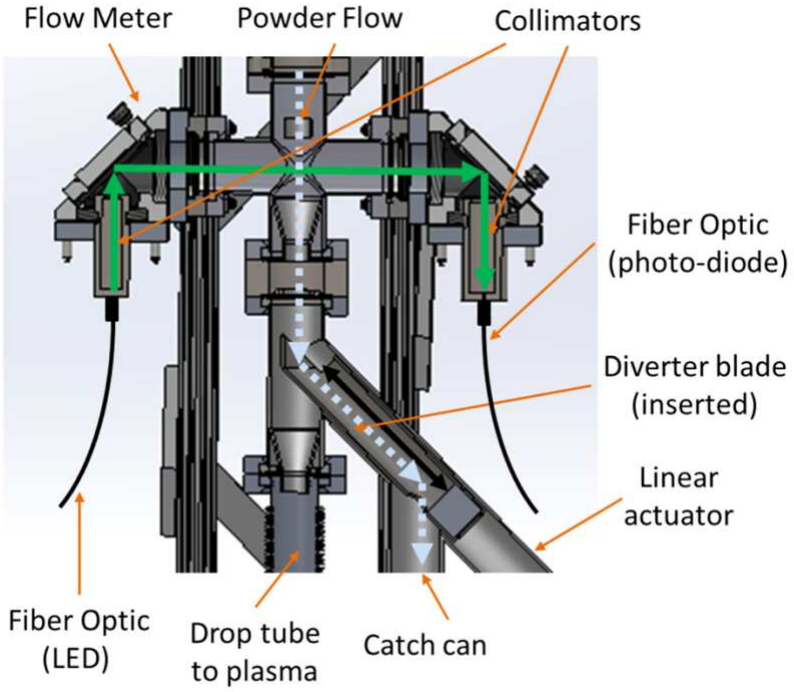

Figure 1.6. Vertical cross-section of IPD showing the vertical powder feeding tube equipped with the diverter shutter and an optical flowmeter. From [26]

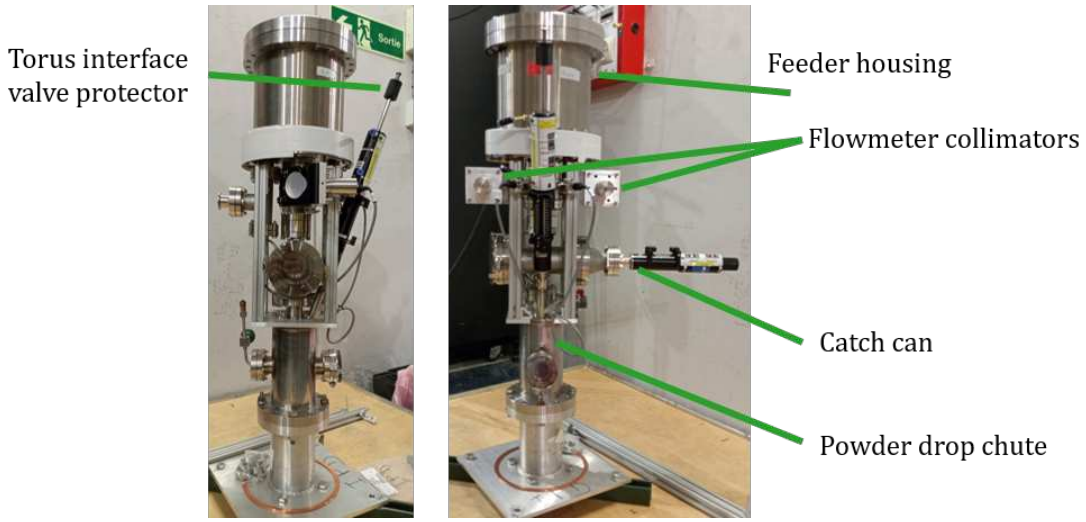

Figure 1.7. Photos of WEST IPD with main components shown. The geometry of WEST IPD slightly varies from the one from [26], but the principle is the same

1.9 Computational modeling of IPD experiments

Computational models of boundary plasma are often utilized to help in the analysis of the experimental data and to have a better insight into the physics of a plasma pulse. There are lots of uncertainties involved in modeling tokamak plasma, e.g. *transport*

coefficients (i.e. diffusivity and viscosity of ions, energy diffusivity) are *anomalous*, i.e. they cannot be or have not been yet calculated from first principles because they represent turbulent transport, and have to be either estimated empirically, or be set by a control algorithm that fits an observable plasma parameter such as an electron density profile with a value provided from an experiment. Nevertheless, the boundary simulation codes are useful when a crude analytic model would not suffice, and a more refined analytic model would be impractical to solve.

One of the advantages of computational models is the access to the plasma parameters that are not directly observable in the experiments. For example, we cannot directly measure the influx of B on the PFCs that we want to condition when we inject B powder, nor can we directly measure the volumetric flux distribution of B and O during the injection. At best the experiments can provide spectroscopic data of B-II and O-II line radiances and the n_e and T_e measurements from one of the PFCs, which in the end would provide us with a gross erosion flux at that PFC, but not anywhere else. Deposition flux can be estimated with the use of collector samples, but these provide measurements cumulative in time, and not instantaneous measurements that are desired in IPD experiments. Near the PFCs without the local n_e and T_e measurements one would have to resort to analysing the evolution of the line radiation in time, hoping that it is a good enough proxy for impurity ion concentration. At the same time in a numerical model these values are directly available, and the experimental measurements can be "modeled" using *synthetic diagnostics*: algorithms that take plasma parameters produced by a plasma simulation code and produce a diagnostic device measurement that corresponds to the given plasma parameters. The measurements of the synthetic diagnostic and of the real diagnostic from an experiment can then be compared to check the soundness of the computational model: if the real and synthetic diagnostic measurements significantly diverge, then at least one of the assumptions made about the modelled plasma has to be incorrect.

Previous attempts have been made to simulate the transport of impurities introduced via powder injection in fusion devices. Shoji et al. [51] modeled pure D boundary plasma in Large Helical Device (LHD) with the EMC3-EIRENE code suite [52], and then used the data from the modeling results as an input for the DUST Transport (DUSTT) code [53]. The EMC3-EIRENE code suite provided spatial distribution of $(n, T)_D$, T_e and plasma flow velocity for DUSTT, which was responsible for modeling B spherical particle transport and ablation, providing the evaporation rate of B. In this study Shoji et al. computed several models of the plasma in the LHD device with varying n_e and found that the lower density plasma scenario was more favorable to the homogeneous distribution of the B flux density due to a stronger deflection of the B particles in a high-density scenario, which prevented them to reach the area of the SOL near the separatrix, where particle transport is more homogeneous in LHD.

A different approach was used by Effenberg et al. [27]: EMC3-EIRENE was used exclusively, with a point source of neutral B placed in the upper part of the boundary plasma, corresponding to the location of the IPD installed on the DIII-D tokamak. That study highlighted an inboard-outboard asymmetry of B distribution: most of the B flux went to the part of the vessel closer to the central column of the tokamak,

i.e. *inboard*, or *high-field side* (HFS). That asymmetry was preserved if B was injected from the top of the machine. Also, similarly to Shoji et al., lower density plasmas were found to be more favorable for an even distribution of B flux on the divertor targets.

In both studies the plasma was considered to have no impurities other than B, and EMC3 treated impurities under the trace approximation, i.e. while impurity radiative losses were taken into account when calculating plasma temperature, they did not contribute to charge balance. The effect of impurities on the main plasma was therefore not completely self-consistent, since we expect that the effect of injected B on the main ions will be significant at high impurity concentration.

1.10 Goals of the study

We set the following goals for this study:

1. Expand the operational domain of the IPD on WEST by maximizing B drop rate and cumulated mass in WEST to try to approach amounts of injected B similar to GDB;

2. Study the effects of IPD conditioning and compare the effectiveness of IPD and GDB in PFC conditioning, as well as study the applicability of IPD in achieving more performant plasma scenarios;

3. Study the conditioning of the new actively cooled divertor;

4. Analyze B powder transport in WEST plasmas in an attempt to improve on the existing computational models to have a better understanding of B distribution on the PFCs and how it depends on the plasma parameters;

5. Use the numerical model to estimate what plasma parameters could help to achieve a more uniform B coating;

6. Perform numerical scans of the plasma parameters to get a better insight into the effects of B powder injection on the plasma in WEST.

The results of the experimental part of the research are described in chapter 2. The results of the numerical analysis of the IPD experiments is presented in the chapter 3. The discussion of the results is given in chapter 4. Chapter 5 is devoted to the discussion of the future research in this domain.

2 Experiment description and results

In this chapter, we will describe the experimental setup of the WEST tokamak and its IPD for the dedicated experiments in section 1 and present the results of the experiments in section 2.

2.1 Methodology of B powder injection experiments

2.1.1 WEST experimental setup

The Low Field Side (LFS) part of the WEST wall, i.e. the side of the wall farther from the central solenoid, is equipped with diagnostic ports, heating antennas, and an Antenna Protection Limiter (APL) (figure 2.1). Two types of microwave heating are supported in WEST, Lower-Hybrid Current Drive (LHCD) [54] and Ion-Cyclotron Resonance Heating (ICRH) [55]. In the IPD experiments, LH heating was preferred to ICRH because of the lower amount of total radiation losses P_{rad}^{total} of the plasma relative to the total heating power $P_{heating}$, i.e. lower *radiative fraction* $f_{rad} = P_{rad}/P_{heating}$, which in the case of ICRH heating was higher due to plasma pollution with copper from ICRH antennae. Attempts to inject B powder during ICRH-heated pulses led to MHD instabilities, followed by a disruption.

IPD injections were performed during WEST L-mode plasma pulses with diverted magnetic configuration, with the X-point located in the lower part of the machine, i.e. in *lower single null (LSN)* configuration. A typical pulse with a B powder injection consisted of several phases, illustrated in figure 2.2. After a gas prefill and plasma breakdown (gas ionization to create plasma) the plasma current I_p, n_e, and $P_{heating}$ would reach their quasi-static values during the *ramp-up* phase. Past ramp-up, the plasma pulse would continue for around 10 seconds in the pre-drop phase, which served as a reference point for the subsequent drop phase, which would last for 10-20 s. Soon after the end of the injection, if a disruption did not occur, the plasma pulse would undergo a *ramp-down* of I_p, $P_{heating}$ and n_e, gracefully ending the pulse.

The most important WEST diagnostics for the IPD experiments were those responsible for measuring $(n,T)_e$ in the confined region, in the boundary plasma, and at the divertors, as well as diagnostics used for estimating the impurity content in these regions. For n_e in the outer midplane, i.e. in the LFS equatorial region of the plasma, a *fast-sweep reflectometry* diagnostic was used [56]. $(n,T)_e$ at the inner and outer targets were measured by *embedded Langmuir probes*. Langmuir probes function

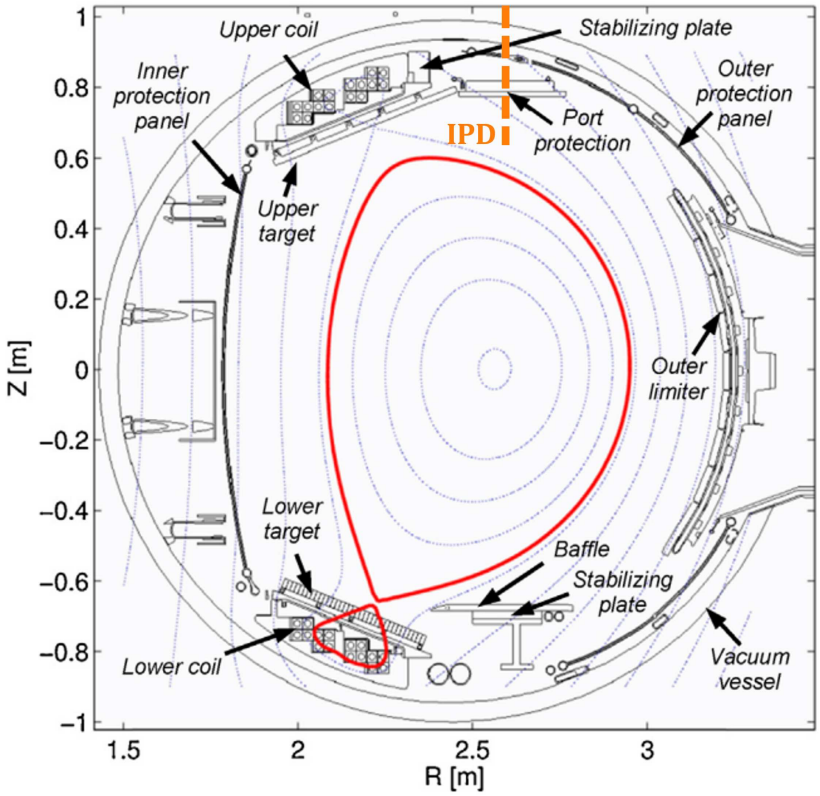

Figure 2.1. Cross section of WEST vacuum vessel from [11]. “Outer limiter" denotes the position of either a heating antenna or APL. IPD position is denoted with orange dashed line.

by measuring the current-voltage characteristic of the probe by varying the probe's potential with respect to the potential of the vessel. $(n,T)_e^{sheath}$ are calculated from the measurements of ion and electron saturation currents using the equations of the electrostatic sheath, as described in section 9.2 in [1].

Fluxes of the main ion and the impurities at the PFCs were estimated using *visible spectroscopy* [57]. Both divertors and midplane limiters on both sides were monitored by visible spectroscopy lines of sight (LoS). *UV spectroscopy* was used to estimate W concentration in confined plasma [58]. The neutron flux rate, which serves as an indication of energy confinement quality, was measured by ionization chambers [59].

Radiated power P_{rad} is measured with *bolometry* diagnostic [60]. Out of 16 lines of sight of P_{rad} detectors three are pointing to the lower and upper divertors each, and 10 lines of sight measure P_{rad} closer to the equatorial plane (figure 2.3), allowing to distinguish P_{rad}^{bulk} (i.e. from the confined plasma and midplane boundary plasma) and P_{rad}^{edge} (i.e. from the plasma at the divertors).

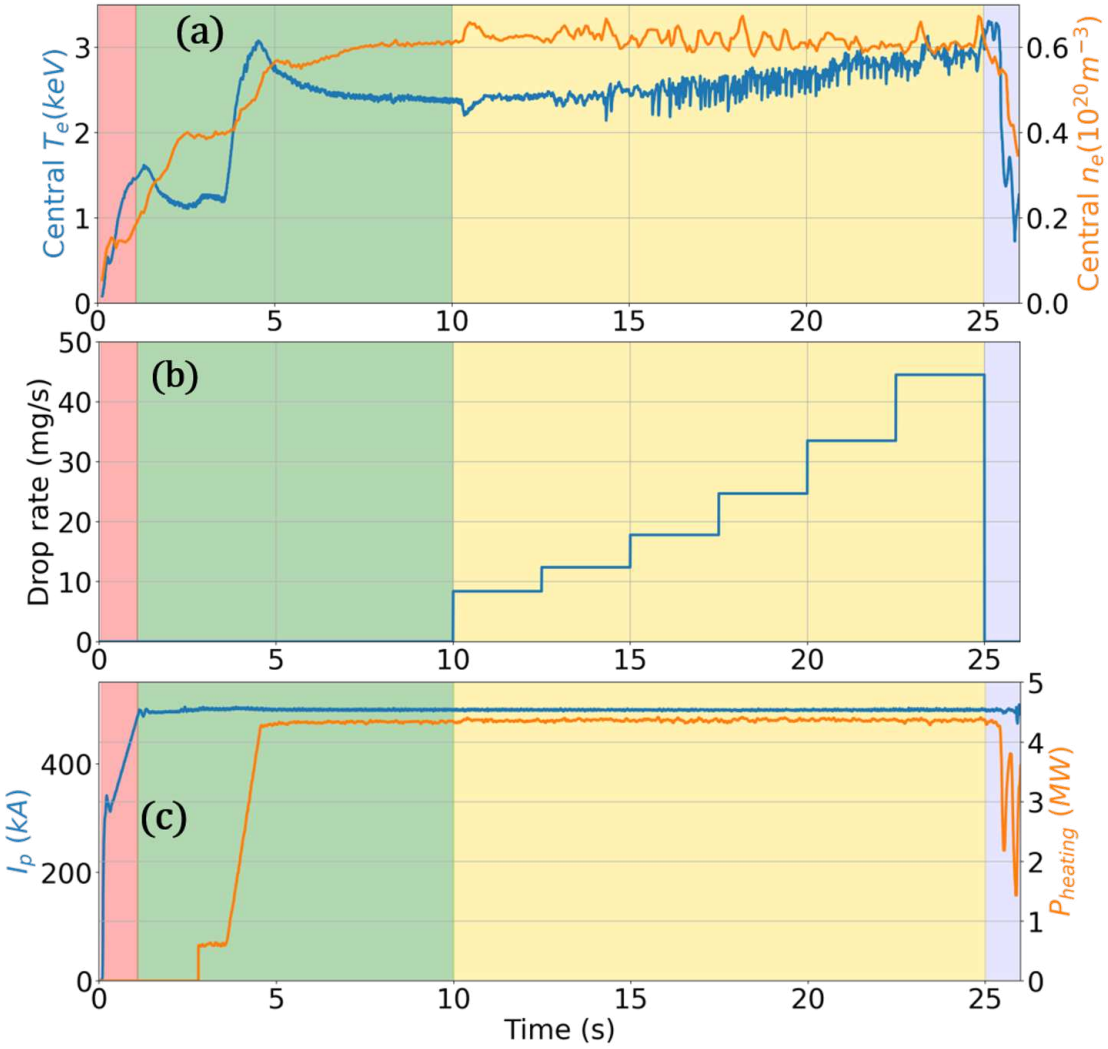

Figure 2.2. Time traces of the programmed drop rate (a), $n_e^{central}$ and temperature (b,c), plasma current, and total stored energy (d,e) in pulse 58051 in the 2023 experiment. In the background colors are shown: current ramp-up (red), X-point formation, LH heating ramp-up and attainment of the pre-drop phase plateau (green), drop phase (yellow), LH ramp-down, and the end of the pulse (purple).

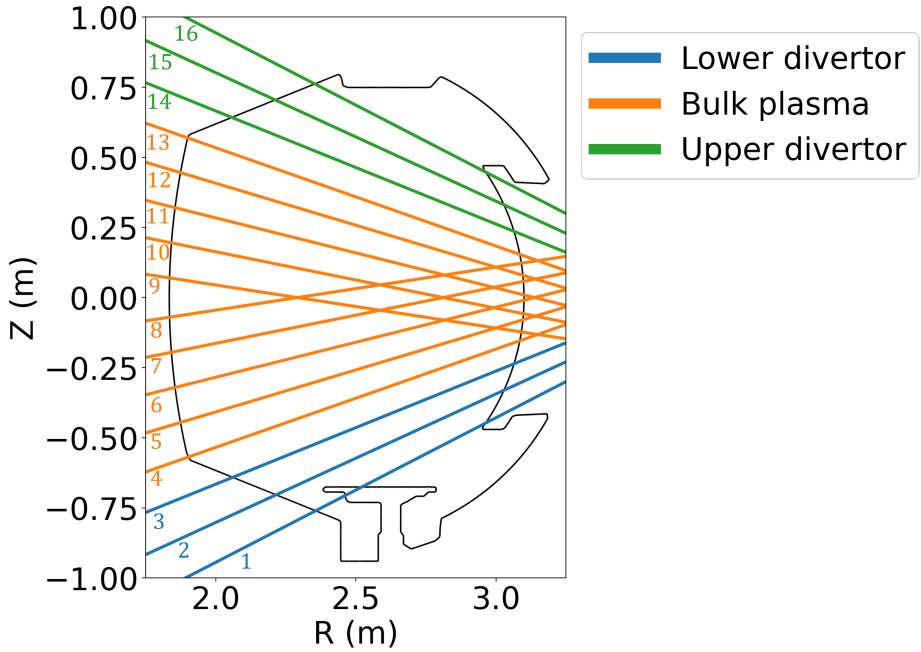

Figure 2.3. Bolometry lines of sight, from bottom to top: 1-3 — lower divertor, 4-13 — bulk plasma, 14-16 — upper divertor

2.1.2 IPD experimental setup

Similar to other plasma devices, WEST had an IPD installed on top of the machine in sector Q5a at the radial distance ≈ 2.56 m to the center of the tokamak (figure 2.1). The feeders were filled with B and BN powders, allowing one to choose the powder type during an injection pulse. Each feeder was calibrated to find the resonance frequency and to establish a relation between the peak-to-peak voltage V_{pp} of the applied sine wave and the drop rate μ by fitting a power law curve with least squares method (figure 2.4). The dispersion of the drop rate points in figure 2.4 comes from the presence of the feeder cap on the troughs after a vacuum loss incident, affecting the resonance frequency of the system. The calibration was additionally verified after the experiments by comparing the calibration curve with powder injection rate estimates from B-II lines from visible spectroscopy and powder-caused visible radiation from fast cameras [50]. While a flowmeter was installed in the drop tube of the IPD, it could not be reliably used to determine μ during the pulse due to low signal-to-noise ratio and the random walk of the alignment of the LED and photo-diode mirrors caused by the vibrations of the tokamak during the pulses.

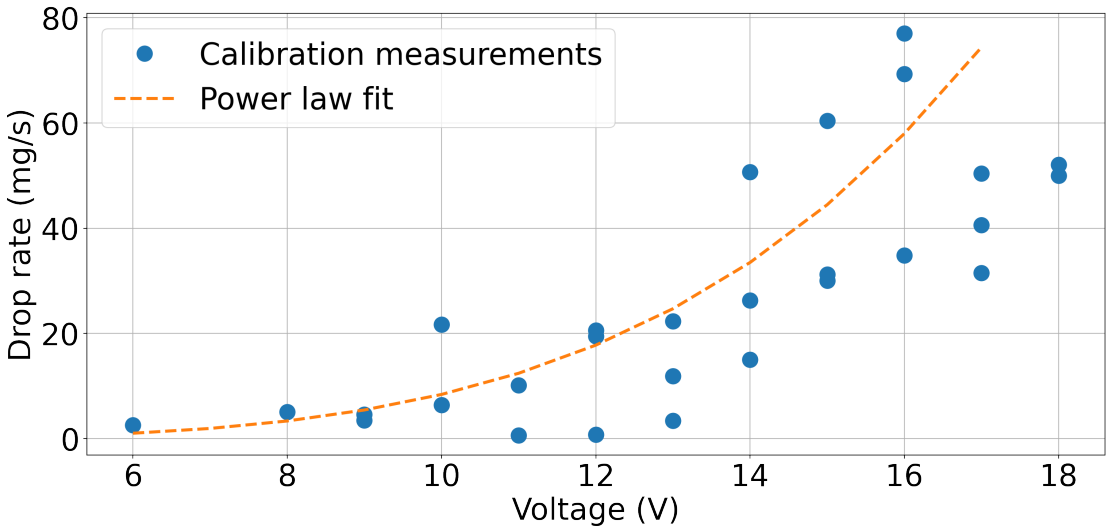

Figure 2.4. Calibration measurements of an IPD feeder with B powder for 2023 experiments

2.2 Objectives for the dedicated experiment

Firstly, the dedicated IPD experiments aimed at expanding the operating space of the IPD on WEST compared to the experiments during the IPD commissioning campaign, described in chapter 1. Secondly, a new fully actively cooled ITER-like W divertor was installed in 2021, and the study of the conditioning of such a divertor was one of the goals of the experiment. Thirdly, an attempt was made to reach a high μ_B and

total injected B mass M_B, with the goal of accumulating M_B comparable with the total amount of B injected in a typical GDB conditioning discharge, which is approximately 10 g, with the goal of comparing the IPD conditioning effect with the effect of GDB. Lastly, the study of the effect of B injection on the transport of W and low-Z impurities in the expanded operating space of the IPD was also a goal of the experiment.

2.3 B and BN powder injection experiment description

Two dedicated series of IPD injection pulses were carried out in the course of this study. In the first, higher drop rate series, approximately 1 g of B was injected over four pulses with B powder injection, with $\mu_{max} \approx 58$ mg/s (table 2.1). Three pulses without powder injection were used for reference. There were five plasma pulses that did not have powder injection due to either early disruptions or their designation as an Ohmic cleaning pulse, which was necessary to restore machine conditions after a disruption. Injections were performed in the LSN configuration, with 4.4 MW of LH heating power and $I_p = 500$kA, with injections starting 10 seconds after the beginning of the current plateau. Both M_B and μ_{max} were around three times greater than in the previous experiment on WEST.

Pulse #	μ, mg/s	Injection duration per μ step, s
58047, 58048, 58049	Reference pulses (no B powder)	0
58050	0.0, 1.0, 3.4, 8.4	2.5
58051	8.4, 12.4, 17.8, 24.7, 33.5, 44.5	2.5
58053	17.8, 12.4	5
58059	17.8, 33.5, 58.0, 17.8	2.5

Table 2.1. IPD drop rates in the higher drop rate series of experiments

In the second, lower drop rate series, which happened about a year after the higher drop rate series, three reference pulses and 14 pulses with powder injection were performed. The plasma conditions were a lot less favourable compared to the higher drop rate series, probably due to the accumulation of impurities over the course of the experimental campaign. Because of that, much smaller drop rates ($\mu_{max} \approx 3$–5 mg/s) were sustained, according to the calibration performed prior to the experiment. To compensate for the smaller operational window with regards to μ, the injections were performed in two other pulse scenarios: in ohmic shots with no additional heating and in the *long pulse* scenario, i.e. with 3 MW of LH heating, $I_p = 400$kA and with the pulse duration over 60 s. In addition, BN powder injection was also performed to compare its effect on the plasma with the effect of B, as BN appeared to have a stronger effect on core energy confinement in ASDEX-Upgrade [43]. Input power and programmed IPD voltages are given in table 2.2; the voltages are given instead of μ because the calibration performed before this experiment series could not resolve

μ variation due to low powder injection rates: during the experiments the visible cameras and the spectroscopy diagnostics detected powder injection, while during the calibration almost no powder was dropped at these voltages. The discrepancy between the calibration and the actual voltage-μ dependency during the second series can be attributed to the vacuum loss incident similar to the one described above.

Pulse #	Input power, MW	Powder, μ and durations
59208	4	Reference shot
59215	0 (Ohmic)	B, 5 V for 1 s
59216	3	B, 4-4.5 V for 30 s
59218	3	B, 3-4 V for 30 s
59219	3	B, 3.25-3.75 V for 15 s
59220	3	B, 3.5 V for 25 s
59221-59224	4	No powder
59265	3	B, 3.5 V for 35 s
59266	4	0
59268	4	BN, 2-4 V for 6 s
59272	3	BN, 3-3.5 V for 15 s
59277	0 (Ohmic)	B, 3.5 V for 5 s
59278	0 (Ohmic)	B, 3.5 V for 5 s
59280	3	BN, 3.5-4.25 V for 20 s
59284	3	B, 3.25-4 V for 20 s
59288	0 (Ohmic)	B, 3.75 V for 6 s
59289	0 (Ohmic)	B, 3.5 V for 6 s

Table 2.2. IPD drop rates and $P_{heating}$ in the low drop rate series of experiments

2.3.1 Transient effects of B powder injection at high drop rates

Similar to the commissioning experiments in 2021 [49], we observed real-time effects of B injection on wall conditioning via visible spectroscopy at the PFCs (lower and upper divertors, HFS inner bumper, and LFS LH antenna). Time traces of spectral lines from a typical pulse from one of the spectroscopy LoSs at the outer target of the lower divertor are shown in figure 2.5. The traces were normalized by line-integrated density at the lower divertor $\langle n_e l \rangle_{\text{low div}}$ measured by the interferometry diagnostic along the lower divertor LoS (LoS 1 from figure 6 in [61]) to account for the changes in n_e due to the changes in fueling and/or in ion recycling rates caused by B injection. The time trace of the B-II line indicates the increased amount of B at the lower divertor. D and light impurity signals indicate lower recycling rates of the main ion and light impurity species. The W signal indicates increased sputtering of W by the injected B. The peak target electron temperature T_e^{target} for each target was calculated by taking a maximum value of a Langmuir probe measured at every point in time for

inner and outer target regions of the divertor. T_e^{target} was mostly unaffected by the B powder injection, except for a sudden drop near the end of the injection at t=22.5 s in 58051, as shown figure 2.6, suggesting a partial detachment of the inner leg. While GDB is performed to bind O via the gettering effect, the spectroscopic data suggests that during the B powder injection, the light impurities may get trapped in the deposited B layers, which can be important considering that on WEST carbon (C) could still be a significant contributor to W sputtering [18]. Similar to the commissioning experiments, improved confinement was also observed, e.g. central T_e (figure 2.2a), increased W_{MHD}, and neutron flux rate (figure 2.7).

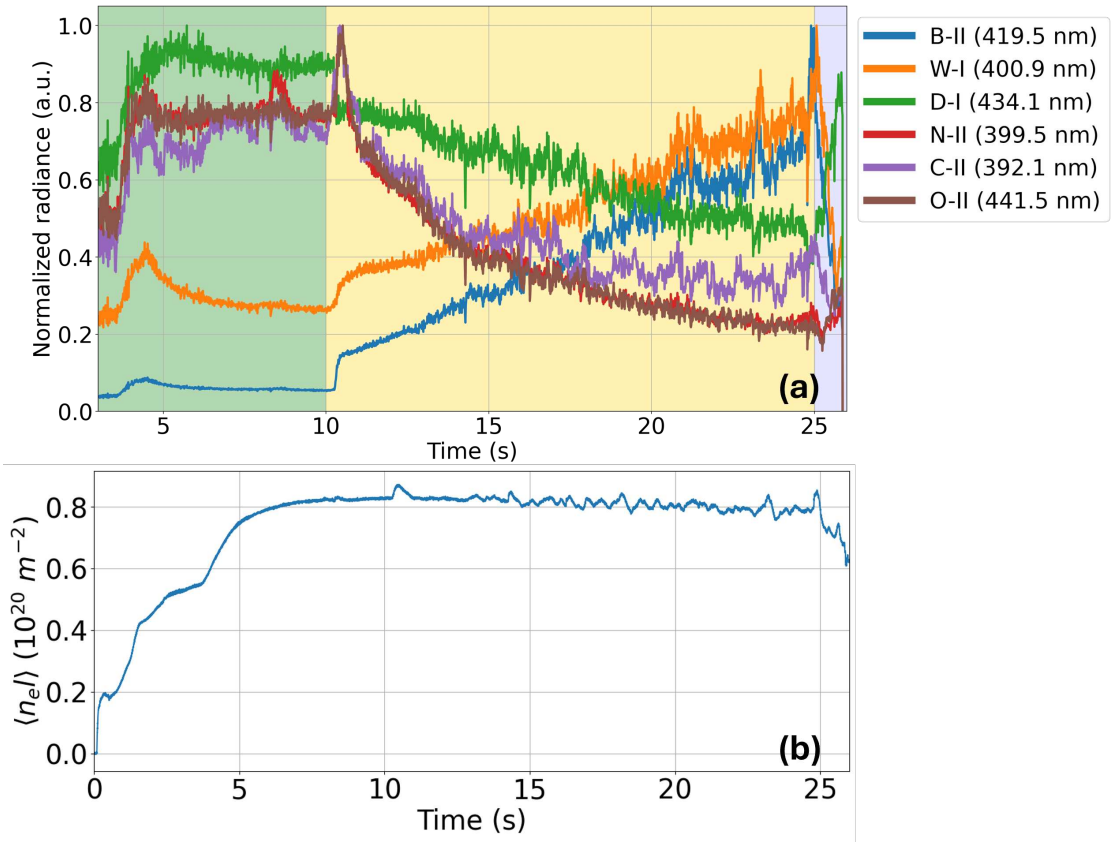

Figure 2.5. **(a)** Visible spectroscopy signals from the lower divertor in pulse 58051, normalized by $\langle n_e l \rangle_{\text{low div}}$ and scaled for readability (1.0 corresponds to the time trace maximum in the presented time window). The background color is the same as in figure 2.2. **(b)** Line-integrated electron density along the lower divertor, used to normalize visible spectroscopy signals in **(a)**

In addition to the density-normalized radiance, the ratio of O fluxes at the lower divertor during and before powder injection $\Gamma_{O+}^{\text{drop}}/\Gamma_{O+}^{\text{predrop}}$ was estimated with *S/XB analysis*: the intensity of an O-II line was multiplied by an ionization-per-photon coefficient, also called S/XB coefficient, where S stands for ionization rate coefficient, X stands for excitation rate coefficient and B stands for branching ratio of the transition. The coefficient was produced with the ColRadPy library [62], which solves

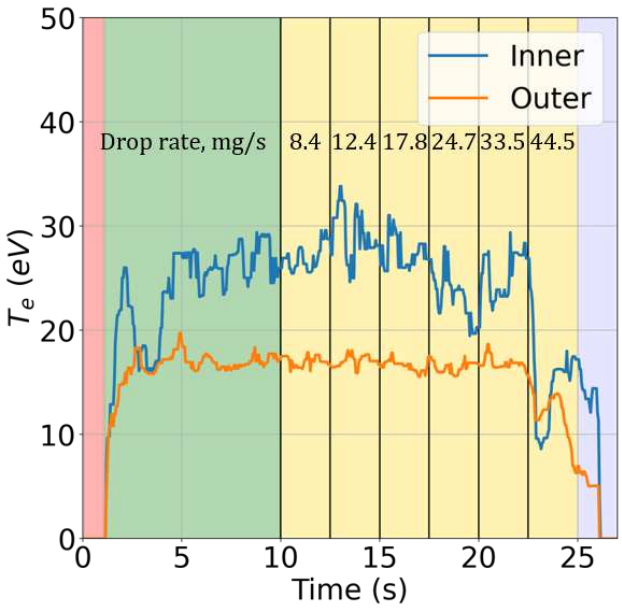

Figure 2.6. Peak T_e^{target} in pulse 58051 measured by embedded Langmuir probes, background color is the same as in figure 2.2. Inner and outer target regions shown in figure 2.13.

the collisional radiative equations for a better approximation of the coefficient. S/XB data produced by that library take the form of a matrix S/XB (n_e, T_e); that matrix was interpolated on the Langmuir probe measurement grid across major radius and time $(R \times t)$. PFC flux measurements with S/XB assume that the radiating ions were sputtered/eroded within the surface of the PFC covered by a spectroscopy LoS, that is, that the perpendicular transport is negligible within the ionization time of a measured species [63]. O-II line intensity measurements from the visible spectroscopy were also interpolated on the same grid, and the results were multiplied to provide a function $\Gamma_{O+}(R,t)$, which was then averaged across different time windows to provide Γ_{O+} profile estimates for the pre-drop and drop phases of a pulse. Profiles of Γ_{O+} in pre-drop and drop phases are shown in figure 2.8, further affirming the reducing effect of B injection on low-Z impurities, which can be explained by the gettering of light impurities during B deposition. The analysis assumes that $(n,T)_e$ variation within O ionization length is negligible; further investigations are needed to verify that assumption.

Further, we observed a roll-over in total radiated power P_{rad}^{total} during B injections past $\mu \approx 20$ mg/s, which was not previously observed in WEST IPD experiments, as shown in figure 2.9. Pulse 58050 was omitted here and in further figures because the drop rate was significantly smaller than in other pulses with B injections, and so the pulse was not as informative as the others. $P_{rad}^{total}(\mu)$ was calculated by taking the average of P_{rad} in the last 0.5 s of a time window with a given μ in order to allow the effects of drop rate ramp-up to dissapear. The $P_{rad}^{total}(\mu)$ roll-over follows the same distribution in both the first and the last pulses of the experiment (58051 and 58059),

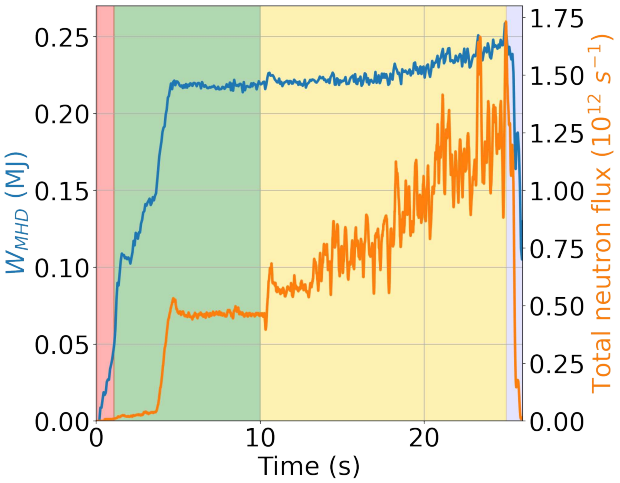

Figure 2.7. W_{MHD} and total neutron flux rate time traces in pulse 58051, background color is same as in figure 2.2.

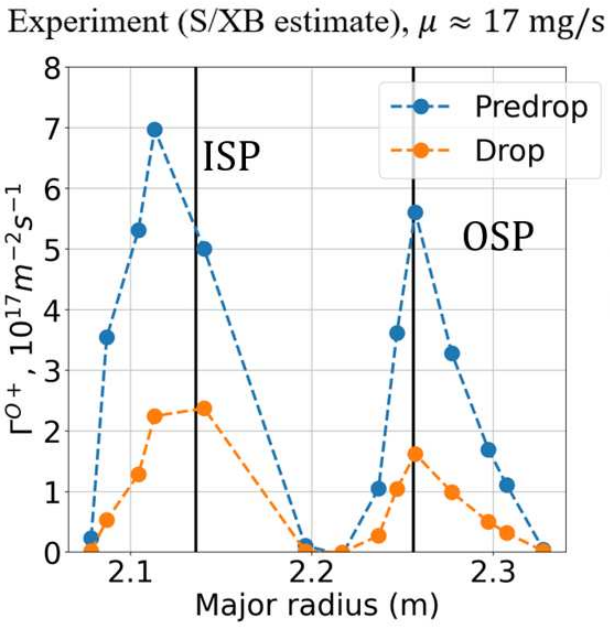

Figure 2.8. $\Gamma_{O+}^{\text{predrop,drop}}$ S/XB estimates in the experiment (pulse 58051, 15 s $< t <$ 17.5 s in the drop phase)

indicating that the roll-over is an effect of B injection on intrinsic impurity transport during the B drop and not a cumulative effect due to e.g. growth of B deposits.

There was no similar roll-over in light impurity spectroscopic measurements, e.g. in figure 2.5 for time traces of N-II, C-II, and O-II lines. In addition, when P_{rad} measurements are broken down between P_{rad}^{bulk} and P_{rad}^{edge}, the roll-over occurs mostly in the confined area of the plasma (figure 2.10). Bolometry signals experience a strong decrease in the upper part of the machine as well, although not at the same time or μ

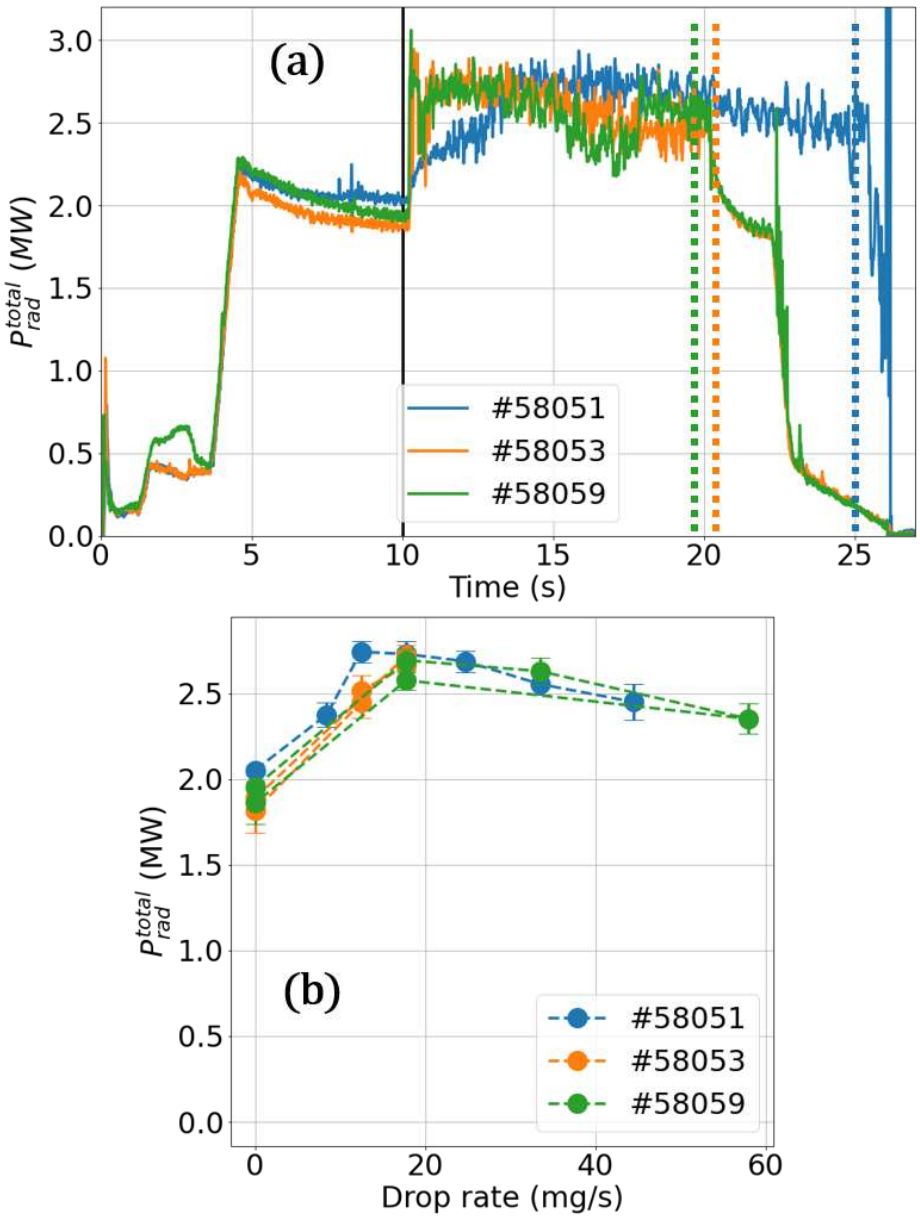

Figure 2.9. Total radiated power from pulses of the high drop rate series as time traces (a) and as functions of μ (b). The full black line shows the start of B powder injection, and dashed colored lines show the end of B injection for each pulse. Note that the drop rate does not monotonically increase with time in pulses 58053 and 58059, per table 2.1

as the P_{rad}^{total} roll-over, which may be caused by the effect of B injection on the plasma transport near the injection site. Thus the roll-over can be attributed to the effect of B injection on W, either by reducing the sputtering rate or by affecting W transport in the boundary plasma, since high-Z impurities are the main source of radiation in confined plasma due to partial ionization of the ions.

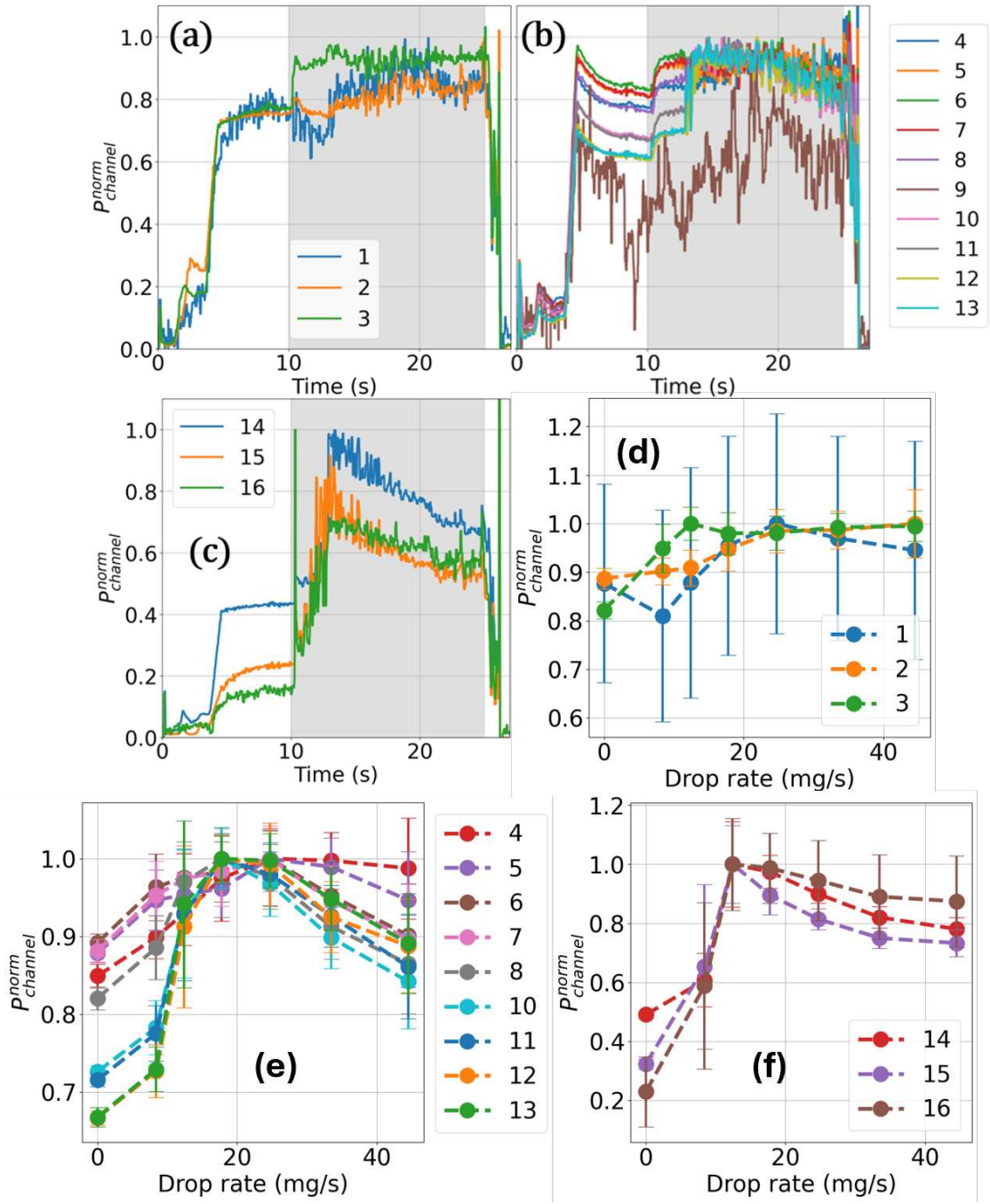

Figure 2.10. **(a-c)** Bolometry measurements from pulse 58051 from the lower divertor region of edge plasma (a), bulk plasma (b), and the upper divertor region of edge plasma (c) normalized by the maximum of the measurement during the drop phase (gray background) and filtered with a median filter. **(d-f)** Same, but as a function of μ_B instead. Channel 8 is omitted due to excessive noise.

To check that W concentration reduction might be the cause of the roll-over, the W core density n_W was estimated from VUV spectroscopy and bolometry measurements

[58], with the estimate shown in figure 2.11. The fact that n_W decreases past a certain μ_B threshold similar to P_{rad}^{total} while the W-I line is consistently increasing with μ_B (except for the inner target at the lower divertor in 58051, which is attributed to the partial detachment) indicates that n_W is lowered by affecting the transport in the boundary plasma via impurity injection, even though the W sputtering rate appears to be monotonically increasing. Speculatively, this effect may be attributed to the same mechanism as in N seeding experiments on WEST: stabilizing ion thermal gradient modes, leading to suppression of W transport into the confined plasma [64]. This result is also consistent with W erosion studies on WEST [65], where it was found that the increase in n_e leads to the decrease of W contamination contribution by the lower divertor due to enhanced screening, despite increased W erosion (figure 6 in [65]). On the other hand, W contribution by the outer midplane limiter increases due to its weak screening, placing an upper limit on B injection effectiveness in reducing n_W.

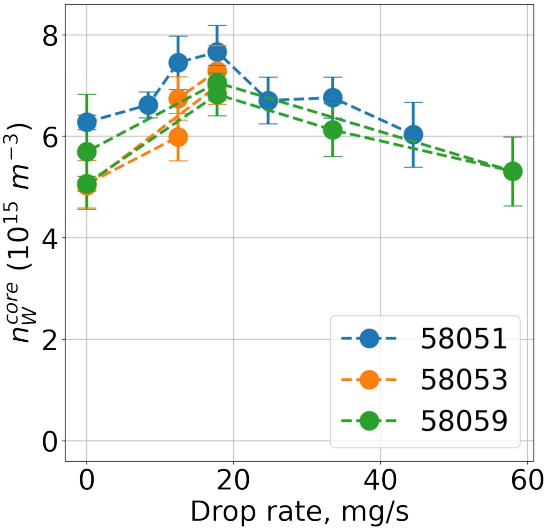

Figure 2.11. n_W in core plasma as a function of μ in pulses with B powder injection

When searching for other possible explanations for the n_W and P_{rad}^{total} roll-overs we found that, while for most PFCs the W-I radiance correlates positively with the injection rate, the dependency of W-I radiance on μ_B for the inner target of the lower divertor was not linear. The radiance of the W-I line from the inner target as a function of μ_B , normalized by the line-average density at the lower divertor is given in figure 2.12, with the radiance from the outer target given as a reference for the dependence of W-I radiance on μ_B for other PFCs. This roll-over was speculatively attributed to the partial detachment of the inner leg of the plasma: while in most pulses Langmuir probe measurements of T_e did not noticeably vary, in 58051 a drop of T_e was observed at the inner leg past t=22.5 s, which corresponded to $\mu \approx 44.5$ mg/s (figure 2.13). The same drop in T_e was not, however, observed in 58059. The roll-over of W-I spectral line radiance was happening at a larger μ threshold than n_W and P_{rad}^{total} roll-overs, and for this reason, potential lower sputtering rate of W due to partial detachment was ruled out as the reason for the n_W and P_{rad}^{total} roll-overs.

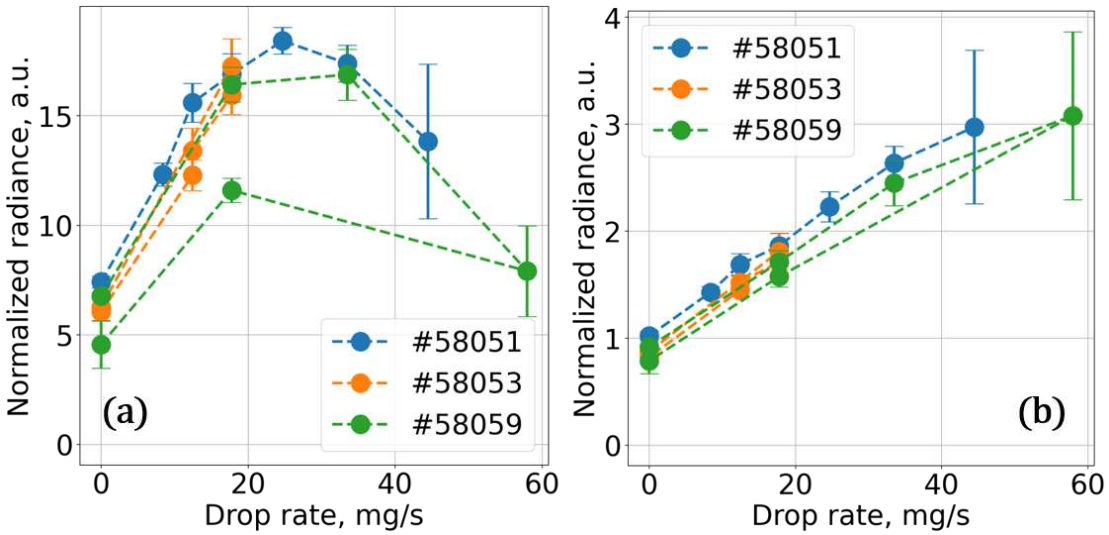

Figure 2.12. W-I (400.9 nm) radiance at the inner (a) and outer (b) targets of the lower divertor, normalized to line-integrated n_e at the lower divertor as a function of μ_B. Measurements are taken from spectroscopy LoSs closest to the strike points at the lower divertor.

While T_e^{target} measured by the Langmuir probes did not vary a lot during the pulses with B powder injection, the injected impurities did have an effect on the temperatures of the PFCs, which was observed via fast infrared camera measurements (IR). The evolution of the peak apparent temperature at the outer target of the lower divertor $T_{\text{app}}^{\text{outer}}$ against time and μ_B are given in figure 2.14. The saturation of $T_{\text{app}}^{\text{outer}}$ at $\mu \approx$ 15 mg/s is consistent with the saturation of the peak n_e at the outer target of the lower divertor at $\mu \approx 20$ mg/s (figure 2.15), which in turn is consistent with the spectroscopic data for low-Z impurities, e.g. O (figure 2.16), affirming the effect of B injection on the recycling rates. This is because the heat flux to the PFC is proportional both to the particle flux to the PFC and the temperature of the incident particles.

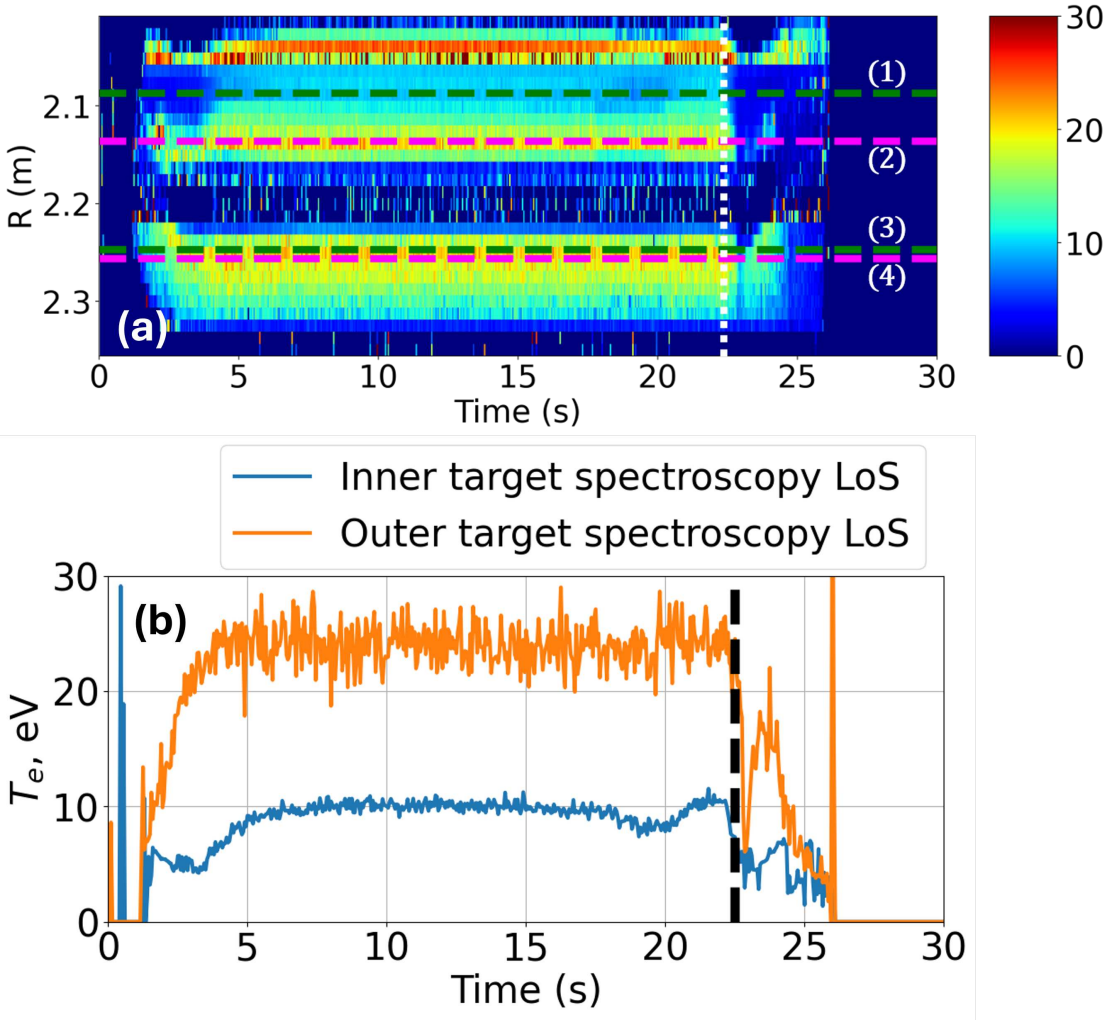

Figure 2.13. **(a)** T_e measurements at the lower divertor in 58051 with embedded Langmuir probes, with inner (2) and outer (4) strike points in magenta and spectroscopy LoS positions at the inner (1) and outer (3) targets in green. The vertical white line marks t = 22.5 s when partial detachment appears to occur. (1) and (3) also denote the radial position of the spectroscopy LoSs used in figures 2.12(a) and (b). **(b)** Same, but as time traces at the spectroscopy LoS positions at the inner and outer targets.

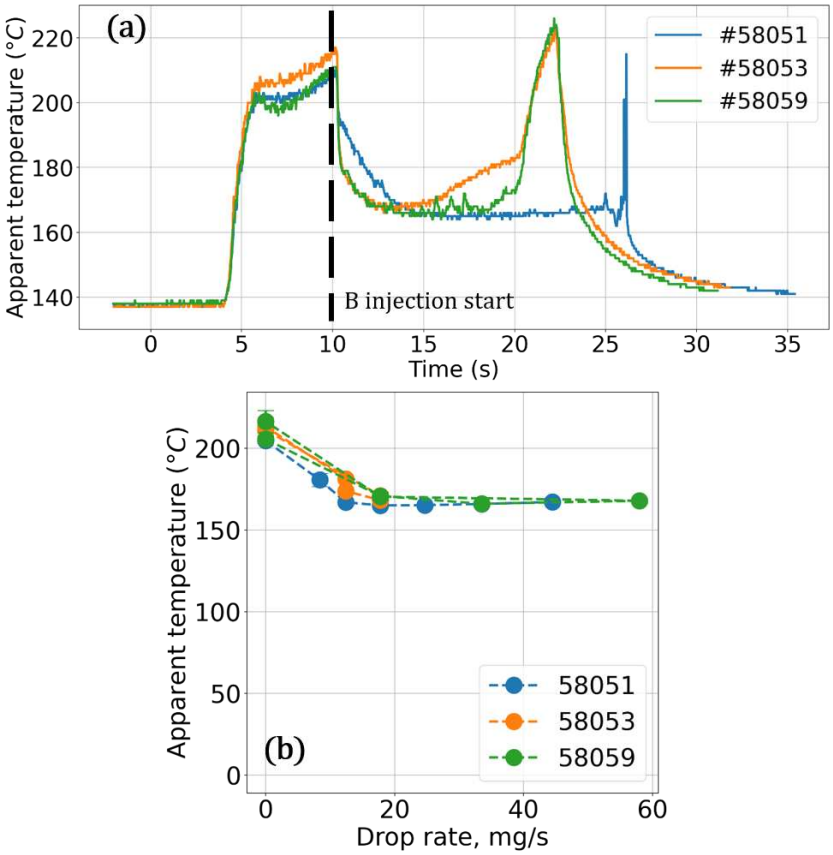

Figure 2.14. $T_{\text{app}}^{\text{outer}}$ measurements from infrared cameras as a function of time (a), and as a function of μ_B (b). Note that the injection time in pulses 58053 and 58059 is 10 s as opposed to 15 s in 58051 and that $\mu(t)$ is not monotonic in 58053 and 58059 per table 2.1

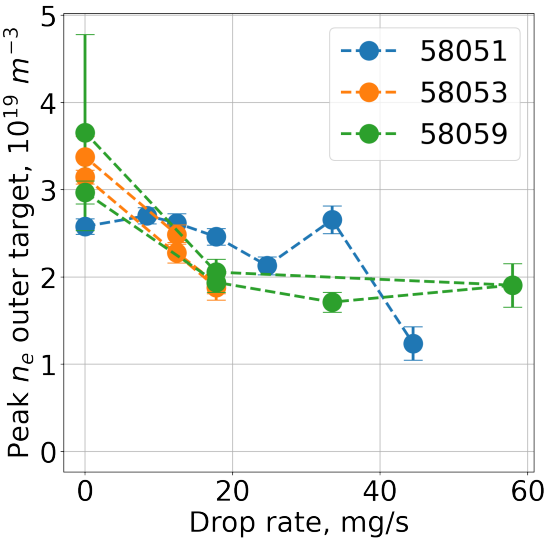

Figure 2.15. Peak n_e at the outer target of the lower divertor as a function of μ_B

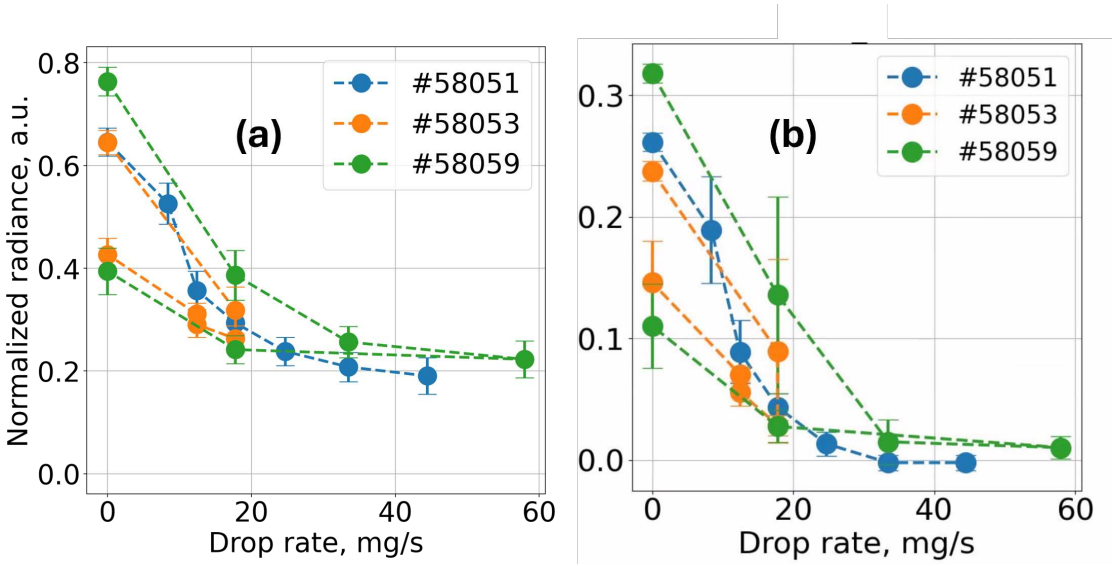

Figure 2.16. O-II (441.5 nm) density-normalized radiance at the (a) outer target and (b) inner target of the lower divertor as a function of μ_B

2.3.2 Cumulative effects of B powder injection

The conditioning effects of B powder injection were evaluated by analyzing cumulative changes in the experimental data from pulse to pulse. One of the quantities whose evolution with respect to M_B was studied was the visible spectroscopy signal in the pre-drop phase. The change in radiance of B-II, W-I, and O-II lines with the increase of M_B in higher drop rate series is shown in figure 2.17 for the inner bumper PFC, which is of particular interest since we assumed it to receive the least amount of B influx due to the LSN configuration and it being farther from the plasma than the antenna. The increase of B-II line radiance and decrease of O-II line radiance suggests the formation of B deposits on this PFC which appears to getter O at a higher rate, likely due to its higher reactivity with O and the porous nature of the B deposits which increased the surface area of the conditioned PFCs, allowing for a more effective O capture via oxide formation compared to bare W surface. While there is no data on the porosity of the B deposits particular to the IPD experiments, the post-mortem studies of the lower divertor's deposit area at the inner target suggest that the B deposits have higher porosity compared to W deposits [66], although the main source of these deposits is GDB conditioning, not IPD experiments. The decrease of W-I radiance further suggests W sputtering rate reduction in the pre-drop phase due to the reduction of O source. This dynamic of pre-drop-averaged line brightness and M_B was present on all PFCs. These B deposit growth indications showed opposite dynamics when a disruption occurred (black arrow in figure 2.17, disruption occured in 58054, after the cumulative measurements were taken), showing that the B deposits can be damaged by a disrupting plasma, reversing the conditioning effect. A conditioning effect with the same dynamic with regards to disruption was also observed in the cumulative effect of the $f_{rad} = P_{rad}/P_{heating}$, shown in the same figure.

Similar effects on the wall conditions, although milder, were observed in the lower drop rate series of pulses as well (figure 2.18). Like in the higher drop rate series, the conditioning effect deteriorated when disruptions occurred. The decrease of B-II line brightness between the experiment days was likely caused by the experimental pulses not related to our experiment, performed after the day 1 IPD pulses.

Conditioning by B powder injection in higher drop rate series was compared with GDB conditioning, which was studied in a recent dedicated experiment. In the experiment, a series of pulses in identical scenarios with 4 MW of LH heating were performed before and after a GDB conditioning session, where approximately 10 g of B were injected in the form of B_2D_6 gas [67]. Average f_{rad} and O-II line radiance $I_{\text{O-II}}$ at the LH antenna in each pulse with available data are given in figure 2.19, where the effect of GDB can be observed in the form of a decrease of f_{rad} and $I_{\text{O-II}}$ measurements, as in IPD experiments. Visible spectroscopy measurements from the LH antenna were chosen for the analysis because the LH antenna was the only PFC with reliable visible spectroscopy lines of sight in the GDB experiment.

The reduction of f_{rad} after the GDB was similar to the reduction of f_{rad} after a day of IPD injections ($M_B \approx 530$ mg). In the subsequent series of 4 MW pulses after GDB (~6 minutes total) f_{rad} increased by at least half of the difference of f_{rad} before and

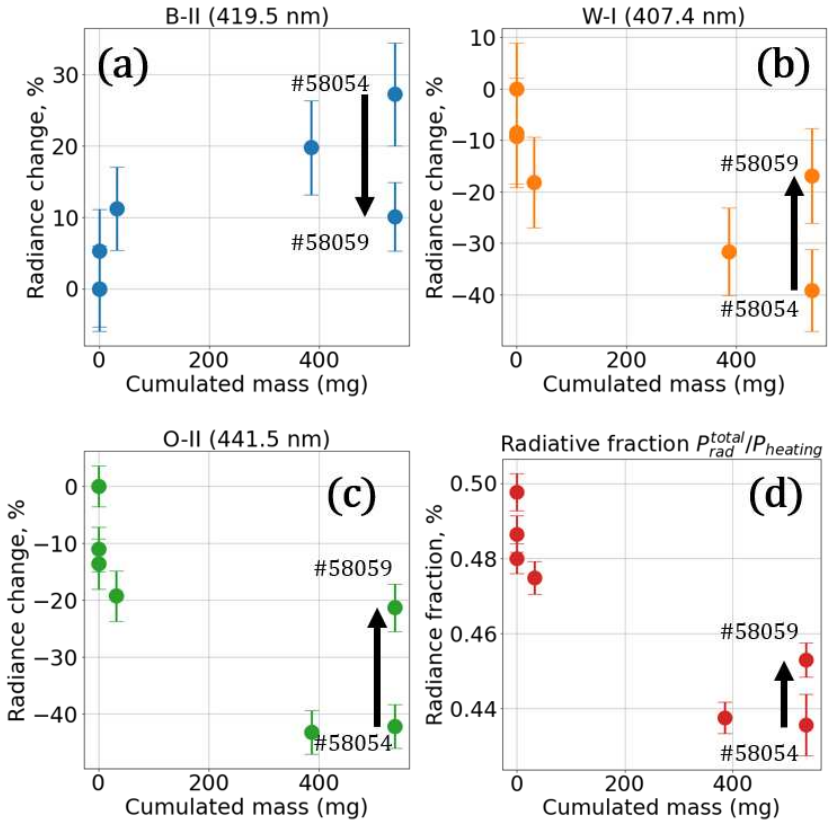

Figure 2.17. Radiance change of B (a), W (b), and O (c) at the inner bumper and f_{rad} (d) in the pre-drop phase of high drop rate pulses. The black arrow represents an opposite trend for when a disruption occurs between the pre-drop phases of the presented pulses

after the GDB. The reduction of $I_{\text{O-II}}$ in GDB experiments was stronger than in the IPD experiment (figure 2.20) and the rate of the fading of the conditioning effect on $I_{\text{O-II}}$ post-GDB session remains unclear. Nevertheless, B powder injection appeared to have comparable effectiveness in changing the plasma parameters linked to the wall conditions' quality with a much smaller amount of B injected and at a shorter time scale: $\approx$ 530 mg in IPD experiments during $\sim$ 1 minute of total B powder injection time against $\sim$ 10 g of B injected in GDB during multiple hours.

Another favorable feature of IPD boronization when compared to GDB is the fact that it can be performed quickly and on demand. This feature was relevant during the low drop rate series of experiments where the machine state was unfavorable for the experiments: disruptions often occurred due to radiative spikes caused by W dust appearing in the plasma [68]. Four pulses 59209-59212 disrupted during ramp-up, after which three ohmic pulses were performed to clean the PFCs. The last ohmic pulse from the cleaning series 59215 featured a one-second-long B powder injection at 5 V, which corresponded to $\mu \approx 3$ mg/s. The following pulse 59216 featured 3 MW of heating power and had two B powder injections, one with 4 V of IPD voltage for 10

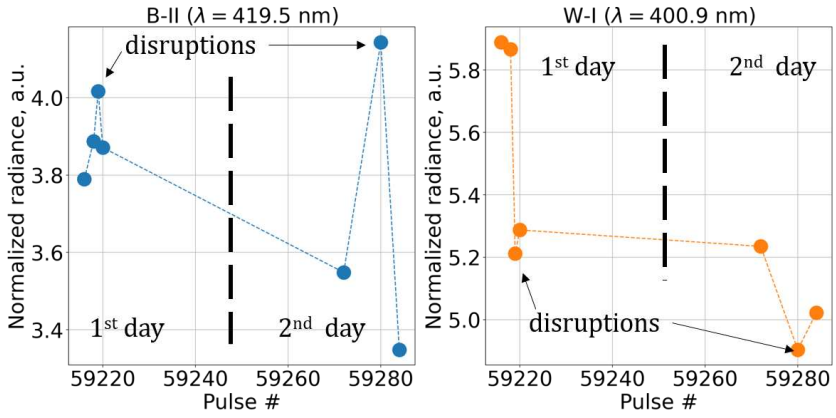

Figure 2.18. Density-normalized radiance of B and W at the lower divertor in the pre-drop phase of low drop rate pulses.

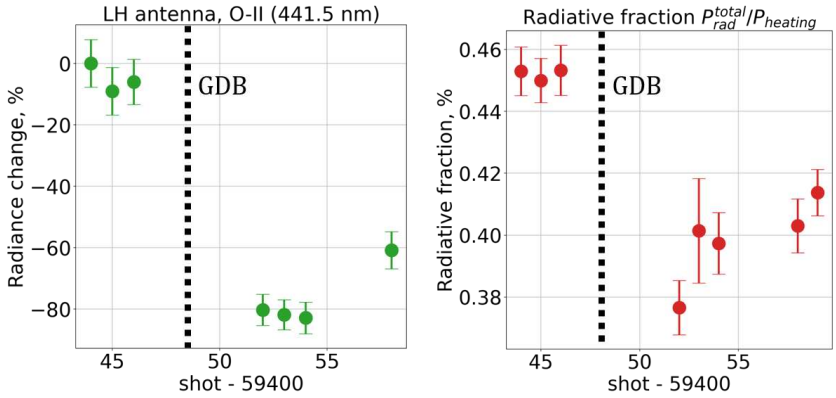

Figure 2.19. Change in O-II radiance at the LH antenna and f_{rad} in GDB experiments

seconds, which the plasma handled, and another at 4.5 V, which was tolerated by the plasma for three seconds and then caused a disruption.

With the 3 MW pulses being tolerated by the plasma, a series of three more long pulses were performed with B powder injections (59218-59220) in order to build up a conditioning layer of B deposits on the PFCs. After that, a series of 4 MW pulses (59221-59224) were performed with no B powder injections to verify the improvement of the tokamak wall conditions. The pulses from this series were successful, with no disruptions except for the very end of the last pulse during ramp-down. A similar effect was also observed on the second day of the low drop rate series of IPD experiments when a 4 MW pulse 59266 was facilitated by a 3 MW long pulse with 35 s of B powder injection at 3.5 V. Considering that the attempts to perform 4 MW pulses in that experiment before B powder injections almost always ended in disruption during ramp-up (59209-59212 in the first day, 59262-59264 in the second day), these incidents show obvious improvement of tokamak conditions with B powder injections even at the low drop rate.

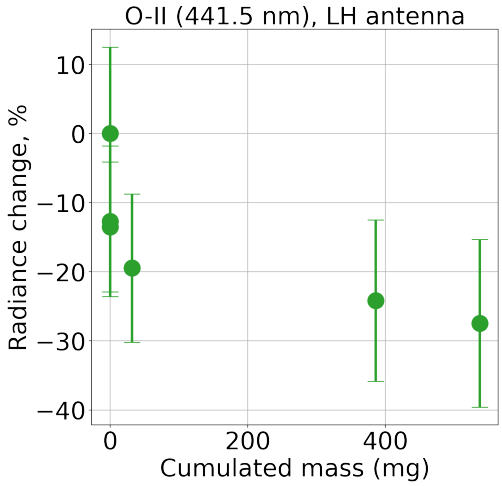

Figure 2.20. Change in O-II radiance at the LH antenna in IPD experiments

2.4 BN powder injection experiment results

In the low drop rate series of the IPD experiments BN powder was injected for the first time in WEST plasma. The motivation behind the BN powder injection was to test whether BN affects the boundary plasma transport of impurities more strongly than the regular B powder due to higher emissivity of N when compared to B; for example, BN injection appeared to have an effect on f_{rad} in ASDEX-Upgrade similar to that of N seeding [43]. N seeding is also studied on WEST as a method to reduce heat flux to PFCs in W machines by increasing P_{rad} in the boundary plasma [69].

While calibration was not available in the low drop rate series of the experiments, the pulses with B and BN powder injections could still be compared using S/XB estimates of ion fluxes. Two pairs of pulses with B and BN powder injections were compared: one pair with 4 MW of LH heating and pulse duration of ~20 s, and one pair with 3 MW of LH heating and pulse duration of ~60 s.

In both pairs of pulses, the estimated B influx increase at the lower divertor due to powder injection was significantly lower in BN injection pulses than in pulses with B injection (figure 2.21). Considering that the reduction of O-II line radiance and S/XB-estimated fluxes were previously attributed to the reduction of light impurity recycling by B deposits, we compared the effect of BN powder injection on O^+ flux $\Gamma^{S/XB}_{O^+}$ with that of B powder (figure 2.22). In 4 MW pulses the amount of powder injected in the BN pulse was a lot smaller than in the B powder pulse, as suggested by S/XB estimates and visible camera footage. In the BN pulse, μ_{BN} was only high enough at $V_{pp} = 4$ V to affect $\Gamma^{S/XB}_{O^+}$. At the same time, the effect of BN powder injection on $\Gamma^{S/XB}_{O^+}$ when μ_{BN} was high enough to affect it was comparable with the effect of B powder injection: both reduced $\Gamma^{S/XB}_{O^+}$ by $\sim 2 \times 10^{17} m^{-2}\ s^{-1}$. Similarly, in 3 MW pulses BN powder injection caused a reduction of $\Gamma^{S/XB}_{O^+}$ by $\sim 1 \times 10^{17} m^{-2}\ s^{-1}$, even though the amount of B injected in pulse 59280 with BN powder was approximately three times lower than in 59220 with B powder, judging by $\Gamma^{S/XB}_{B^+}$ estimates.

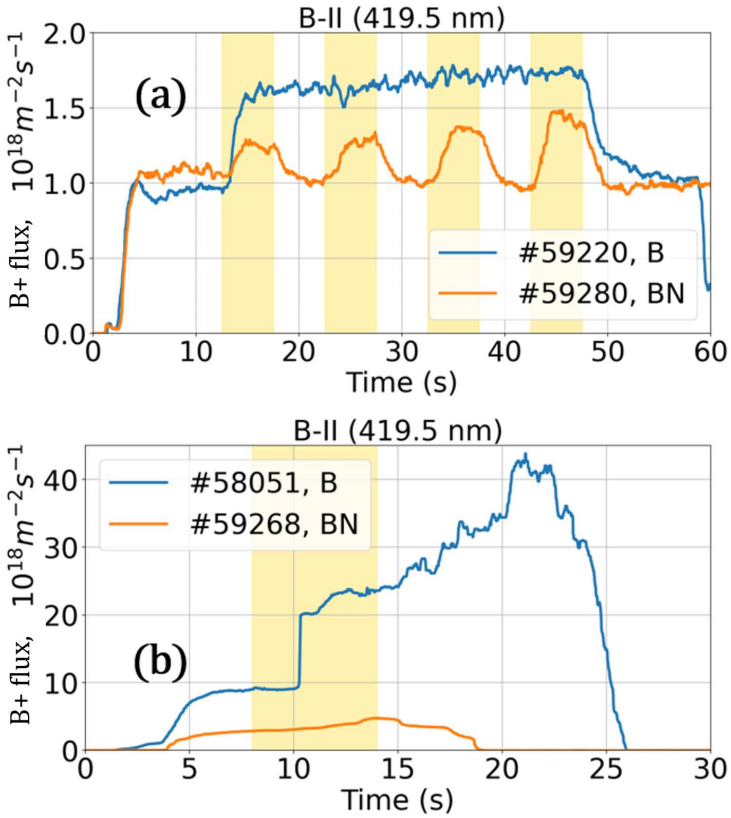

Figure 2.21. B^+ flux estimated with S/XB at the outer target of the lower divertor in (a) pulses with 3 MW of heating power and (b) with 4 MW of heating power. The yellow background denotes BN injection in the corresponding pulse.

These findings show that the reduction of low-Z impurities recycling via B deposit creation alone cannot explain the overall effect of B-containing powder injection on the O transport in the boundary plasma. Changes in boundary plasma due to the introduction of impurity ions must also be taken into account. A similar effect was also observed in WEST experiments with N impurity seeding, with $\Gamma_{O^+}^{S/XB}$ shown in figure 2.23. In both cases the reduction of $\Gamma_{O^+}^{S/XB}$ can be explained by the cooling of the SOL plasma due to impurity introduction, which affected interaction of O with the wall, e.g. reduced physical sputtering of O due to lower impact energy. N seeding appears to be a more effective method in transient suppression of O sputtering in WEST, while it lacks the cumulative conditioning effect.

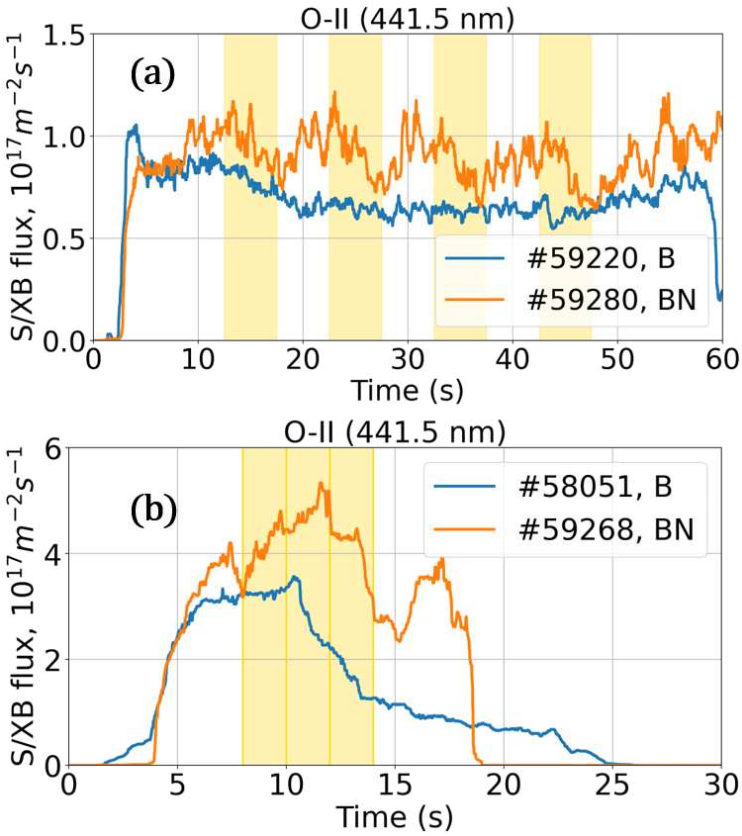

Figure 2.22. Same as 2.21, but for O^+ flux. Vertical yellow lines in (b) separate injection windows with V_{pp} = 2, 3, and 4 V.

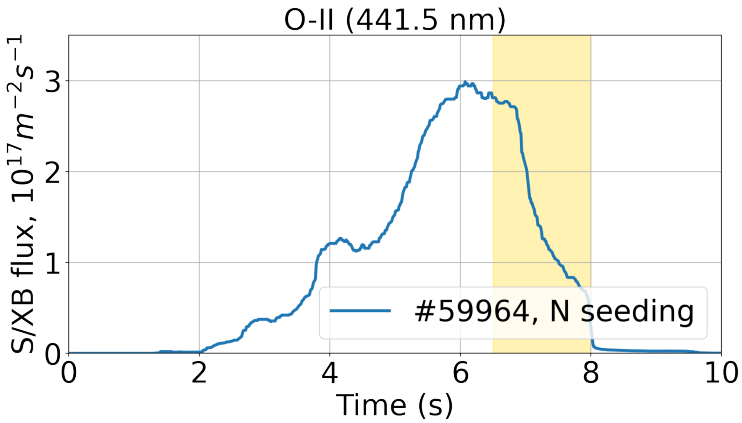

Figure 2.23. Same as 2.22, but for a pulse with N seeding. N injection is highlighted with a yellow background.

2.5 Summary of the experimental part of the thesis

In the higher drop rate series $M \approx 1$ g of B were injected, about three times greater than in the preliminary series of experiments for IPD commissioning [49]. Peak μ_B was also about three times greater, $\mu_B^{\text{peak}} \approx 58$ mg/s. In addition to previously observed effects of B injection that were also present in the preliminary series (W_{MHD} increase, effects on line emission from low-Z impurities and W, etc.), P_{rad}^{total} roll-over occurred at $\mu_B^{\text{threshold}} \approx 20$ mg/s. Considering that the conditioning effects were present for $\mu_B < 20$ mg/s, the roll-over is likely caused by the effect of B injection on W transport from the SOL to the core plasma and not due to, for example, reduced low-Z impurity recycling flux.

While T_e^{targets} was largely insensitive to the B powder injection, T_{app} of the lower divertor was affected by the injection, mostly due to lower particle flux caused by the recycling reduction. Thus B powder injection can be used to lower heat flux to the targets by decreasing incident particle flux.

Conditioning effects of B powder injection were compared to the effects of GDB. Similar levels of conditioning were obtained after the GDB conditioning with $M_B^{\text{GDB}} \sim 10$ g and after IPD injections with $M_B^{\text{IPD}} \approx 530$ mg, with a similar reduction rate of conditioning effects during 4 MW pulses. Conditioning via IPD injections appears to be a viable alternative to GDB in achieving higher performance that can be applied during a smaller amount of time (~ minutes of IPD operation vs ~ hours of GDB operation) and on demand.

On the other hand, performing boronization via IPD requires the PFCs to be in a good enough condition to perform the plasma pulse. If wall conditioning is required to achieve plasma breakdown, then IPD may not be used for this purpose. It can, however, be used to achieve higher performance, as indicated by the series of 4 MW pulses 59221-59224 enabled by a preceding pulse with B powder injection.

3 Modeling workflow description and results of the computational analysis

In this chapter, we will describe the results of the computational analysis of the WEST plasma pulses with B powder injections. The modeling workflow is described in section 3.1. Workflow validation and scan of input parameters in the preliminary model are presented in section 3.2. A model with a feedback on the density profile and a scan of input power and core O concentration are presented in section 3.3. A model with a scan of B drop rate and recycling coefficients $R_{D,O,B}$ is presented in section 3.4. A scan of input power and density with the revised model is presented in section 3.5.

3.1 Modeling workflow description

In our study, we approached the problem of IPD experiment modeling in a similar way to the method in Shoji et al. [51], with SOLEDGE3X-EIRENE code suite [70] modeling the boundary plasma, including B transport, and the Dust Injection Simulator (DIS) code [71] modeling powder dynamics and evaporation.

3.1.1 Boundary plasma modeling with SOLEDGE3X-EIRENE

The SOLEDGE3X-EIRENE boundary plasma numerical model consists of two coupled parts: SOLEDGE3X [70], a multi-species transport code that can simulate D plasma with multiple impurities, and EIRENE [72], which serves to model neutrals.

SOLEDGE3X models boundary plasma as a magnetized fluid by evolving fluid equations for $n_{e,i}$, $v_{\parallel}^{e,i}$, and $T_{e,i}$ with collisional closure derived by Zhdanov [73]. Transport equations in SOLEDGE3X are described in [70], with the mass balance equation being of particular interest to our study:

$$\partial_t n_\alpha + \vec{\nabla} \cdot (n_\alpha \vec{v_\alpha}) = S_\alpha^n$$

where n_α is the density of the ion α and S_α^n is the ion source due to ionization or recombination. The velocity $\vec{v_\alpha}$ is decomposed into the parallel and perpendicular components $\vec{v_\alpha} = v_{\parallel,\alpha}\vec{b} + \vec{v_{\perp,\alpha}}$, where $\vec{b} = \vec{B}/B$ is the direction of the magnetic field. Perpendicular velocity $\vec{v_{\perp,\alpha}}$ is calculated from cross-field transport equations that can involve cross-B drifts and anomalous diffusivity e.g. due to turbulence. In the simulations of the boundary plasma of the IPD experiment, cross-B drifts were not

taken into account, and a simpler, purely diffusive, one-dimensional radial transport model was used:

$$v_{\perp,\alpha}(\rho) = -\frac{D_\alpha(\rho)\partial_\rho n_\alpha}{n_\alpha}$$

where $D_\alpha(\rho)$ is the particle diffusion coefficient. $D_\alpha(\rho)$ is not calculated from first principles. $D_\alpha(\rho)$ could either be set to a uniform value or be controlled by the code in order to fit a prescribed radial ion density profile $n_\alpha(\rho)$, where ρ is the normalized magnetic flux surface coordinate (equal to 0 at the magnetic axis and 1 at the separatrix).

One of the benefits of using SOLEDGE3X as a plasma model is that the impurity ion species are fully coupled with the main ion species, which means that the impurity fluid species exert force on the main ion and vice versa. In the EMC3 plasma fluid model, for instance, the impurity species' transport is approximated with the impurity trace model [74], where the impurity distribution is calculated using the ion thermal and friction forces from the main ion, and the ionization and the excitation of the impurities provide an energy sink for the main ion. Main ion temperatures and temperatures of impurity ion species are computed individually in SOLEDGE3X.

Another feature of SOLEDGE3X which makes it an attractive choice is the extension of the spatial grid up to and into the PFCs, which allows to model plasma-wall interactions more thoroughly. Grid cells that are intercepted by the wall are masked out with the so-called "penalization mask" which sets wall boundary conditions in these cells.

While it is possible to use fluid equations for neutral particles as well, it requires the assumption of high collisionality, i.e. of the fact that the mean free path of a neutral particle is smaller than the length of the trajectory from the neutral emission source (recombination of an ion, recycling) to the ionization site. This assumption does not usually hold for most of the neutral particles in tokamak boundary plasmas, with the motion of the neutral particles being better described as an isotropic ballistic motion [75]. For this reason, SOLEDGE3X is coupled with a neutral particle transport code EIRENE [72]. EIRENE is based on the Monte-Carlo process of generating test ion particles near the wall surface, where they impact the surface material and generate atoms and molecules via recombination. EIRENE then tracks these neutral particles and handles their interactions with the plasma and the PFCs. Thus SOLEDGE3X provides EIRENE with the plasma parameters to generate test ions and model neutral-plasma interactions, and EIRENE provides SOLEDGE3X with the particle sources of ions.

3.1.2 Dust Injection Simulator

The Dust Injection Simulator (DIS) [71] is a dust tracking code developed to model the dynamics of dust particles in fusion plasma, which uses plasma parameters that are given to the model to compute the trajectory of an injected dust particle and its evaporation rate along the path until it is fully evaporated. It takes into account drag forces from ions, both main and impurities, and neutrals, current and energy balances

of the particle, as well as melting of the injected material, which is applicable to B. DIS was recently used to model powder injection experiments by Nespoli et al. [76] to study the distribution of B ions in the simulations of IPD experiments on LHD.

3.1.3 Modeling of IPD experiments in WEST

The modeling workflow consisted of three main steps. First, the pre-drop phase plasma was modeled in SOLEDGE3X-EIRENE (𝕊𝔼) with two elements, D as the main ion species and O as a proxy for all light impurities present in WEST before B injection, which are mostly B, O, C, and N [18]. Then, plasma parameters from a given D+O simulation ($(n,T)_{e,i,n}$, Mach number $\vec{M}$) were exported from 𝕊𝔼 to DIS, where a spherical B particle was launched vertically downward from the top of the machine. Then, the volumetric distribution of the B neutral atomic source (NAS) was scaled by the desired B powder injection rate, and the B atomic source was added back into the 𝕊𝔼 simulation, yielding D+O+B cases which represented the drop phase of a pulse with B powder injection. All of the simulations were performed time-independently, assuming a constant B source during powder injection.

Figure 3.1 depicts the simulation domain in 𝕊𝔼. The simulation grid was built based on the magnetic equilibrium reconstruction of WEST pulse 56919 from the Newton direct and Inverse Computation for Equilibrium (NICE) reconstruction code [77]. The equilibrium reconstruction was performed by averaging the data over the period of diverted phase of the pulse. NICE reconstructs the magnetic equilibrium by taking positions of magnetic coils and using them to calculate the magnetic field, with the solution constrained by the measurements from various diagnostics, which include magnetic diagnostics but also other diagnostics that provide e.g. plasma density and pressure measurements. Pulse 56919 from 2021 had the same magnetic configuration as the experiments in 2023-2024, so the mesh constructed from that equilibrium could be used in modeling IPD experiments both from the previous and the latest experiments. Plasma parameters and PFCs were assumed to be axisymmetric, i.e. the plasma model was two-dimensional, with a toroidal slice of WEST plasma being modeled instead of the entire vessel. Three-dimensional modeling is possible in SOLEDGE and WEST plasma was modelled in 3D [78] but it is not possible yet to perform 3D SOLEDGE models with EIRENE at full resolution and with a toroidally non-axisymmetric wall.

The walls were considered to be made of pure W when the energy loss of collisions of neutral particles with the wall was calculated (i.e. projectile surface binding energies of neutral D, O and B were set to the corresponding values of binding of D, O and B to W from TRIM database [79]), but W was not sputtered since it would make the simulations a lot harder to compute due to the high atomic number of W and thus, the high number of ion species (one for each ion charge). Since the plasma in this study was modeled in 2D, the geometry of the wall contour was assumed to be axisymmetric. In reality, WEST has toroidally localized antennae that act as poloidal limiters, which cannot be accurately described by a 2D model. The antennae have a toroidal length of approximately 30°, so in order to have a compromise in terms of the recycling flux

and cooling effect on the plasma, the portion of the wall contour that represents the antennae is placed at major radius R^{LHCD}=3.1 m, further away from the separatrix with respect to its actual radial position in the modeled experiment. This working assumption is consistent with previous WEST modeling efforts [80] [81] [82]. The inner boundary of the simulation domain was placed far from the separatrix in the confined plasma to also model B transport in the edge region, since there was evidence from the VUV spectroscopy (increase of 24.3 nm B-V line intensity) that B may be transported into the confined plasma [49].

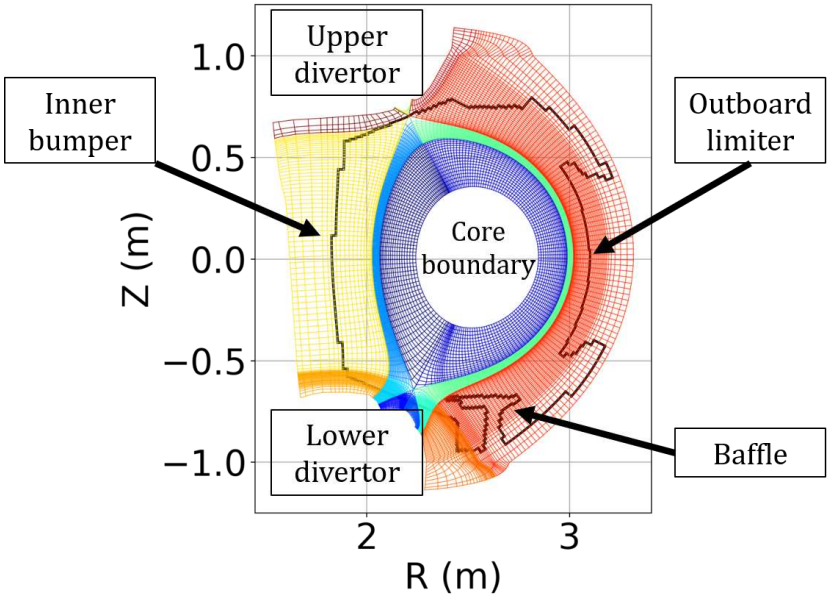

Figure 3.1. Quadrangular simulation mesh for SOLEDGE3X-EIRENE

After the D+O pre-drop phase model was calculated, B particle injection was modeled in DIS. The injection point was at R_{inj} = 2.6 m and Z_{inj} = 0.7 m, corresponding to the poloidal position of the IPD tube end on WEST (figure 3.2). In the DIS simulations a single B sphere represented a multitude of B grains dropped in the experiment similarly to the previous modeling efforts [51] [27]. The diameter of the particle was d_{part} = 150 μm which matched the size of the powder utilized in the experiment. Figure 3.2 shows the impact of particle size (15 to 150 μm) on the trajectory of B test particles for one of D+O $\mathbb{SE}$ simulations (simulation 1 in table 3.1). Main contributor to powder ablation was the evaporation of the melted B powder particle. Larger particles tended to penetrate the boundary plasma further and reach closer to the core as they were dragged outwards less by centrifugal forces. Similar results were observed in [51].

To model the drop phase of an IPD pulse, a source of neutral B atoms was added to the $\mathbb{SE}$ simulation based on the evaporation rate calculated by DIS. The B atom source rate per mesh cell was obtained by interpolating the NAS distribution over poloidal coordinates and sampling it at EIRENE mesh cells and then multiplying the sampled values by a scaling factor to have the total B atom source be equal to the desired powder injection rate in atoms s^{-1}. Total evaporation of the injected powder was

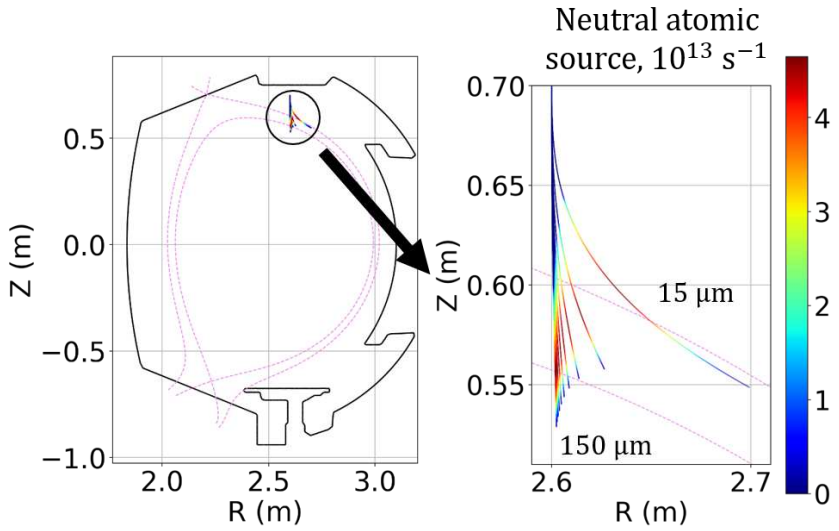

Figure 3.2. B particle trajectories provided by DIS and projected onto the poloidal plane with diameters ranging from 15 to 150 μm (from right to left). In color is the evaporation rate of the test particle.

assumed at this step. The injected mass rate was varied from 2.5 to 15 mg s^{-1}, while in experiments in the higher drop-rate series we reached ~60 mg/s, and ~5 mg/s in the lower drop-rate series. Drop rates above that typically led to the non-convergence of the numerical solution in $\mathbb{SE}$ in adequate time due to the large time derivatives of plasma parameter fields, leading to a small time step in the simulation. The B diffusion coefficient D_n^B was set to be equal to D_n^O. In order to add the B source generated from DIS, the interface between SOLEDGE3X and EIRENE has been modified to include an input in the form of a text file, which contains an array of triples (EIRENE mesh cell index, NAS, B atom temperature T_B). This array was calculated by taking the volumetric distributions of B NAS and T_B and sampling them in the EIRENE mesh cells, integrating NAS, and averaging T_B.

After the addition of the B source, a D+O+B $\mathbb{SE}$ simulation is calculated to model the drop phase of the IPD pulse. Main plasma parameters such as P_{in}, and reference n_e^{OMP} were not changed at this point to make it possible to compare the effects of B injection on the plasma in the numerical model and the experiments. The only parameter that was varied was $R_{D,O}$ to account for the effect of low-Z impurity gettering by the injected powder, which is discussed further in section 4.

3.2 Workflow test and parameter scan with constant $D(\rho)$

After the workflow was developed, input parameters were scanned to obtain a qualitative match with the experimental data with a pulse 56919 from the preliminary

IPD experiment on WEST [49] in order to test the workflow and to establish a basis for further model refinements and scans. First, P_{in}, D_2 gas puff rate and O source (set as a boundary condition on O density at the core boundary) were varied to obtain a simulation that resembles experimental data from preliminary IPD experiments, based on the n_e^{OMP} from reflectometry and n_e^{lower} from embedded Langmuir probes that were compared to the plasma parameters in the model such as n_e^{OMP}, $(n,T)_e^{(\text{outer,inner})}$. T_e^{OMP} was not included due to lack of T_e measurements in SOL. As a result, $P_{in} = 1$ MW, puff rate of 1.17×10^{20} s^{-1} and O concentration at the core $C_O^{core} = 3\%$ were chosen as an initial basis for further simulations and future refinements ($\mathbb{SE}$ allows to set absolute values for n_O^{core} boundary condition, so n_O^{core} was varied with the change of n_D^{core} to preserve the ratio). Then, P_{in} and D diffusion coefficient D_n^D were varied to study the sensitivity of the model to those variations and to perform first studies on the correlation of B influx distribution with various plasma parameters. These parameters were chosen due to the disagreement of the experimental data and the data from the base simulation with the parameters listed above on n_e^{OMP} and $(n,T)_e^{(\text{outer,inner})}$, and the scan served to find more optimal model input parameters to match experimental data while studying the effect of the variations of these parameters on B influx distribution. Four D+O simulations were calculated in the result of that scan, with their parameters given in table 3.1.

Simulation #	P_{in}, MW	D_n^D, m^2 s^{-1}
1	1.0	0.6
2	0.75	0.6
3	1.0	0.5
4	0.75	0.7

Table 3.1. Parameters for pre-drop simulations in $\mathbb{SE}$ in P_{in} and D_n^D scan

Experimental and numerical profiles of n_e^{OMP}, and $(T,n)_e^{\text{outer}}$ are shown on figure 3.3. While there was a match of n_e and T_e at the lower divertor (figures 3.3b and 3.3c) and of n_e in the far SOL, that method was not successful in matching n_e in the edge and near SOL, likely due to the uniform radial distribution of D_n^D, which is addressed in further sections.

Despite the mismatch of n_e^{OMP} in the the edge and near SOL, these preliminary results were used to compare the distributions of the injected B in the simulations and in the experiments. In the scan of input parameters, bolometry data were used as a measure of the presence of injected B, since in preliminary WEST IPD experiments [49] all bolometry signals S correlated positively with the amount of B powder injected. Bolometry channels 1, 2, and 3 were used for the radiated power from the lower divertor plasma, and channels 14 and 15 were used for the upper divertor plasma, as shown in figure 3.4. Pulse 56919 was chosen for the comparison as it was one of the pulses of that campaign with the biggest B drop rate $\mu_B = 9.2$ mg/s and without disruption. S in the experiment were averaged in pre-drop and drop phases (5.6 s $\leq t_{\text{pre-drop}} \leq$ 6.6 s, 8.0 s $\leq t_{\text{drop}} \leq$ 13.0 s). S in the simulations were calculated using

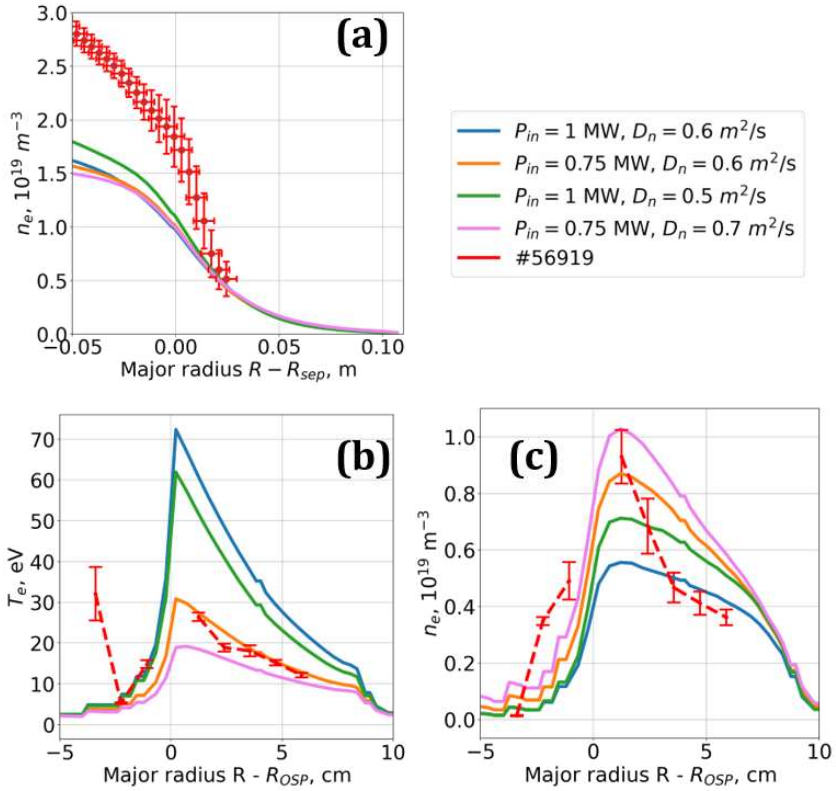

Figure 3.3. n_e^{OMP} profiles (a), T_e^{outer} (b) and n_e^{outer} (c) profiles at the lower divertor from a pulse 56919 (red) and simulations with D gas puff 1.17×10^{20} s^{-1}, P_{in} and flat D_n^D profile (solid lines). n_e^{OMP} in 56919 was provided by reflectometry, $(n,T)_e^{\mathrm{OMP}}$ were provided by embedded Langmuir probes.

a synthetic diagnostic code called SYNDI [60], to which a 2D P_{rad} radiance map was provided to calculate S. SYNDI calculates synthetic S by multiplying 2D maps of emissivity provided by $\mathbb{SE}$ with weight coefficients for each LoS from a given diagnostic. The resulting matrix is then integrated to obtain the synthetic measurement for a given LoS.

For each of the four D+O $\mathbb{SE}$ simulations described above, a D+O+B simulation was calculated by injecting 9.2 mg/s worth of B atoms (which corresponded to the drop rate in 56919) into the plasma along the trajectory of a B particle calculated with DIS. Bolometry signals from the experiment in pre-drop and drop phases and from corresponding D+O and D+O+B $\mathbb{SE}$ simulations $S_{\mathrm{pre-drop,drop}}$ are shown in figure 3.5, left and middle columns. The bolometry signals are grouped in the upper divertor and lower divertor LoSs to compare the distribution of injected B between the upper and the lower parts of the machine in the experiment and in the simulation (figure 3.5, upper and lower rows). Ratio $S_{drop}/S_{pre-drop}$ was then calculated for both the experimental and synthetic data to serve as a proxy for B concentration at a given LoS of the bolometry, given in the right column of figure 3.5.

While there was a significant discrepancy in the absolute values of bolometry signals

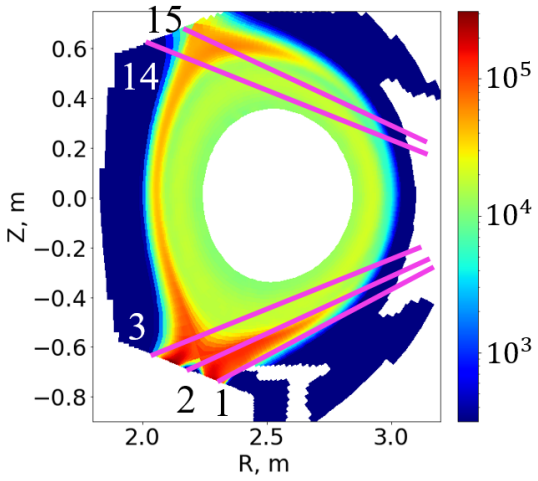

Figure 3.4. 2D map of P_{rad} in one of the simulations with bolometry lines of sight in magenta

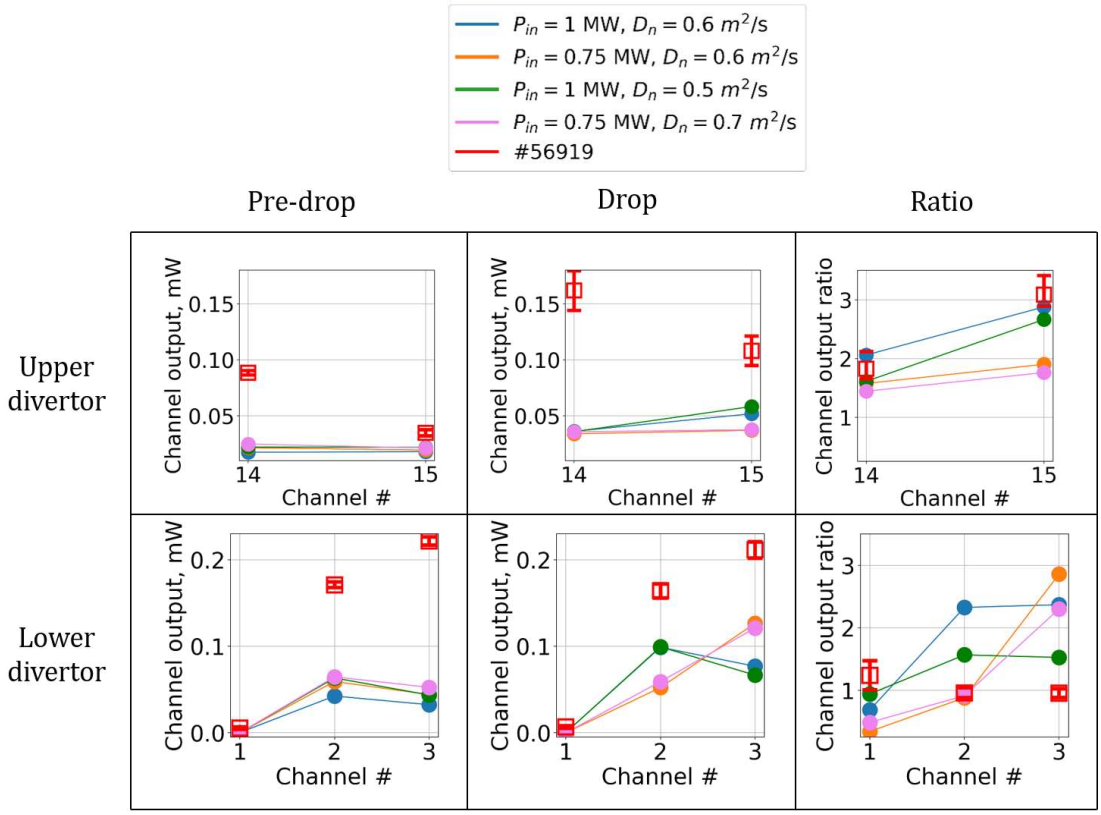

Figure 3.5. Bolometry signals in 56919 pulse from the preliminary experimental campaign (red boxes), and in simulations (colored dots and lines), with a scan of P_{in} and D_n^D. Columns are for pre-drop, drop phases, and the ratios of signals between them, rows are for lower and upper divertor.

between experimental and the synthetic data, there was a qualitative match between the ratios $S_{drop}/S_{pre-drop}$. The quality of the match of $S_{drop}/S_{pre-drop}$ appears to be greater at the upper divertor than at the lower divertor. This might be caused by the assumption of $R_{D,O} = 1, R_B = 0$ which does not hold in the experiments. It is also of note that fixed R_B is a strong simplification of B interaction with PFC since it is deposited in the solid phase, unlike gaseous impurities. A more realistic simulation would take it into account by modeling B re-entry into the plasma as sputtering, with sputtering yield dependent on the energy and the incident flux of the sputtering ions. As a result, $S_{drop}/S_{pre-drop}$ is close to 1 in the experiment at the lower divertor, while in the simulations it varied significantly. Simulations with $P_{in} = 0.75$MW showed trends of $S_{drop}/S_{pre-drop}$ that were different from the other simulations, because in the simulation the injected B powder triggered a transition from an attached divertor regime to a detached one, with n_e at X-point being a lot greater than $n_e^{\text{OMP,target}}$, which did not happen in the experiments on WEST (figure 3.6).

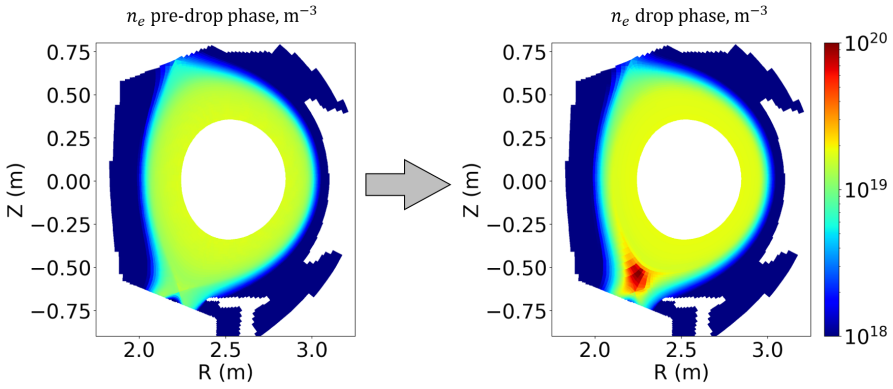

Figure 3.6. n_e in pre-drop and drop phase of a simulations with $P_{in} = 0.75$ MW

These observations indicate that, while the assumption of $R_{D,O} = 1, R_B = 0$ is likely introducing discrepancies in the lower divertor plasma, and that P_{in} needs to be sufficiently large to properly model the drop phase of an IPD pulse, the B transport predicted by the model was qualitatively similar to the B transport in the experiment and that the model could be used to inform future experiments.

To investigate the effect of various plasma parameters on B transport and deposition, the normalized wall deposition B flux was calculated for each drop phase simulation:

$$\Gamma^B_{\text{norm}} = \Gamma^B(L) / \int \Gamma^B(L) dL,$$

where $\Gamma^B = \Sigma_{i=0}^{5} \Gamma^{B_i}$, L is the wall contour length, Γ^{B_i} is the wall incident flux of B in the ith ionization state for $i > 0$ and the neutral B wall incident flux for i=0. One-dimensional plots of $\Gamma^B_{norm}(L)$ along the wall are given in figure 3.7 for different sets of input parameters. The peak of $\Gamma^B_{norm}(L)$ at the baffle is one cell wide and is an artifact of the geometry of the wall at the tip of the baffle. The Γ^B_{norm} distribution stayed approximately the same for the variations in P_{in} and D^D_n. Interestingly, in all

of the drop phase simulations, the upper divertor received a substantial amount of B with respect to Γ^{B}_{norm} on the lower divertor, at least 50% despite the LSN configuration (although upper divertor X-point is very close to the wall contour, figure 3.1). This point will be brought up in further numerical analysis; for now, validation of this influx ratio against measurements remains unsolved due to the lack of visible spectroscopy data near the upper divertor during the preliminary IPD experiments.

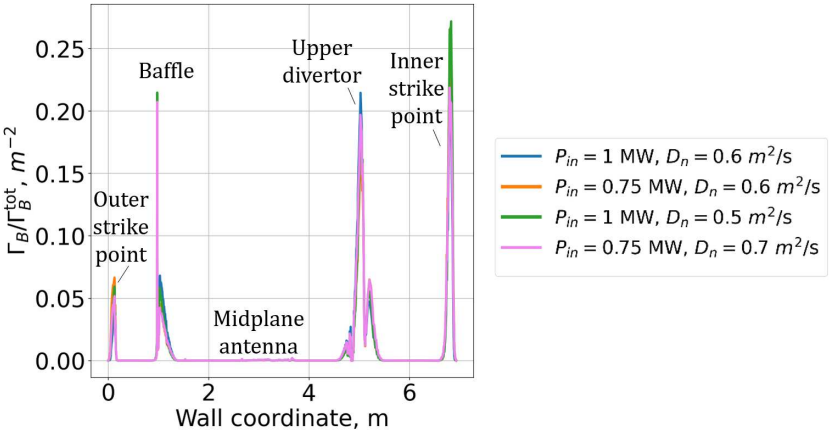

Figure 3.7. Wall profile of normalized B influx with indications of wall elements (0 near outer strike point, counterclockwise)

3.3 Scan of P_{in} and C_O^{core} with a feedback on $D(\rho)$

In order to address the discrepancies noted in the previous section, $D(\rho)$ was set with a control algorithm with a feedback on the D density profile n_D^{OMP} to match a reference profile [83]. The reference profile $n_D^{\mathrm{OMP,\,ref}}$ was estimated by taking n_e^{OMP} from the pulse 56919 measured with the reflectometry diagnostic during the pre-drop phase and manually downscaling it by multiplying it by a radially constant factor to account for the presence of impurities. While $\mathbb{SE}$ allows to set the feedback on $D(\rho)$ and/or the D puff rate, the former was preferred due to a better match of n_e profile in the SOL.

With n_e^{OMP} being bound by experimental data, P_{in} and C_O^{core} were varied to scan the parameter space to analyze their effect on the B transport. P_{in} was prescribed as a core boundary condition on heat flux, and C_O^{core} was prescribed by setting core boundary condition for absolute value of n_O^{core} to be equal to a desired fraction C_O^{core} of the electron density at the core boundary. A set of nine pre-drop simulations were calculated with varying P_{in} and n_O^{core} values, given in table 3.2. For simulations to better represent the pulses from the experiments, P_{in} in the simulation should equal to $P_{heating} - P_{rad}^{core}$ from the experiment. Here we recall, $P_{heating}$ is the total heating power in the experiment, and P_{rad}^{core} is the radiated power emitted by the plasma in the experiment from the toroidal region enclosed with the core boundary defined in the simulation mesh (shown in figure 3.1). P_{rad}^{core} was approximated with

$P_{rad}^{bulk} = P_{rad}^{total} - P_{rad}^{div}$, where P_{rad}^{div} is the radiated power from the plasma regions near the divertors (chords 1-3, 14, 15 in figure 3.4). In the case of the pre-drop phase of pulse 56919 $P_{rad}^{bulk} \approx 1.9$ MW, therefore $P_{in} \approx P_{heating} - P_{rad}^{bulk} = 2.6$ MW. For the simulations, we chose three values of P_{in} above this estimation, since P_{rad}^{bulk} is an overestimation of P_{rad}^{core} due to bolometry LoSs passing through the midplane section of the SOL.

P_{in}, MW	2.75	2.875	3.0
n_O^{core}, 10^{17} m^{-3}	7.58	8.34	9.10
$C_O^{core} = n_O^{core}/n_D^{core}$, %	2.36	2.59	2.83

Table 3.2. Parameters for pre-drop simulations in $\mathbb{SE}$

One of the goals of this modeling scan was to obtain a better match of the plasma parameters in the simulation with the ones measured in the experiment. Figure 3.8 shows experimental data from pulse 56919 and the parameters from a subset of simulations with the opposite extreme values from the scan (higher C_O^{core}, lower P_{in}, medium values for both and lower C_O^{core}, higher P_{in}): n_e^{OMP}, $(n,T)_e^{\mathrm{outer}}$ and $S_{\text{pre-drop}}$ at the lower and upper divertors. While there was no numerical solution that had a quantitative match of all the compared parameters, overall the match was closer than in the previous scan: there was a quantitative match of n_e^{OMP} in the confined plasma and a better match of the bolometer chord intensities S in the pre-drop phase. In the far SOL, however, all pre-drop simulations had a higher n_e^{OMP} than n_e^{ref}, which is attributed to $R_{D,O} = 1$, as it will be shown in further $\mathbb{SE}$ models. The difference of the S trend with the channel number at the lower divertor in the experiment and in the simulations (figure 3.8(b)) is likely due to the assumptions about $R_{D,O} = 1$. The difference of S trends at the upper divertor (figure 3.8(c)) is attributed to the inaccurate representation of magnetic equilibrium in the upper part of the vessel [80].

To model B injection, varying amounts of B powder (mass rate μ_B=2.3, 4.6 mg/s) were injected into the simulations described above. B drop rates beyond 4.6 mg/s led to non-convergence of the numerical models in a timely manner similar to the previous scan, again due to the time step constraint by the large time derivatives of fields. Similar to the analysis in the previous section, Γ_{norm}^B distribution on the wall contour was calculated. One-dimensional plots of $\Gamma_{\mathrm{norm}}^B(L)$ along the wall are given in figure 3.9 for different sets of input parameters, this time with varying C_O^{core}, P_{in} and μ_B. Based on that figure, it is expected that in IPD experiments on WEST upper divertor and the inner target of the lower divertor receive B due to its first flight deposition, whereas other PFCs would receive B due to its subsequent re-erosion and redeposition. Similarly to the cases from the previous section, $\Gamma_{\mathrm{norm}}^B(L)$ distribution stayed approximately the same for the variations in P_{in}, μ_B and C_O^{core}, with B being spread more homogeneously (lower at the upper divertor and inner target, higher at the baffle) at higher P_{in} and lower μ_B, all other parameters being equal. Same as in the previous scans, the upper divertor received a greater amount of B influx than the lower divertor. A difference of 1.5-4 times between the integrated incident fluxes of B ions and neutrals to the upper and lower divertors was estimated despite the LSN

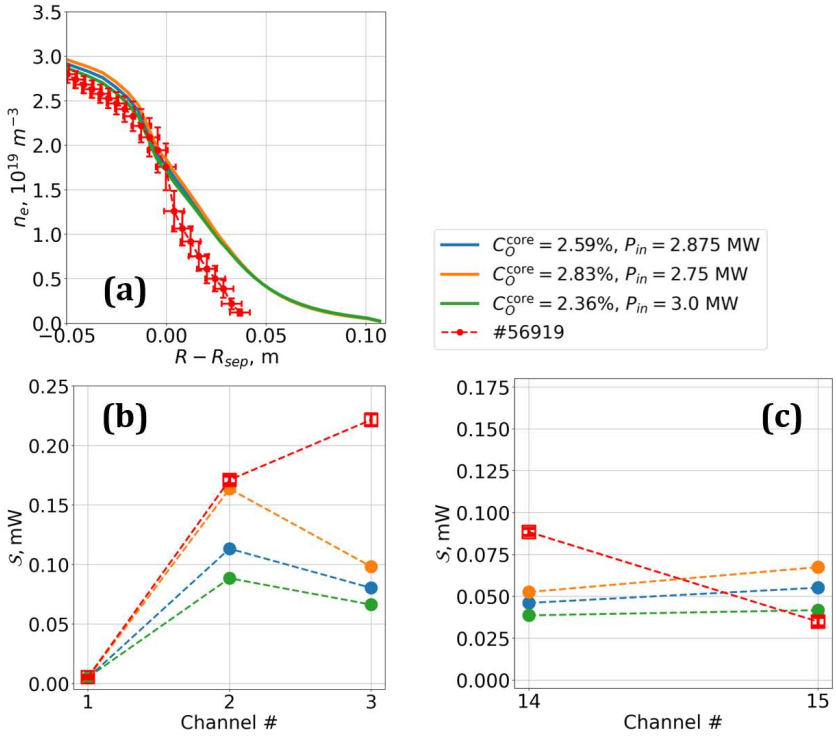

Figure 3.8. Plasma parameters in simulations (solid lines) and experiment measurements (red dashed lines, error bars) in pre-drop phase: n_e^{OMP} (a), bolometry signals S at the lower (b) and upper (c) divertors

configuration.

The modeling results also suggested that the outer target received little to no injected B when compared to the other PFCs such as the baffle. In contrast, the experiment showed similar levels of B-II line brightness measured with visible spectroscopy at the baffle and the outer target in the pulse 56919, shown in figure 3.10. Spectroscopy measurements from the experiment could not be compared with the synthetic diagnostic data from simulations provided by SYNDI as there was no B recycling or re-erosion in the numerical model. Therefore, there were practically no B+ ions at the lower divertor, as B+ ions were only present in the vicinity of the neutral B source.

Having modeled both pre-drop and drop phases, we can now compare the impact of B injection in the experiments with the impact of adding a B source in the simulations. Similar to the previous scan, a ratio of bolometry measurements $S_{drop}/S_{pre-drop}$ was calculated for each simulation using SYNDI and compared with the ratio from the experiments. The effect of B injection on S was qualitatively reproduced at the upper divertor for both pre-drop and drop phases, especially with higher μ_B (figure 3.11), indicating that matching drop rates in simulations with the ones in the experiments is one of the necessary prerequisites for matching other plasma parameters. In particular, synthetic bolometry signals for simulations with higher μ_B at the upper divertor show a 2-3 times increase, similar to bolometry measurements increase in the experiment. The discrepancy between channels 14 and 15 in modeling and experiments could

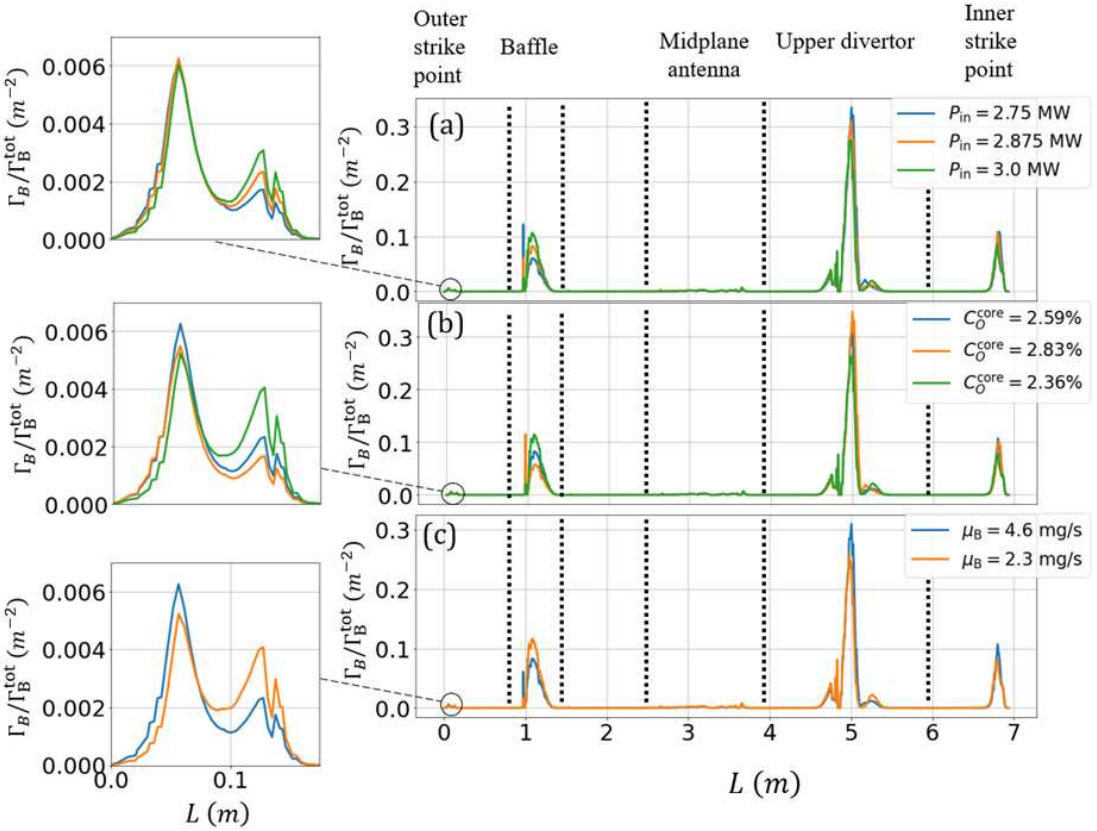

Figure 3.9. Normalized distribution of B total incident flux summed over all B species Γ^B_{norm} for drop phase simulations with the variations of: (a) P_{in}, with C_O^{core}=2.59% and B mass rate μ_B=4.6 mg/s (b) C_O^{core}, P_{in}=2.875 and μ_B=4.6 mg/s (c) μ_B, C_O^{core}=2.59% and P_{in}=2.875

again be attributed to an inaccurate representation of magnetic equilibrium in the upper part of the vessel. The difference in trends of the lower P_{in}, higher C_O^{core} simulation (figure 3.11, orange) is due to its low P_{in} which causes B powder injection to trigger detachment at the lower divertor (figure 3.12), changing P_{rad} distribution with stronger radiation near the X-point region, that corresponds to the bolometer channel 3.

At the lower divertor, the impact of B injection on experimental and synthetic bolometry signals greatly differs, as shown in figure 3.11 in the lower row. Synthetic signals increased for channels 2 and 3 and decreased for channel 1, while in the experiment, the bolometry signals remained approximately constant. The channel 1 signal behavior may be explained by the sensitivity of the model to near-target plasma parameters and by lower light impurity concentration near the outer target relative to volume near inner target, an effect that was studied by Effenberg et al. [27] and tied to the balance between friction and thermal terms in the momentum equation. As for channels 2 and 3, considering that the increase of the bolometry signal in the simulation is caused by the increased radiance of the plasma due to the

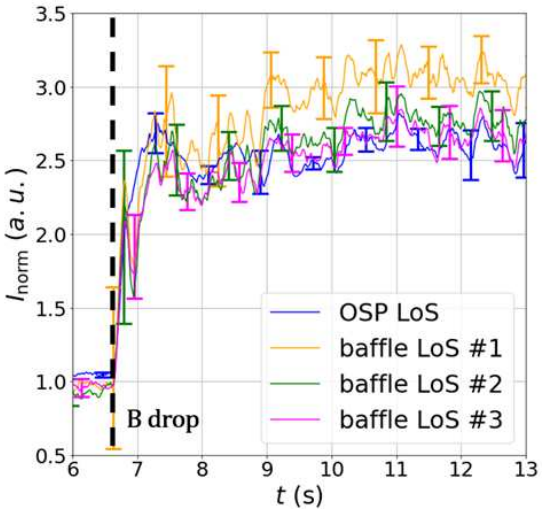

Figure 3.10. Line intensity of B-II (λ=419.5 nm) in the experimental pulse 56919 at the baffle and outer target (LoS closest to the strike point), normalized by pre-drop values.

injected impurities, the discrepancy suggests that the numerical model overestimates the impurity concentration in the lower divertor plasma.

The lack of the effect of B injection on the lower divertor bolometry measurements in the experiments can be attributed to the phenomena not taken into account in the scan: the most likely candidate for this effect is reduced D and O recycling, which were not modeled here as the wall properties were assumed to be static. In the simulations, R_B was set to zero, i.e. B was simply pumped by the wall without affecting the D recycling ($R_D = 1$). A similar discrepancy was found between the $(n,T)_e$ measured by the embedded lower divertor Langmuir probes and that estimated from the simulations. In every simulation, B injection resulted in a 2-10 times decrease of the peak T_e^{outer} and a similar increase of the peak n_e^{outer}, which was not consistent with the experimental results. In the experiment, B powder injection had no effect on e.g. T_e^{outer}, as shown in [49] and in figure 3.13.

Another comparison between the B injection effects from the experiment and the $\mathbb{SOLEDGE}$ results was made using spectroscopy data for the O-II line brightness at 4415 Å. As in the case of P_{rad}, an emissivity map for an O ion was calculated based on the parameters of a plasma simulation, and then brightness signals for different lines of sight of a synthetic spectrometer were obtained with SYNDI.

The lower divertor LoS with the brightest O-II signal from shot 56919 (which happened to be a line near the OSP) was selected for the analysis. During pulse 56919, the injection of B powder resulted in a decrease in the O-II line intensity as shown in figure 3.14. This was attributed to the reduction of O recycling due to the B gettering effect [49]. In the scan, however, the O-II line intensity increases with the addition of a neutral B source (figure 3.15) despite using the same O source as the core density boundary condition. This result, similar to the bolometry analysis, strengthens the argument that the decrease in O-II line intensity in the experiment was caused by the

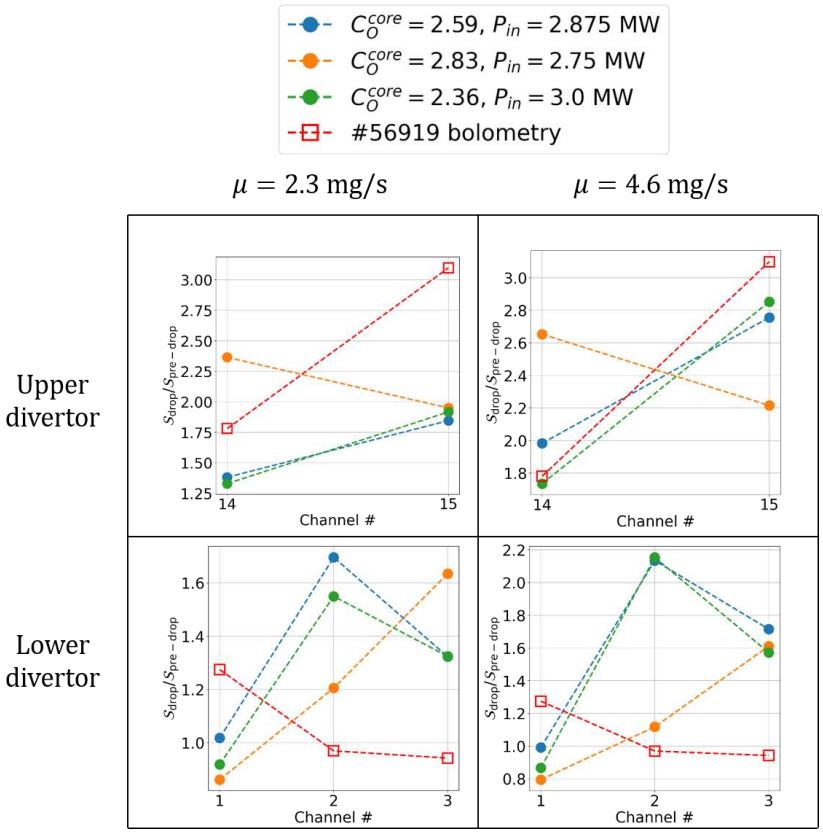

Figure 3.11. Bolometry signal ratios $S_{drop}/S_{pre-drop}$ from the experiment (red boxes) and calculated with SYNDI for studied simulations: $S_{drop}/S_{pre-drop}$ for B mass rate μ_B=2.3, 4.6 mg/s (columns) for the lower divertor (lower row) and the upper divertor (upper row).

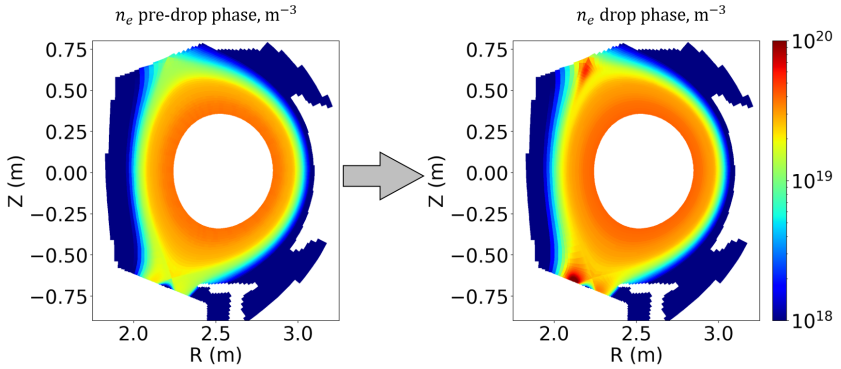

Figure 3.12. n_e in pre-drop and drop phases of a simulation with $P_{in} = 2.75$ MW.

O gettering by B and, therefore, the reduction of O recycling, an effect which could not be modeled in the presented scan.

We draw the conclusion from the evidence presented above, that the variation of $R_{D,O}$ with μ_B is an important effect that should not be omitted in the modeling of

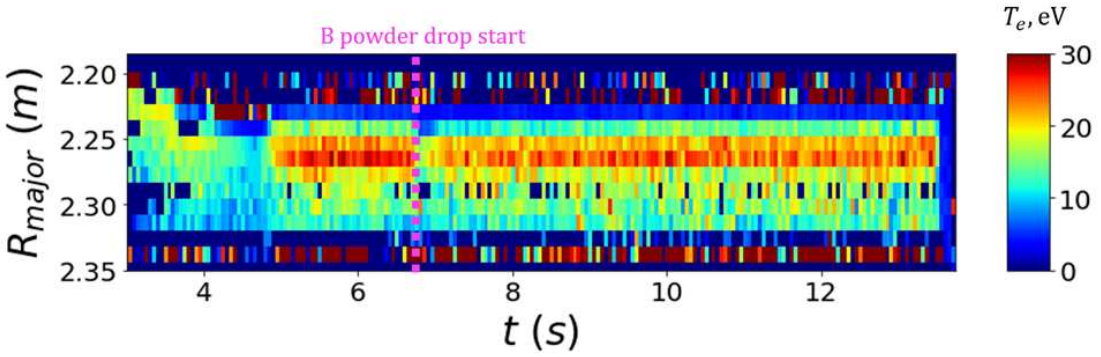

Figure 3.13. Embedded Langmuir probe measurement of T_e^{outer} profile over time in pulse 56919

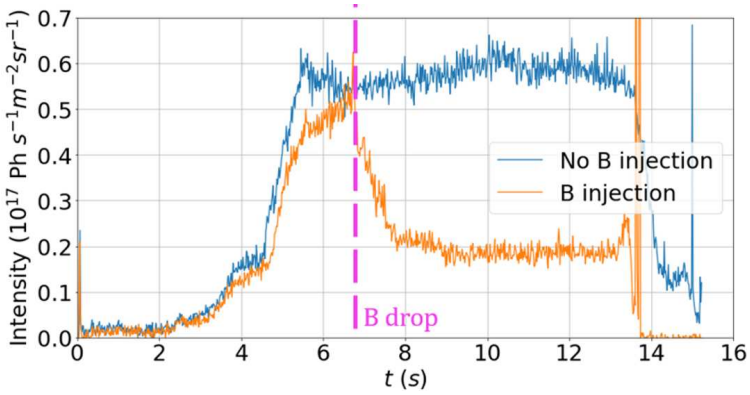

Figure 3.14. Time traces from two shots (control 56915 and with B powder injection 56919) from an IPD experiment on WEST: O-II (λ=441.5 nm) visible line intensity at the outer target (LoS closest to the strike point), lower divertor

IPD experiments: in the absence of the effect of B injection on D and O recycling $(n,T)_e^{\text{outer}}$ changes in the simulations do not match measurements in the experiments; O radiance $I_{\text{O-II}}(\mu_B)$ shows a dynamic opposite to the one observed in the experiment. Finally, IPD pulses with higher μ_B could not be effectively modeled due to the non-convergence of $\mathbb{SE}$ algorithm, most likely due to high n_e at the strike points, which decreased the time step of the simulation by ~2 orders of magnitude, not allowing to finish the computation in adequate time.

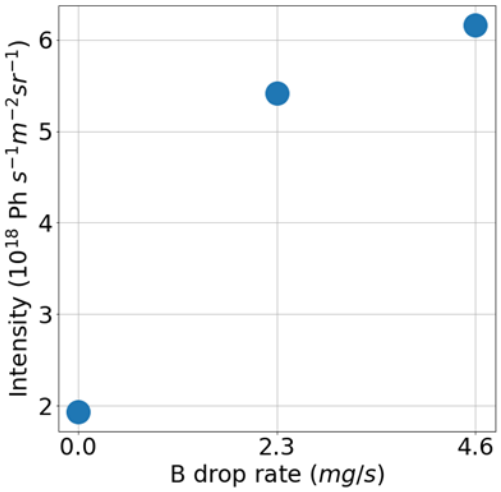

Figure 3.15. Line intensity for the O-II (441.5 nm) line for simulations with the P_{in}=2.875 MW, C_O^{core}=2.59% and varying B drop rate

3.4 Scan of B drop rate and recycling coefficients

As discussed in the previous section, B injection in the experiment led to the decrease of the O-II line intensity as opposed to the simulations where the O-II line intensity increased. This may be explained by the lack of gettering effect and co-deposition of O in the model. Insensitivity of lower divertor Langmuir probe measurements of n_e, T_e to B injection in the experiment and their sensitivity in the numerical models shows that the effect of B powder on D recycling and O gettering effects is a fundamental aspect that has to be included in the future modeling efforts.

In order to address this issue and to lower the discrepancy between the simulations and the measurements, additional refinement of the workflow was performed. First, the reference n_e^{OMP} profile for the feedback algorithm in $\mathbb{SOLPS}$ was redone with higher fidelity in the SOL region. This refinement was also warranted by the change of experimental data source since these simulations were performed after the C7 experiments in 2023. In these newer simulations pulse 58051 from the 2023 IPD experiment with 4 MW of P_{heating} was used as a source of simulation input parameters and as a source of experimental data for the comparative analysis, because higher drop rate series of IPD pulses, from which pulse 58051 was chosen, had greater operational domain (greater μ_B, M_B) when compared to the preliminary IPD experiments. $R_{D,O}$ were varied for a better match of n_e^{OMP} profile at the lower divertor in the pre-drop phase.

As a result of these scans, a base case D+O simulation with $R_{D,O} = 0.95$ was produced that served as a starting point for other simulations and corresponded to the pre-drop phase of the pulse 58051. Comparisons of n_e^{OMP} and $(n,T)_e^{\text{outer}}$ in the base case simulation and in the pre-drop phase of the pulse 58051 are given in figures 3.16-17. Due to optimized $R_{D,O}$, $n_e^{outer,inner}$ matched the experimental data, allowing to better reproduce the plasma conditions near the divertor targets.

Leveraging the insight from the simulations described in the previous section that

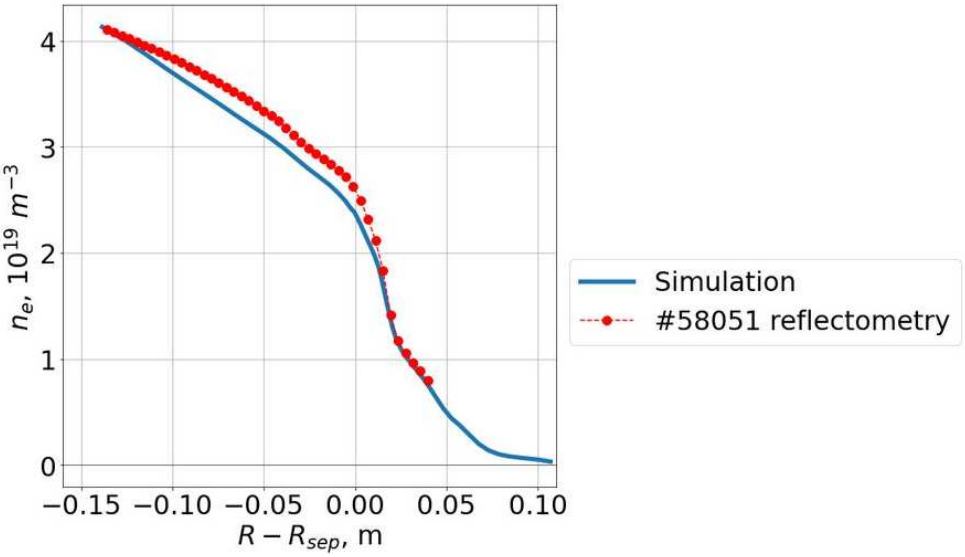

Figure 3.16. n_e^{OMP} in the base case simulation (blue) and in the pre-drop phase of the pulse 58051, averaged over the time window $8.5 < t < 10$

$R_{D,O}$ reduction during the B injection might play a key role in modeling the drop phase, a scan of B drop rates from 0 to 15 mg/s was performed while also changing $R_{D,O}$ in order to match peak n_e^{outer} in the drop phase of the pulse 58051. R_B was set to 0.75 to match visible spectroscopy measurements from the experiments with synthetic measurements calculated with SYNDI. Figure 3.18 shows $R_{D,O}$ that were necessary to reproduce peak n_e^{outer} for a given μ_B.

Without changing $R_{D,O}$ even a small B source of 1 mg/s was enough to drastically change the divertor plasma regime in the simulation: a factor of 5 increase of n_e^{outer} and $T_e^{\mathrm{outer}} < 5$ eV, indicating detached conditions (figure 3.19). At the same time, in the experiment, embedded Langmuir probe measurements of $n_e^{\mathrm{outer,\ inner}}$ stayed either relatively constant (experiments in 2021, 2024) or decreased (e.g. 58051 in 2023). This discrepancy in the absence of $R_{D,O}$ modification confirms once more that the gettering qualities of B are responsible for this discrepancy between the plasma model and the experimental data.

In addition to the effects on $(n,T)_e^{\mathrm{outer}}$ change of $R_{D,O}$ also affected O+ ion flux Γ^{O+}. In order to compare the effect of B injection on O+ fluxes in the experiment and in the modeling, the ratio of Γ^{O+} in drop and pre-drop phase simulations was compared to the ratio $\Gamma^{O+}_{\mathrm{drop}}/\Gamma^{O+}_{\mathrm{predrop}}$ estimated in the experiment with S/XB analysis. For the simulations, a case with $\mu_B = 15$ mg/s was chosen, while for experimental data average O+ flux estimates were taken from pre-drop phase of the pulse 58051 and from a time window 15 s $< t <$ 17.5 s of the drop phase of the same pulse, where average B drop rate according to the calibration was equal to 17 mg/s.

$\Gamma^{O+}_{\mathrm{predrop,drop}}$ estimates from the experiment and values from simulations are given in figure 3.20. While the absolute values of the fluxes in the simulation are ~2 orders of magnitude greater than in the experiment, the ratios of the fluxes before and

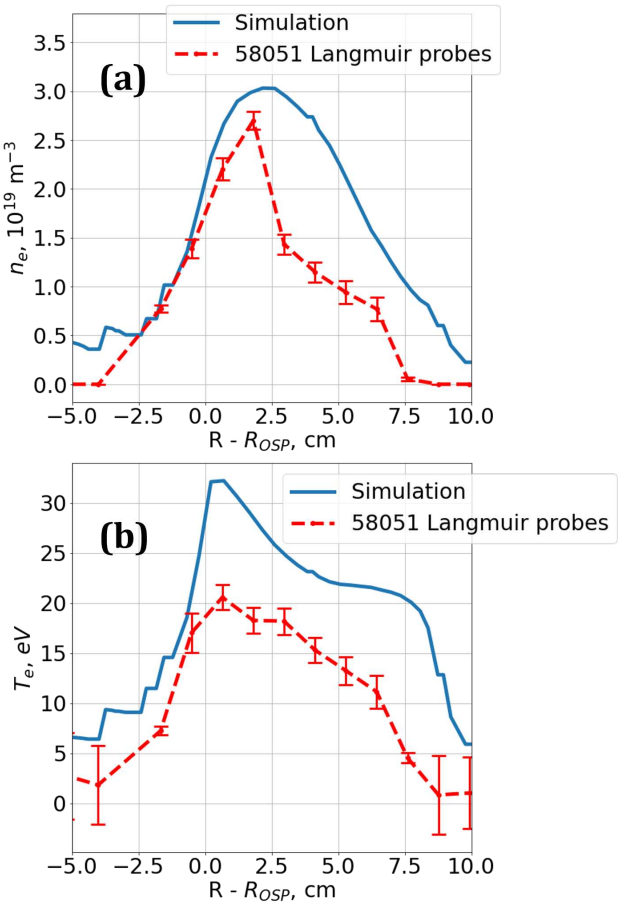

Figure 3.17. n_e^{outer} (a) and T_e^{outer} (b) in the base case simulation (blue) and in the pre-drop phase of the pulse 58051, averaged over the time window 8.5 $s < t < 10$ s

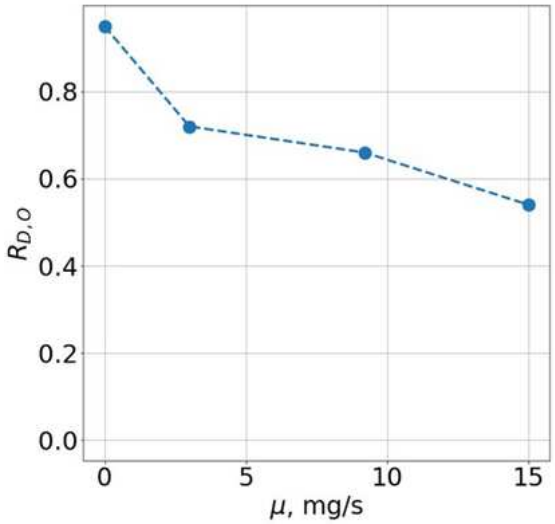

Figure 3.18. Effect of μ_B on $R_{D,O}$ in $\mathbb{SE}$ simulations

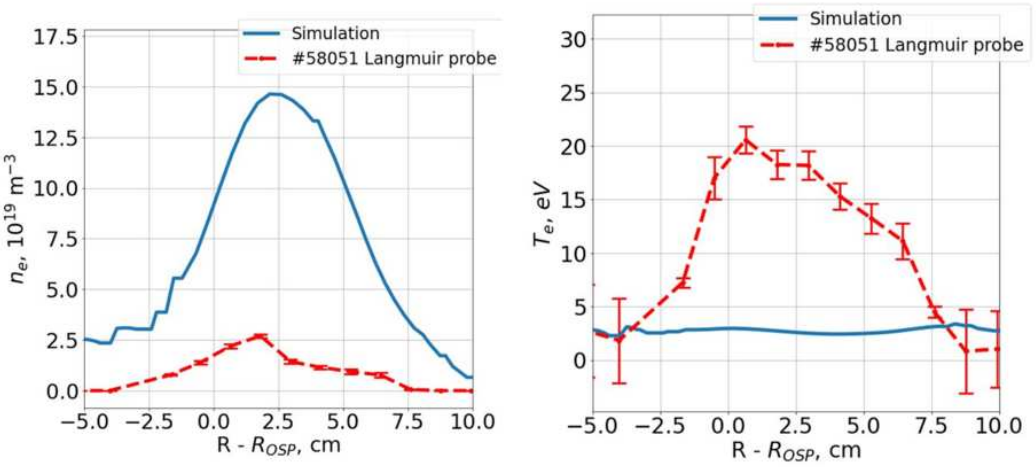

Figure 3.19. Same as figures 3.17(a, b), but with 1 mg/s of B source added in the simulation and $R^{\text{drop}}_{D,O} = R^{\text{predrop}}_{D,O}$. Experimental data averaged over the time window 10 $s < t < 12.5$ s, corresponding to B drop rate of 8.4 mg/s

during the B injection are very similar. Indeed, O was the only impurity besides B in the simulation and acted as a proxy for all other impurities for a better match of boundary plasma parameters. With that, the effect of B injection on Γ^{O+} appears to be very similar, helping us to assert that the gettering effect of B during the injection is responsible for light impurity removal near the divertor.

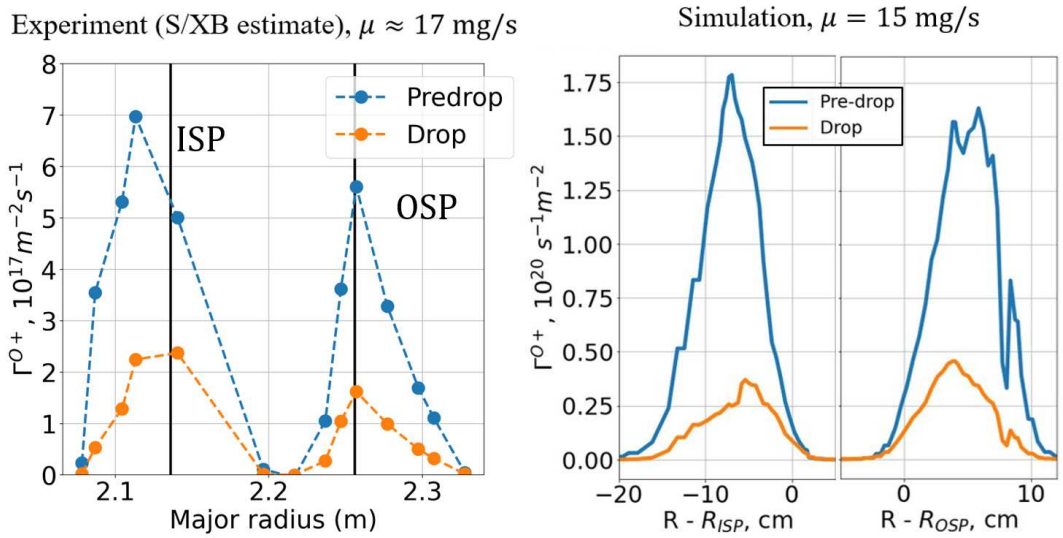

Figure 3.20. $\Gamma^{O+}_{\text{predrop,drop}}$ S/XB estimates in the experiment (pulse 58051, 15 s $< t <$ 17.5 s) and $\Gamma^{O+}_{\text{predrop,drop}}$ from the simulations.

3.5 Scan of input parameters in the revised model

After a quantitative match of plasma parameters in the numerical model with the measurements was obtained, we performed another scan of P_{in} and n_e^{OMP}, as well as a scan of the radial position of the IPD to study the sensitivity of Γ^B_{norm} distribution to these parameters in the revised model.

3.5.1 Scan of P_{in} and n_e^{OMP}

Similarly to previous scans, P_{in} was varied by changing boundary conditions of the simulations, and n_e^{OMP} was varied by scaling the reference profile for the density feedback algorithm. A D+O simulation from section 3.4 was used as a base case, and B neutral source in produced D+O+B simulations was equivalent to 15 mg/s. To study the effect of P_{in} on B transport, simulations with P_{in} = 3.0, 3.25, 3.5 MW were produced, and to study the effect of n_e variation, a simulation with $n_D^{\mathrm{OMP}} = 0.7 * n_{D,base}^{\mathrm{OMP}}$ was performed, where base subscript refers to the base case simulation.

In addition, another simulation was calculated to represent a long pulse scenario from the IPD experiment described in section 2.3, where 3 MW of P_{heating} were injected as opposed to 4 MW in the experimental scenario represented in the simulations in the previous scans. The differences between the long pulse and high power scenarios include the width of the SOL, which is broader in long pulse, and the difference in the magnetic configuration due to I_p difference (400 kA in long pulse configuration vs 500 kA in high power configuration, causing reduction of B_θ). However, the main features of the magnetic equilibrium (B_T, strike point position, distance from the lower divertor to the X point) were very similar, so the computational mesh did not have to be changed. To reflect the difference in P_{heating} in $\mathbb{SE}$ simulations, P_{in} in the simulation of long pulse scenario plasma was lowered by 25%. Lower n_e^{OMP} was represented by multiplying $n_{D,base}^{\mathrm{OMP}}$ by a factor of 0.625, to match the ratio of $\langle nl \rangle_{\mathrm{central}}$ between the pulses in two scenarios. The simulation parameters of the scan are enumerated in table 3.3.

Simulation #	Input power P_{in}, MW	$n_e^{\mathrm{OMP}} / n_e^{\mathrm{OMP,\ base}}$
1 (base)	2.75	1
2 (power)	3.0	1
3 (power)	3.25	1
4 (power)	3.5	1
5 (density)	2.75	0.7
6 (long)	1.964	0.625

Table 3.3. Parameters for pre-drop simulations in $\mathbb{SE}$ in P_{in} and n_e^{OMP} scan with revised base case

The total B deposition flux to the wall in the simulations from the scan is given in figure 3.21. The ratio of Γ^B_{norm} between the lower and upper divertor changed significantly in favor of the lower divertor when compared to the simulation scans with

no B recycling: from $\Gamma^B_{\text{norm, upper}}/\Gamma^B_{\text{norm, lower}} \approx 2$ with $R_B = 0$ to ≈ 0.4 with recycling (compare e.g. with the Γ^B_{norm} distribution from the figure 3.9), indicating that the recycling of B, as well as the sputtering and re-deposition following the initial deposition of injected B, plays a major part in the transport of IPD-injected B. The distribution of B influx in the scan, however, remained relatively unchanged, showing that n_e, P_{in} variation does not play a significant role in the transport of the injected B. This finding differs from the one by Shoji et al. [51] due to the difference in B injection locations relative to the magnetic field features: in LHD the trajectory of the injected B goes through the upper divertor leg of the plasma, where changes in n_e can significantly alter the trajectory of the B particle, causing it to miss the ergodic region of the plasma, a behavior which was not observed either in the experiments on WEST or in the simulations presented so far.

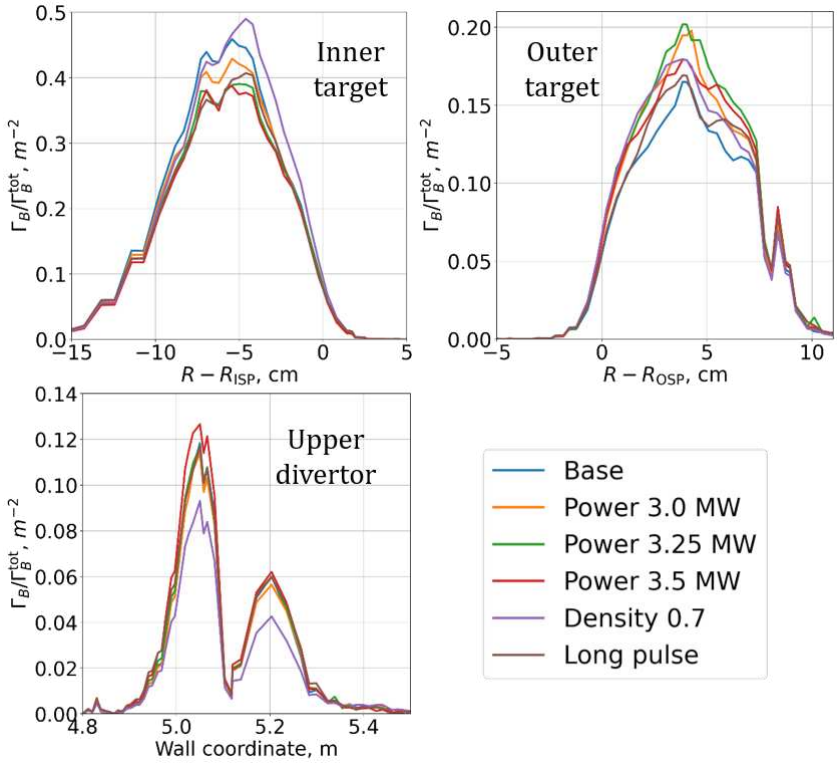

Figure 3.21. Γ^B_{norm} on the outer and inner targets of the lower divertor and the upper divertor in the scan of P_{in} and n_e^{OMP}.

3.5.2 Scan of the radial position of IPD

Previously it was shown that the B recycling and re-deposition may be significant contributors to the dynamics of B transport in WEST, while the variations of $(n, T)_e$ appear to be less significant. Another parameter that was not previously discussed is the radial position of the IPD, R_{IPD}. This parameter may be important because the injection of B powder in $\mathbb{SE}$ happens to be in the vicinity of the *stagnation point*

of the main ion: region of the plasma where the flow of D^+ reverses, which can be seen in the figure 3.22. To investigate the effect of relative position of the IPD and the plasma on the B influx distribution on the PFCs, four simulations with modified R_{IPD} were calculated: $R_{\mathrm{IPD}} = 2.4,\ 2.5,\ 2.7,\ 2.8$ m, with $R_{\mathrm{IPD}} = 2.6$ m being the base case. The modification was performed by changing the initial radial position of a B particle launched in DIS.

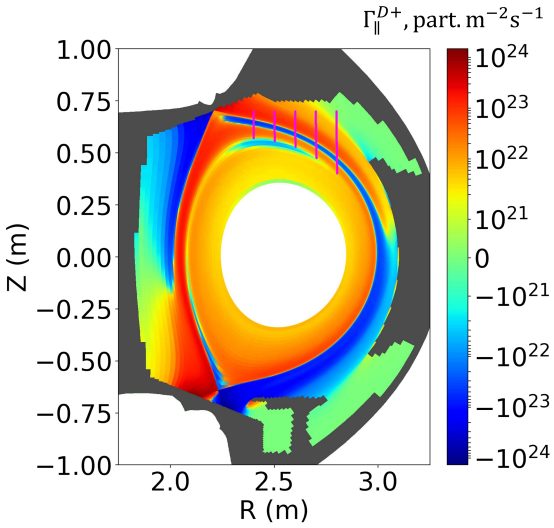

Figure 3.22. $\Gamma_{\parallel}^{D^+}$ (part. m^{-2} s^{-2}) distribution with five B trajectories in magenta (base case in the middle). Positive sign corresponds to the direction along the magnetic field (counterclockwise)

In this scan Γ^B_{norm} shows much greater dependence on varying R_{IPD}, as can be seen in figure 3.23. The ratio $\Gamma^B_{\mathrm{norm,\ inner\ target}}/\Gamma^B_{\mathrm{norm,\ outer\ target}}$ varied with the change of R_{IPD} from ≈ 1.6 to ≈ 6.4 while in the previous scan this ratio stayed between 2.3 and 3.2. $\Gamma^B_{\mathrm{norm,\ upper}}/\Gamma^B_{\mathrm{norm,\ lower}}$ in this scan varied between 0.3-0.45, which is approximately the same range of values as in the previous scan, with the upper divertor receiving greater Γ^B with an outboard shift of R_{IPD}: longer path to the upper divertor allows more B to be transported across the field lines.

In particular, variation of R_{IPD} had an effect on B^+ parallel flux $\Gamma_{\parallel}^{B^+}$ as shown on figure 3.24. The effect on $\Gamma_{\parallel}^{B^+}$ is of special interest because it can be compared with the $\Gamma_{\parallel}^{B^+}$ derived from the line intensity of the B II line at 419.5 nm using the respective photon efficiency S/XB of IPD experiments, which was described in section 2.3.1. When compared to the S/XB estimates of $\Gamma_{\parallel}^{B^+}$ in IPD experiments (figure 3.25), an outward shift of $\Delta R_{\mathrm{IPD}} = +10$ cm allowed to better match the distribution of $\Gamma_{\parallel}^{B^+}$ between the inner and outer targets. This fact indicates that the chosen modeling parameters might lead to an incomplete picture of particle transport in the simulation, and in particular to a placement of the stagnation point that significantly differs from the one in the experiments, causing the distribution of $\Gamma_{\parallel}^{B^+}$ along the flux tube in the simulation to be different from the one in the experiment, affecting $\Gamma^B_{\mathrm{norm,\ inner\ target}}/\Gamma^B_{\mathrm{norm,\ outer\ target}}$

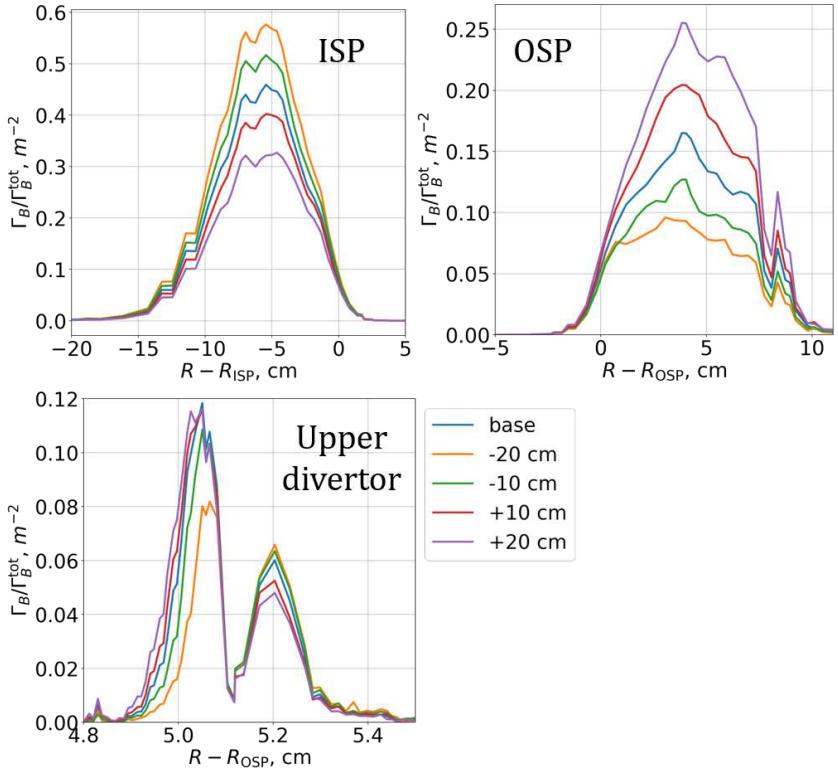

Figure 3.23. Γ^B_{norm} on the outer and inner targets of the lower divertor and the upper divertor in the scan of R_{IPD}

ratio. This could be caused by the lack of modeling of cross-B drifts or lack of turbulent transport in the simulations.

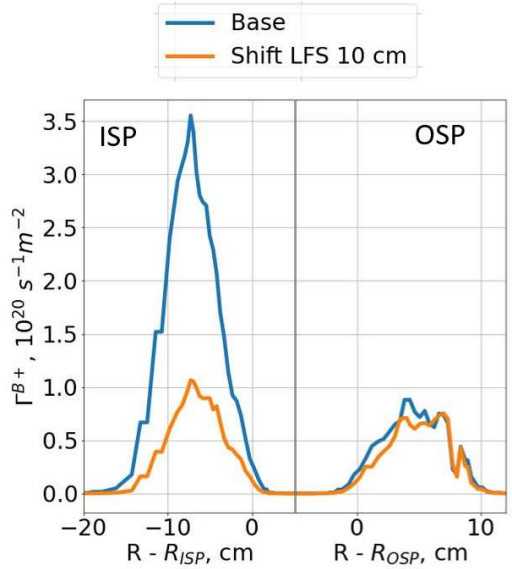

Figure 3.24. $\Gamma_{\parallel}^{B^+}$ on the lower divertor in base case D+O+B simulation (μ = 15 mg/s) and the simulation with an outward radial shift of IPD location of 10 cm.

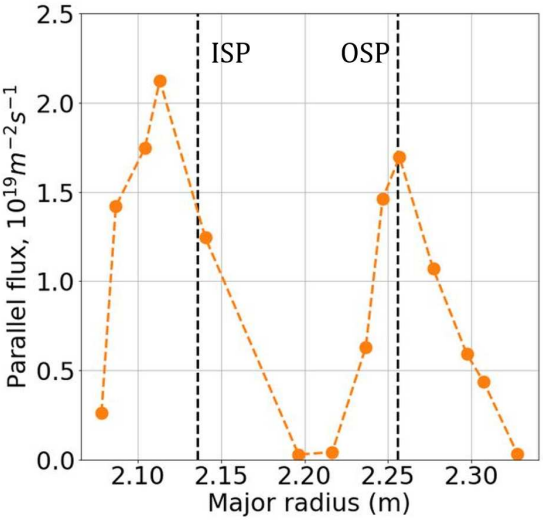

Figure 3.25. S/XB estimation of $\Gamma_{\parallel}^{B^+}$ on the lower divertor in 58051 with drop rate ~ 17 mg/s.

3.6 Summary of the modeling part of the thesis

A quantitative match of some of the quantities in the numerical model with experimental data was achieved in pre-drop and drop phases ($(n,T)_e^{\text{targets}}$, n_e^{OMP}), and for other quantities a qualitative match was obtained (ratio of $\Gamma_{\parallel}^{O^+}$ between drop phase and pre-drop phase, $S_{drop}/S_{pre-drop}$ at the upper divertor). A scan of plasma parameters was performed to study the sensitivity of Γ^B distribution to the variation of $(n,T)_e$, P_{in}, C_O^{core} and R_{IPD}. The scans showed that Γ^B varies very little with these parameters except for R_{IPD}. While the absolute position of the IPD on the machine cannot be practically varied, the strong effect of R_{IPD} on Γ^B in the simulations shows that the B transport depends on the relative position of the IPD and the plasma, in particular the position relative to the stagnation point.

In the scan of μ_B R_B was set to a non-zero value to match the visible spectroscopy measurements from the experiments with the synthetic ones. Variation of μ_B necessitated reduction of $R_{D,O}$ to match $(n,T)_e^{\text{targets}}$ (figure 3.18). This is consistent with the effects of impurity injection in the experiments, where an injection of an impurity that does not adhere to a surface (e.g. N) would cause strong changes of $(n,T)_e^{\text{targets}}$ and eventually trigger detachment, while B powder injection would not affect $(n,T)_e^{\text{targets}}$ significantly even at $\mu_B^{max} \approx 60$ mg/s. With that, $R_{D,O}$ necessary to match $(n,T)_e^{\text{targets}}$ profiles at $\mu_B = 15$ mg/s was significantly smaller than the albedo of the pump in the simulation. Such a low value could be an overestimation due to the lack of e.g. turbulent transport in the SOL which could have been suppressed by B injection, which is expected to happen in the experiments but was not accounted for in the numerical model.

4 Discussion of the results

First, let us discuss the status of the goals set in the beginning, section 1.10:

1. Higher drop rate and cumulated mass were achieved during IPD experiments on WEST when compared to the IPD experiments commissioning campaign in 2021 (~58 mg/s vs ~17 mg/s, ~1 g vs ~300 mg respectively [49]);

2. Even though only ~10% of B mass that is typically injected in a GDB on WEST was injected in the 2023 campaign, the conditioning effects of the GDB and IPD were comparable; in addition, transient effects during the injection were observed, such as the increase of W_{MHD} and neutron flux;

3. IPD injections were performed with the new divertor; one of the reasons why WEST plasmas sustained higher B powder drop rate in 2023 compared to the experiments in the commissioning campaign appears to be the installation of the new divertor, cleaner W surface of which reduced f_{rad}, allowing for higher injection rates;

4. $\mathbb{SE}$-DIS workflow was developed to study the transport of the injected B in WEST plasma. Using the workflow it was established that the distribution of B flux on the PFCs is weakly dependent on $(n, T)_e$ profiles of the plasma;

5. A scan of R_{IPD} was performed, showing that the radial position of the IPD relative to the plasma is responsible for the ratio of Γ_B between the inner and outer targets; however, the ratio of Γ_B between the upper and lower divertors was not affected;

6. Scan of B source and $R_{D,O}$ allowed to estimate the effect of B injection on the recycling of main ions and light impurities, showing strong effect on $R_{D,O}$, which was also suggested by the experimental data.

To draw the conclusions and discuss the results of this study we will go through the experimental and modeling results, while trying to find the ways in which they complement each other.

In the two series of experiments on WEST, the positive effects of B powder injection on the confinement, that were first observed in the preliminary experiments with IPD, were confirmed and the main causes for such improvement were established: the gettering and reduction of recycling of the main ion and light impurities, together with the reduction of impurity transport due to the boundary plasma dilution caused W_{mhd}, T_e^{central} and neutron rate to increase. We expect B powder injection to have a

similar effects in L-mode discharges in ITER, while the effects in H-mode discharges might be weaker, due to already suppressed turbulent transport in the edge plasma.

The recycling reduction effect is suggested by the cumulative effects of B powder injection in pre-drop phases of each pulse. B-II, O-II and W-I lines were noticeably affected by the injections in previous pulses, even when μ_B did not exceed the P_{rad} roll-over threshold. The effect was similar in magnitude to GDB conditioning even for significantly smaller M_B.

The gettering of the impurities and the reduction of impurity transport are harder to discern. On one hand, effects of B powder injection are clearly different from the effects of N seeding, where N does not adhere to the surface: $(n,T)_e$ varies more strongly, and divertor plasma changes to the detached regime in N injection experiments, while in B/BN powder injection experiments effects on $(n,T)_e$ were a lot milder, and n_e even decreased for high enough μ_B. This difference can be attributed to the gettering effect that happens during the powder injection, effectively strongly reducing D and low-Z impurities' recycling, compensating for the electrons introduced by the injected powder. On the other hand, gettering alone cannot adequately describe the effects of powder injection: in the low drop rate series where both B and BN were injected in pulses with otherwise same parameters (P_{in}, n_e, magnetic configuration etc.) BN powder appeared to have an effect on O-II visible line at the lower divertor similar to the one caused by B powder injection, even though mass-wise less than a half of BN powder is constituted by B which can getter O (figure 2.22). At the same time N radiates more than B with line emission, and considering that N injection also affected O flux measured with S/XB (figure 2.23), it can be assumed that the more intensive line radiance, and subsequently stronger cooling of the SOL and the related effects on impurity transport, could compensate missing B in BN powder injection.

The presence of seeding-like effects of B powder injection appears to be another advantage of IPD usage during a discharge. However, B powder injection does not appear to be a well-qualified alternative to N seeding in machines operating without T due to restrictions on IPD position and lower emissivity of B compared to N. In machines operating with T both B injection and N seeding have their disadvantages (dust accumulation vs ammonia formation, both of which contribute to T retention), thus more information is needed to pick a better alternative.

While the effect of B powder injection on light impurities appears to be two-fold, the effect on W transport appears to be primarily driven by the changes in the SOL transport. W-I line radiance at the outer target correlated linearly with μ_B in higher drop rate series for the entire range of μ_B, suggesting increased sputtering of W by B. W-I line radiance at the inner target behaved differently, it experienced a roll-over at $\mu_B \approx 30$ mg/s (figure 2.12a), which appeared to be caused by the partial detachment of the inner leg of the plasma. Nevertheless, n_W^{core} and P_{rad} roll-over occurred at a lower threshold $\mu_B \approx 20$ mg/s, so it could not have been caused by the partial detachment of the inner leg. Increased W sputtering rate with decreased n_W^{core} suggests that the primary reason for the roll-over is the effect of injected B on W transport, possibly by suppressing cross-B turbulent transport [64].

In the scan of μ_B and $R_{D,O}$ in $\mathbb{SE}$ model we had to lower $R_{D,O}$ down to 0.58 for $\mu_B = 15$

mg/s, which is significantly smaller than the pump albedo in our $\mathbb{SE}$ simulations. In other words, the wall in the simulations was a bigger sink per surface area than the vacuum pump. Such a strong effect on $R_{D,O}$ might be an overestimation caused by the lack of turbulent transport in pre-drop phase simulations, which could have been suppressed by adding B.

Another interesting question is the evolution of P_{rad}^{total} in the assumption of an indefinitely long drop phase. As the B deposits would grow their erosion rate r_{ero}^{B} would likely match the deposition rate r_{dep}^{B} in the limit of infinitely long drop phase: B deposits would start to flake away from the PFCs, releasing trapped low-Z impurities. In that case one would expect P_{rad}^{total} to return back to pre-roll-over value in the case of practical saturation of PFCs with B. The appropriate duration and μ to achieve this effect remains unclear.

Unlike in [51], the variation of n_e did not appear to significantly affect the distribution of Γ_B, which we linked to the fact that B is injected far from the divertor legs, so the B particle trajectory is not significantly affected by n_e. Similarly, variation of P_{in} did not significantly affect the distribution either. If the goal of B powder injection is to condition the PFCs as evenly as possible, then changing the magnetic configuration of the plasma might be necessary, as the radial position of the IPD relative to the plasma appears to be the only controllable factor with a significant effect on Γ_B.

Neither in [51] nor in [27] R_D was varied to account for the effects of B deposits gettering. While $R_B = 0$ (B sticking to the wall) might be sufficient to match some plasma parameter like $(n,T)_e^{\text{targets}}$, the comparison of B-II visible spectroscopy line radiance from the experiment with the one calculated with SYNDI from the modeling data required non-zero R_B, which in turn required adjusting $R_{D,O}$ to match the experimental data. In an idealized, infinitely long drop phase, where r_{ero}^{B} matches r_{dep}^{B}, one would expect R_B to reach 1 when PFCs saturate with B, together with other recycling coefficients.

It is also worth to note that, since B is deposited in a solid phase, its reintroduction into the plasma is better described with sputtering rather than recycling, which makes the B influx from PFCs dependent on the temperature and the flux of the sputtering species (B for self-sputtering, but also O and D) rather than just that of B.

Our experiments revealed some advantages of conditioning via IPD when compared to GDB in addition to previously stated ones. Only a small fraction ($\sim 5\%$) of B mass in typical GDBs had to be injected in the higher drop rate series to achieve a comparable effect on the cumulative conditioning (O-II line brightness, f_{rad}). We need to keep in mind that the accumulation of B dust caused by GDB is a concern for ITER due to its effective increase of surface area of PFCs, enhancing T retention. Considering that similar effects were achieved with the fraction of M_B in 15 seconds total of B powder injection time and that the rate of which the conditioning effects faded away from pulse to pulse appeared to be similar after both GDB and IPD conditioning, IPD conditioning appears to be an attractive alternative to GDB. Operating IPD, however, requires the machine to be able to achieve plasma breakdown, and IPD cannot aid in achieving that. If the boronization is required only for achieving breakdown, GDB

remains a preferred conditioning method.

The reasons for the comparable conditioning effects of IPD boronization and GDB despite the great difference in injected B mass remain unclear. One possible reason is the difference in B deposits' distribution on the PFCs. Since IPD injections are performed in the presence of the magnetic field, B is likely to be transported to the divertors, as indicated by the $\mathbb{SE}$ modeling in chapter 3. In GDB on WEST, however, B is ionized and driven towards the wall via potential gradient caused by six anodes and negatively charged wall without the magnetic field to affect the B ion transport. It remains unclear what features of these distributions play a major role in the conditioning effectiveness: it could be that the in IPD boronizations PFCs near the wetted areas, that would get higher heat and particle fluxes compared to other PFCs and would sputter more impurities, receive more B, and B deposits on them are thicker, allowing for greater conditioning.

5 Future research

This chapter concludes the dissertation with an outlook to the future of the research of B powder injection on WEST.

In the experimental part a larger operational domain of IPD is desired. While in the higher drop-rate series μ_{max} and M_{max} were both tripled compared to the previous experiments, M_{max} still constituted only ~ 10% of the total injected B mass in a GDB. Considering that most of that mass was injected over three pulses, it is very realistic and desirable to achieve $M \geq 10$ g in one experimental session to, firstly, have a better comparison of IPD and GDB conditioning techniques and secondly, to check if the conditioning effects will saturate past a certain M threshold. We did not manage to achieve $M \geq 10$ g due to the miscalibration of the IPD, which caused us to spend multiple pulses on injecting $\mu_B \approx 0$ mg/s.

Another way to expand the operational domain is to increase P_{LHCD} to obtain lower f_{rad}, which clearly acts as a limiting factor for IPD injections, as observed e.g. in ICRH-heated pulses. Pulses with $P_{LH} \geq 5$ MW were recently achieved on WEST, and it would be worthwhile to attempt injecting B at much higher rates in such pulses. IPD injections at 5 MW were even attempted in the end of the campaign in the first semester of 2024, but the machine was not in a favorable state, and all pulses disrupted before B powder injection could have been performed.

Another part of the experimental portion of the research worth discussing is influencing Γ_B to spread more homogeneously or to target specific PFCs. As shown in the scan of R_{IPD} in $\mathbb{SE}$ modeling, relative position of the IPD to the plasma center/SOL may be a key to affecting the distribution of Γ_B across the wetted PFCs. One other configuration that was not considered neither in the experiments nor in modeling is limited magnetic configuration. On one hand, plasma limited on a W PFC would be expected to condition that PFC better during a B powder injection. On the other hand, WEST limited configuration is typically limited by BN tiles that do not require boronization, and limiting the plasma on a W surface may lead to an increase of f_{rad} to such a degree that B powder injection would become impossible.

It would also be interesting to try to discern between the gettering effect and the effects on the impurity transport in the SOL by e.g. injecting both B and BN at the same time at different ratios to compare the effects for different values of μ_N/μ_B. For that a more robust calibration would be necessary and higher drop rates are desirable to have a bigger operational space ($\mu_B + \mu_N, \mu_N/\mu_B$) to analyse. Similarly, a comparison of effects of B and Li injections is also desirable, since the interactions of the injected impurity with the plasma and the walls are considerably different for Li due to its lower melting point and lower atomic charge.

A similar experiment could be performed by combining B powder injection and N

seeding to establish an importance of N source position and to investigate whether the B drop rate can be reduced while keeping the same transient reduction of the recycling of D and light impurities.

Studies of W samples exposed to B powder injection using e.g. thermal desorption spectroscopy would be beneficial to have a better understanding on the effects of B deposits introduced by IPD on D and impurity retention. Comparative analysis of such samples with analogous samples from GDB would give more insight on similarities and differences of the two approaches to wall conditioning.

In this thesis, studies of the conditioning effects compared IPD conditioning to only GDB. Further studies should compare IPD conditioning to other techniques that can be performed on-demand to condtition the machine, such as cleaning pulses with Ohmic heating, ion- and electron-cyclotron wall conditioning.

The persistence of IPD conditioning effects was not covered by the experiments performed in this study. Future studies should investigate the rate of fading of the IPD effect.

As for the modeling part of the research, there are many areas for improvement. One could attempt to model the entire range of μ present in the experiments. Simulations with $\mu > 15$ mg/s could not converge in adequate time due to a small time step caused by large time derivatives of fields. One way to approach this issue is to compromise on the spatial resolution of the models: the time step is also limited by the size of the mesh cells, so opting to not resolve e.g. baffle might help achieving particle balance convergence. Another way is to add B gradually in steps each time the particle balance is achieved.

Modeling of B reintroduction from PFCs into the plasma via sputtering in $\mathbb{SE}$ would require setting up a wall with mixed properties: W reflectivity but B content when it comes to sputtering. Other tools like ERO2.0 [84] or WallDYN [85] might be better equipped to deal with this problem and the integration of these tools into the developed workflow may be of interest.

Another area of improvement for modeling is to account for non-axisymmetry of the PFCs and the B source. At this moment EIRENE does not function in 3D SOLEDGE simulations, which means that the 3D computations would have to be done with fluid neutrals, unless EIRENE interface STYX gets updated. It would be interesting to analyse the kinetic neutral vs fluid neutral models differences with respect to SOLEDGE models of IPD experiments – whether or not the fluid neutrals are an adequate model to match experimental data and in which conditions this is true.

The $\mathbb{SE}$ simulations presented in our study do not include "cross-B" drifts, that is, $\vec{E} \times \vec{B}$, $\vec{B} \times \nabla B$ etc, nor does it include turbulent transport. The inclusion of each could affect the poloidal distribution of $\Gamma^i_{\parallel}$, changing the final distribution of Γ^B on PFCs. The addition of each incurs longer computational time, which could be remedied with the methods discussed above.

References

[1] J. Wesson. Tokamaks. 3rd edition, Clarendon Press-Oxford (2004)

[2] P. Stangeby. The Plasma Boundary of Magnetic Fusion Devices. Institute of Physics Publishing, Bristol and Philadelphia (2000)

[3] L. Artsimovich. Tokamak devices, part 1. Kurchatov Institute of Atomic Energy (1974)

[4] The JET team. Results of JET operation with beryllium. Journal of Nuclear Materials 176 8177 (1990) 3-13

[5] J. Roth et al. Recent analysis of key plasma wall interactions issues for ITER. Journal of Nuclear Materials 390-391 (2009) 1-9

[6] D. Campbell. Challenges in Burning Plasma Physics: the ITER Research Plan. IAEA Fusion Energy Conference, San Diego, CA (United States), 8-13 Oct 2012, 789 p.

[7] R. Pitts. Physics basis and design of the ITER plasma-facing components Journal of Nuclear Materials 415 (2011) S957-S964

[8] R. Pitts et al. Status and physics basis of the ITER divertor. Phys. Scr. (2009) 014001

[9] A. Loarte et al. Initial evaluations in support of the new ITER baseline and Research Plan. ITER technical report, ITR-24-004

[10] R. Pitts et al. Plasma-wall interaction impact of the ITER re-baseline. PSI-26 conference, May 12-17 2024

[11] J. Bucalossi et al. The WEST project: Testing ITER divertor high heat flux component technology in a steady state tokamak environment. Fusion Engineering and Design 89 (2014) 907-912

[12] C. Bourdelle. WEST Physics Basis. Nuclear Fusion (2015) 55 063017

[13] Y. Corre et al. Testing of ITER-grade plasma facing units in the WEST tokamak: Progress in understanding heat loading and damage mechanisms. Nuclear Materials and Energy 37 (2023) 101546

[14] M. Missirlian et al. Manufacturing, testing and installation of the full tungsten actively cooled ITER-like divertor in the WEST tokamak. Fusion Engineering and Design 193 (2023) 113683

[15] M. Diez et al. In situ observation of tungsten plasma-facing components after the first phase of operation of the WEST tokamak. Nuclear Fusion 61 (2021) 10

[16] P. Maget et al. Healing plasma current ramp-up by nitrogen seeding in the full tungsten environment of WEST. Plasma Physics and Controlled Fusion 64 (2022) 045016

[17] T. Pütterich et al. Determination of the tolerable impurity concentrations in a fusion reactor using a consistent set of cooling factors. Nuclear Fusion 59 (2019) 056013

[18] A. Grosjean et al. Refining light impurity content estimates at the lower divertor based on experimental data in WEST. Nuclear Materials and Energy 35 (2023) 101385

[19] P. Anderson and A. Kellman. Optimized baking of the DIII-D vessel. 18th IEEE/NPSS Symposium on Fusion Engineering. Symposium Proceedings, Albuquerque, NM, USA, 1999, pp. 535-538

[20] H. Dylla. Glow discharge techniques for conditioning highvacuum systems. Journal of Vacuum Science & Technology A 6 (1988) 1276-1287

[21] J. Winter et al. Boronization in textor. Journal of Nuclear Materials 162-164 (1989) pp. 713-723

[22] J. Phillips et al. Initial boronization of the DIII-D tokamak. 38th National symposium of the American Vacuum Society, Seattle, WA (United States), 11-15 Nov 1991

[23] V. Rohde et al. Wall conditioning in ASDEX Upgrade. Journal of Nuclear Materials 363-365 (2007) 1369-1374

[24] J. Bucalossi et al. Operating a full tungsten actively cooled tokamak: overview of WEST first phase of operation. Nuclear Fusion 62 (2022) 042007

[25] M. Dibon et al. New boronization system at ASDEX Upgrade. Fusion Engineering and Design 165 (2021) 112233

[26] A. Nagy et al. A multi-species powder dropper for magnetic fusion applications. Review of Scientific Instruments 89 (2018) 10K121

[27] F. Effenberg et al. 3D modeling of boron transport in DIII-D L-mode wall conditioning experiments. Nuclear Materials and Energy 26 (2021) 100900

[28] A. Kirschner et al. Modelling of tungsten erosion and deposition in the divertor of JET-ILW in comparison to experimental findings. Nuclear Materials and Energy 18 (2019) pp. 239-244

[29] M. Mayer et al. Erosion and deposition in the JET divertor during the second ITER-like wall campaign. Physica Scripta (2017) 014058

[30] J. Hu et al. New Steady-State Quiescent High-Confinement Plasma in an Experimental Advanced Superconducting Tokamak. Physical Review Letters, 114, 055001 (2015)

[31] J. Canik et al. Active Recycling Control Through Lithium Injection in EAST. IEEE Transactions on Plasma Science, vol. 46, no. 5, pp. 1081-1085 (2018)

[32] Z. Sun et al. Real time wall conditioning with lithium powder injection in long pulse H-mode plasmas in EAST with tungsten divertor. Nuclear Materials and Energy 19 (2019) pp. 124-130

[33] T. Osborne et al. Enhanced H-mode pedestals with lithium injection in DIII-D. Nuclear Fusion 55 (2015) 063018

[34] G. Canal et al. Study of the Impact of Pre- and Real-Time Depositions of Lithium on Plasma Performance on NSTX. IEEE Transactions on Plasma Science, vol. 47, no. 8, pp. 4225-4232 (2019)

[35] A. Bortolon et al. Observations of wall conditioning by means of boron powder injection in DIII-D H-mode plasmas. Nuclear Fusion 60 (2020) 126010

[36] F. Effenberg et al. Mitigation of plasma-wall interactions with low-Z powders in DIII-D high confinement plasmas. Nuclear Fusion 62 (2022) 106015

[37] R. Maingi et al. ELM Suppression by Boron Powder Injection and Comparison with Lithium Powder Injection on EAST. Journal of Fusion Energy 39 (2020) pp. 429-435

[38] Z. Sun et al. Enhancement of edge turbulence concomitant with ELM suppression during boron powder injection in EAST. Physics of Plasmas 28 (2021) 082512

[39] W. Xu et al. Comparison of active impurity control between lithium and boron powder real-time injection in EAST. Physica Scripta 96 (2021) 124034

[40] W. Xu et al. Active wall conditioning through boron powder injection compatible ELM control in EAST. Nuclear Materials and Energy 34 (2023) 101359

[41] K. Krieger et al. Wall conditioning effects and boron migration during boron powder injection in ASDEX Upgrade. Nuclear Materials and Energy 34 (2023) 101374

[42] A. Bortolon et al. Real-time wall conditioning by controlled injection of boron and boron nitride powder in full tungsten wall ASDEX Upgrade. Nuclear Materials and Energy 19 (2019) pp. 384-389

[43] R. Lunsford et al. Active conditioning of ASDEX Upgrade tungsten plasma-facing components and discharge enhancement through boron and boron nitride particulate injection. Nuclear Fusion 59 (2019) 126034

[44] E. Gilson et al. Wall conditioning and ELM mitigation with boron nitride powder injection in KSTAR. Nuclear Materials and Energy 28 (2021) 101043

[45] F. Nespoli et al. First impurity powder injection experiments in LHD. Nuclear Materials and Energy 25 (2020), 100842

[46] T. Kawate et al. Experimental study on boron distribution and transport at plasma-facing components during impurity powder dropping in the Large Helical Device. Nuclear Fusion 62 (2022) 126052

[47] R. Lunsford et al. Real-time wall conditioning and recycling modification utilizing boron and boron nitride powder injections into the Large Helical Device. Nuclear Fusion 62 (2022) 086021

[48] R. Lunsford et al. Characterization of injection and confinement improvement through impurity induced profile modifications on the Wendelstein 7-X stellarator. Physics of Plasmas 28 (2021) 082506

[49] G. Bodner et al. Initial results from boron powder injection experiments in WEST lower single null L-mode plasmas. Nuclear Fusion 62 (2022) 086020

[50] R. Lunsford et al. Utilization of boron particulate wall conditioning in the full tungsten environment of WEST. Nuclear Materials and Energy 40 (2024) 101726

[51] M. Shoji et al. Full-torus impurity transport simulation for optimizing plasma discharge operation using a multi-species impurity powder dropper in the large helical device. Contributions to Plasma Physics (2020) 60:e201900101

[52] Y. Feng et al. Transport in island divertors: physics, 3D modelling and comparison to first experiments on W7-AS*. Plasma Physics and Controlled Fusion 44 (2002) 611

[53] A. Pigarov et al. Simulation of convective cross-field transport, toroidal plasma flows, and dust dynamics in NSTX with UEDGE and DUSTT codes. 47th Annual Meeting of the Division of Plasma Physics October 24-28, 2005

[54] Ph. Bibet et al. New advanced launcher for lower hybrid current drive on Tore Supra. Fusion Engineering and Design 51-52 (2000) pp. 741-746

[55] W. Helou et al. Radio-frequency electrical design of the WEST long pulse and load-resilient ICRH launchers. Fusion Engineering and Design 96-97 (2015) pp. 473-476

[56] R. Sabot et al. Development of Microwave Imaging Diagnostics for WEST Tokamak. Journal of Fusion Energy 38 (2019) pp. 394-405

[57] O. Meyer et al. Visible spectroscopy diagnostics for tungsten source assessment in the WEST tokamak: First measurements. Review of Scientific Instruments 89 (2018) 10D105

[58] R. Guirlet et al. Extreme UV spectroscopy measurements and analysis for tungsten density studies in the WEST tokamak. Plasma Physics and Controlled Fusion 64 (2022) 105024

[59] P. Manas et al. Maximizing the ion temperature in an electron heated plasma: from WEST towards larger devices. Nuclear Fusion 64 (2024) 036011

[60] P. Devynck et al. Calculation of the radiated power in WEST. Journal of Physics Communications 5 (2021) 095008

[61] C. Gil et al. Renewal of the interfero-polarimeter diagnostic for WEST. Fusion Engineering and Design 140 (2019) 81-91

[62] C. Johnson et al. ColRadPy: A Python collisional radiative solver. Nuclear Materials and Energy 20 (2019) 100579

[63] K. Behringer et al. Spectroscopic determination of impurity influx from localized surfaces. Plasma Physics and Controlled Fusion 31 (1989) 2059

[64] X. Yang et al. Core tungsten transport in WEST long pulse L-mode plasmas. Nuclear Fusion 60 (2020) 086012

[65] S. Di Genova et al. Modelling of tungsten contamination and screening in WEST plasma discharges. Nuclear Fusion 61 (2021) 106019

[66] C. Martin et al. Post-mortem analysis of the deposit layers on the lower divertor after the 2023 high particle fluence campaign of WEST. Nuclear Materials and Energy 41 (2024) 101764

[67] A. Gallo et al. Wall conditions in WEST during operations with a new ITER grade, actively cooled divertor. Nuclear Materials and Energy 41 (2024) 101741

[68] E. Tsitrone et al. Overview of plasma wall interactions in the first high particle fluence campaign of WEST. PSI-26 conference, May 12-17 2024

[69] N. Rivals et al. Dissipative compact divertor in WEST: experiments and SOLEDGE modelling. PSI-26 conference, May 12-17 2024

[70] H. Bufferand et al. Three-dimensional modelling of edge multi-component plasma taking into account realistic wall geometry. Nuclear Materials and Energy 18 (2019) pp. 82-86

[71] F. Nespoli et al. Hyperdiffusion of dust particles in a turbulent tokamak plasma. Physics of Plasmas 28 (2021) 073704

[72] D. Reiter et al. The EIRENE and B2-EIRENE Codes. Fusion Science and Technology 47 (2005) 2 pp. 172-186

[73] V. Zhdanov. Transport Processes in Multicomponent Plasma. 1st Edition, CRC Press (2002)

[74] T. Xie et al. EMC3-EIRENE modelling of edge plasma and impurity emissions compared with the liquid lithium limiter experiment on EAST. Nuclear Fusion 58 (2018) 106017

[75] M. Valentinuzzi et al. Fluid description of neutral particles in divertor regimes in WEST. Contributions to Plasma Physics 58 (2018) pp. 710-717

[76] F. Nespoli et al. A reduced-turbulence regime in the Large Helical Device upon injection of low-Z materials powders. Nuclear Fusion 63 (2023) 076001

[77] B. Faugeras. An overview of the numerical methods for tokamak plasma equilibrium computation implemented in the NICE code. Fusion Engineering and Design 160 (2020) 112020

[78] S. Di Genova et al. First 3D modelling of tungsten erosion and migration in WEST discharges adopting a toroidally non-symmetric wall geometry. Nuclear Materials and Energy 34 (2023) 101340

[79] D. Reiter et al. Database for recycling and penetration of neutral helium atoms in the boundary of a fusion plasma. KFA-Jülich report, Jül-2605 Forschungszentrum Jülich, Germany (April 1992)

[80] A. Gallo et al. Interpretative transport modeling of the WEST boundary plasma: main plasma and light impurities. Nuclear Fusion 60 (2020) 126048

[81] S. Di Genova et al. Modelling of tungsten contamination and screening in WEST plasma discharges. Nuclear Fusion 61 (2021) 106019

[82] A. Gallo et al. First efforts in numerical modeling of tungsten migration in WEST with SolEdge2D-EIRENE and ERO2.0. Physica Scripta (2020) 014013

[83] S. Baschetti et al. Optimization of turbulence reduced model free parameters based on L-mode experiments and 2D transport simulations. Contributions to Plasma Physics 58 (2018) 511-517

[84] J. Romazanov et al. Beryllium global erosion and deposition at JET-ILW simulated with ERO2.0. Nuclear Materials and Energy 18 (2019) 331-338

[85] K. Schmid et al. An integrated model of impurity migration and wall composition dynamics for tokamaks. Journal of Nuclear Materials 415 (2011) S284-S288